

**Editor-in-Chief B.E.Paton**

**EDITORIAL BOARD**

Yu.S. Borisov,  
B.V. Khitrovskaya (*exec. secretary*),  
V.F. Khorunov, V.V. Knysh, I.V. Krivtsun,  
S.I. Kuchuk-Yatsenko (*vice-chief editor*),  
Yu.N. Lankin, V.N. Lipodaev (*vice-chief editor*),  
L.M. Lobanov, A.A. Mazur,  
O.K. Nazarenko, I.K. Pokhodnya,  
V.D. Poznyakov, I.A. Ryabtsev,  
K.A. Yushchenko,  
A.T. Zelnichenko (*exec. director*)  
(*Editorial Board Includes PWI Scientists*)

**INTERNATIONAL EDITORIAL  
COUNCIL**

**N.P. Alyoshin**  
N.E. Bauman MSTU, Moscow, Russia  
**V.G. Fartushny**  
Welding Society of Ukraine, Kiev, Ukraine  
**Guan Qiao**  
Beijing Aeronautical Institute, China  
**V.I. Lysak**  
Volgograd State Technical University, Russia  
**B.E. Paton**  
PWI, Kiev, Ukraine  
**Ya. Pilarczyk**  
Welding Institute, Gliwice, Poland  
**U. Reisgen**  
Welding and Joining Institute, Aachen, Germany  
**O.I. Steklov**  
Welding Society, Moscow, Russia  
**G.A. Turichin**  
St.-Petersburg State Polytechn. Univ., Russia  
**M. Zinigrad**  
College of Judea & Samaria, Ariel, Israel  
**A.S. Zubchenko**  
OKB «Gidropress», Podolsk, Russia

**Founders**

E.O. Paton Electric Welding Institute  
of the NAS of Ukraine  
International Association «Welding»

**Publisher**

International Association «Welding»

**Translators**

A.A. Fomin, O.S. Kurochko,  
I.N. Kutianova  
*Editor*  
N.A. Dmitrieva  
*Electron galley*  
D.I. Sereda, T.Yu. Snegiryova

**Address**

E.O. Paton Electric Welding Institute,  
International Association «Welding»  
11, Bozhenko Str., 03680, Kyiv, Ukraine  
Tel.: (38044) 200 60 16, 200 82 77  
Fax: (38044) 200 82 77, 200 81 45  
E-mail: journal@paton.kiev.ua  
www.patonpublishinghouse.com  
State Registration Certificate  
KV 4790 of 09.01.2001  
ISSN 0957-798X

**Subscriptions**

\$348, 12 issues per year,  
air postage and packaging included.  
Back issues available.

All rights reserved.

This publication and each of the articles contained  
herein are protected by copyright.  
Permission to reproduce material contained in this  
journal must be obtained in writing from the  
Publisher.

## CONTENTS

### SCIENTIFIC AND TECHNICAL

- Semyonov A.P.* Methods of mathematical modelling of the processes of electrode metal drop formation and transfer in consumable electrode welding (Review) ..... 2
- Moltasov A.V., Samotryasov S.M., Knysh V.V., Chvertko P.N.* and *Gushchin K.V.* Influence of non-uniformity of heating on upsetting force value and forging time in flash-butt welding of flat ring ..... 11
- Maksymova S.V., Khorunov V.F., Myasoed V.V., Voronov V.V. and Kovalchuk P.V.* Microstructure of brazed joints of nickel aluminide ..... 15
- Kuzmenko D.N., Ustinov A.I., Kosintsev S.G. and Petrushinets L.V.* Influence of heating rate on inflammation temperature of multilayer Ti/Al foil ..... 22
- Buzorina D.S., Sholokhov M.A. and Shalimov M.P.* Improvement of the procedure of mode parameter calculation for gas-shielded multipass welding ..... 26

### INDUSTRIAL

- Lobanov L.M., Makhnenko O.V., Saprykina G.Yu. and Pustovoj A.D.* Fatigue calculation for welded joints of bearing elements of freight car bogie ..... 30
- Poleshchuk M.A., Atroshenko M.G., Puzrin A.L. and Shevtsov V.L.* Estimation of possibility for producing full-strength joint of large steel parts using the method of autovacuum brazing of threaded profile ..... 35
- Pismenny A.A., Gubatyuk R.S., Prokofiev A.S., Muzhichenko A.F. and Shinkarenko A.S.* Braze-welded tubular billets for pipelines and high-pressure vessels ..... 38
- Grechanyuk N.I., Kucherenko P.P., Melnik A.G., Kovalchuk D.V. and Grechanyuk I.N.* Industrial electron beam installation L-8 for deposition of heat-protective coatings on turbine blades ..... 45
- Keitel S., Ahrens C. and Moll H.* Computer-based technologies and their influence on welding education ..... 51



# METHODS OF MATHEMATICAL MODELLING OF THE PROCESSES OF ELECTRODE METAL DROP FORMATION AND TRANSFER IN CONSUMABLE ELECTRODE WELDING (Review)

A.P. SEMYONOV

E.O. Paton Electric Welding Institute, NASU  
11 Bozhenko Str., 03680, Kiev, Ukraine. E-mail: office@paton.kiev.ua

Processes of welding wire heating and melting, electrode metal drop formation and transfer in consumable electrode welding largely determine welding efficiency and quality. In its turn, the nature of metal melting and transfer with this welding process is determined by a large number of such physical phenomena as heat and mass transfer, gas(hydro)dynamics, electromagnetic processes, running in arc plasma, on the surface and in the volume of molten electrode metal-drop. This paper gives a review of currently available methods of theoretical investigation and mathematical modelling of the above processes, allowing prediction of such characteristics of electrode metal transfer as drop volume and shape, their thermal and gas-dynamic state, detachment frequency, etc. Advantages and disadvantages of the considered models are analyzed and main directions of their further development are outlined. 37 Ref., 11 Figures.

**Keywords:** consumable electrode welding, mathematical modelling, electrode metal drop formation

Interest to the problem of metal transfer in consumable electrode welding is due to a number of causes. It is known that formation of electrode metal drop can be accompanied by its overheating, leading to considerable loss of alloying elements contained in welding wire, bulk boiling and spattering of drop metal, closing of arc gap, etc. In addition, metal transfer mode essentially influences the processes running in the weld pool that, in its turn, determines weld formation. Ensuring directed metal transfer in welding in different positions is also important. Therefore, this work sets forth the known theoretical approaches and describes the available mathematical models, allowing prediction of the main characteristics of metal transfer at different technological parameters of consumable electrode welding.

Methods of mathematical modelling of drop formation and electrode metal transfer in consumable electrode welding can be conditionally divided into two main groups (Figure 1). The first includes approaches, which enable prediction of just the individual characteristics of metal transfer process, such as drop size and detachment frequency. The main disadvantage of these models consists in that they do not allow determination of drop shape, or describing the phenomena of charge and energy transfer in molten electrode metal, which accompany the considered techno-

logical process. The first group includes such procedures as static force balance theory (SFBT) [1–3], pinch instability theory (PIT) [4–6], as well as dynamic force balance theory (DFBT) [7, 8]. The second group includes the model of drop formation in terms of hydrostatic approximation [9–11], as well as models based on equations of motion of viscous incompressible liquid. In its turn, in the subgroup of dynamic models thin jet approximation can be singled out [12–14], as well as models based on total system of Navier–Stokes equations [15–20]. Let us consider the most widely accepted of the above methods.

**SFBT.** This method is based on analysis of the magnitude of resultant of forces, applied to molten metal drop. Drop dimensions and their detachment frequency are calculated, proceeding from detachment criterion. We assume that the drop has an axisymmetric shape and its detachment occurs at the moment, when the force, directed at drop detachment, is comparable by absolute value with the restraining force magnitude. Drop formation and detachment are determined by simultaneous action of forces of surface tension, gravity, electromagnetic, as well as aerodynamic force, due to mechanical interaction of metal drop with shielding gas flow. Surface tension force is calculated, using the following formula:

$$F_s = 2\pi R_w \gamma, \quad (1)$$

where  $R_w$  is the welding electrode radius;  $\gamma$  is the coefficient of liquid metal surface tension. Note that during drop growth the axial compo-

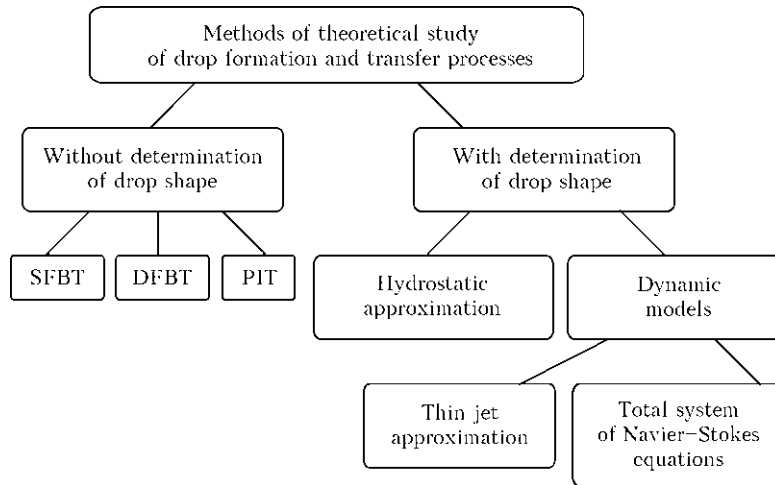


**Figure 1.** Classification of methods of theoretical study of the processes of electrode metal drop formation and transfer

ment of restraining force varies by magnitude, and formula (1) determines only its possible maximum value (upper estimate). Gravity force is calculated from the assumption that the drop has the shape of a sphere of radius  $R_d$ :

$$F_g = \frac{4}{3} \pi R_d^3 \rho g, \quad (2)$$

where  $\rho$  is the drop metal density;  $g$  is the acceleration of gravity. Integral electromagnetic force is usually determined with application of an approach proposed in [21]. Let us write down the final expression for calculation of Lorenz force, acting on the drop:

$$F_{em} = \frac{\mu_0 I^2}{4\pi} \times \left( \frac{1}{4} + \frac{1}{1 - \cos \phi} - \frac{2}{(1 - \cos \phi)^2} \ln \left( \frac{2}{1 + \cos \phi} - \ln \left( \frac{R_d \sin \phi}{R_w} \right) \right) \right), \quad (3)$$

where  $\mu_0$  is the magnetic constant, and angle  $\phi$  determines the current-conducting region on the

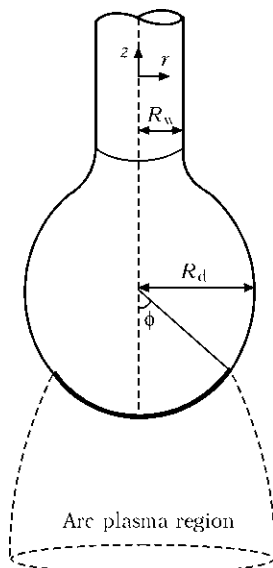


**Figure 2.** Schematic for analysis of SFBT method

drop surface (region of arc anode binding) (Figure 2).

Aerodynamic resistance is approximately calculated as a force applied to a sphere in gas flow:

$$F_a = \pi R_d^2 C_D - \frac{\rho_g v_g^2}{2}, \quad (4)$$

where  $C_D$  is the coefficient of aerodynamic resistance;  $\rho_g, v_g$  is the density and velocity of shielding gas flow, respectively. Dimensions of detached drop are found by solving non-linearity equation relative to unknown  $R_d$  value:

$$F_s = F_a(R_d) + F_{em}(R_d) + F_g(R_d). \quad (5)$$

Frequency of drop detachment is readily calculated at known values of wire feed rate and drop radius.

As can be seen, analysis of force factors influencing metal transfer characteristics is rather an estimate, as the drop surface is assumed to be spherical. Probably, this is exactly why the best agreement between experimental results and calculation data, derived by SFBT method, is observed in the case of globular metal transfer (Figure 3). More over, when deriving expression

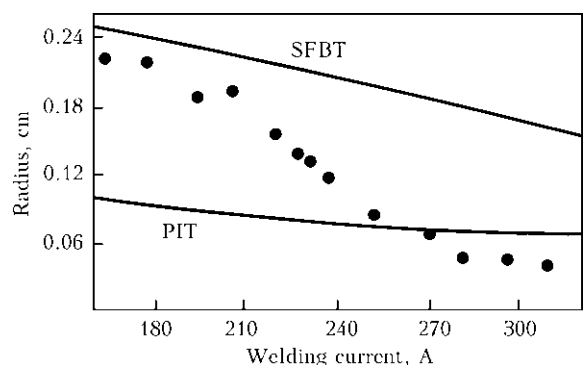


**Figure 3.** Comparison of experimental data (dots) with calculated ones (solid lines), obtained with SFBT and PIT methods [22], on dependence of dimensions of detached drops on current in welding with 1.2 mm steel wire in Ar + 2 % O<sub>2</sub> mixture

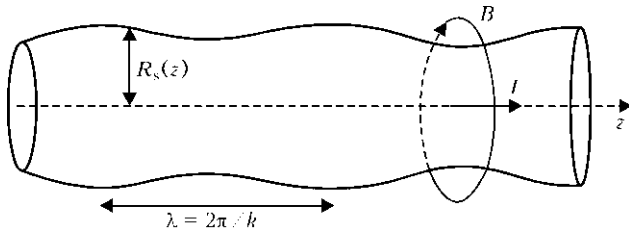


Figure 4. Instability of current-carrying liquid jet

(3), an assumption was made that current density is uniformly distributed in arc anode binding region. It should be also noted that within SFBT bounds, the influence of various kinds of shielding gas, or length of electrode extension on the process of drop formation and detachment cannot be substantiated.

**DBFT.** This model is similar to SFBT model in many respects. In this connection, this paper does not give its detailed description. Main difference of DFBT model from SFBT model consists in that it additionally allows for the forces of inertia.

**PIT.** Formation of electrode metal drops in terms of PIT model is treated as decomposition of a cylindrical liquid jet. This model is a generalization of Raleigh–Plateau theory of instability in the case of current-carrying jet. In keeping with works [4, 5] let us set forth the main postulates of this model. Let us consider an infinitely long liquid jet of radius  $R_0$ , through which electric current  $I$  is running (Figure 4).

We will assume that the liquid surface undergoes a harmonic disturbance of small amplitude  $\alpha$

$$R_s = R_0 + \alpha e^{\omega t + ikz}, \quad \alpha \ll R_0, \quad (6)$$

where  $\omega$  is the parameter characterizing the velocity of disturbance increment;  $k$  is the wave number of the considered mode. The following dispersion equation is derived by solving the linealized problem of magnetic hydrodynamics for a liquid jet:

$$\omega^2 = x(1 - x^2) \frac{I_1(x)}{I_0(x)} \theta_\gamma + \left( 1 + \frac{x}{2} \left( \frac{I_1(x)}{I_0(x)} - \frac{I_0(x)}{I_1(x)} \right) \right) \theta_J, \quad x = R_0 k, \quad (7)$$

where  $\theta_\gamma = \gamma/\rho_0^3$ ;  $\theta_J = \mu_0 I^2 / \rho \pi^2 R_0^4$ ;  $I_n(x)$ ,  $n = 0, 1$  is the modified Bessel's function. One can see from Figure 5 that the disturbances, the length of which is smaller than  $\lambda_c = x_c / 2\pi R_0$  are decaying. As  $\omega^2(x)$  dependence is nonmonotonic, there exist disturbance modes  $\lambda_m$ , to which maximum propagation rate corresponds.

Analysis of equation (7) allows determination of

$$\begin{cases} \lambda_c = \frac{2\pi R_0}{0.923 \cdot \theta^{0.274}}, \\ \lambda_m = \frac{2\pi R_0}{0.625 \cdot \theta^{0.278}}, \\ \omega_m^2 = 0.616 \cdot \theta^{0.278}, \end{cases} \quad (8)$$

where  $\theta = \mu_0 I^2 / \pi^2 \gamma R_0$ . Further construction of PIT model is based on dependences (8). Let us assume that the length of jet section, from which the drop forms later on, is equal to  $3\lambda/4$  (Figure 6). At transition from drop mode of metal transfer to spray mode, the molten electrode tip takes a tapered form (taper formation), as a result of which the drop base radius turns out to be much smaller than that of the wire. In the model, this factor is allowed for by geometrical parameter  $\delta$  determining  $R_0 = \delta R_w$  interrelation. Selection of value  $\delta$  depends on the considered transfer mode. To study formation of large drops, values  $\delta > 1$  are used, whereas for spray mode  $\delta < 1$ .

Let us write the resultant expressions, yielded by PTI model for drop volume  $V_d$  and their detachment frequency  $f_d$ :

$$V_d = \frac{\pi R_w^2}{2} \delta^2 \lambda_m, \quad (9)$$

$$f_d = \frac{2v_w}{\delta^2 \lambda_m}, \quad (10)$$

where  $v_w$  is the wire feed rate.

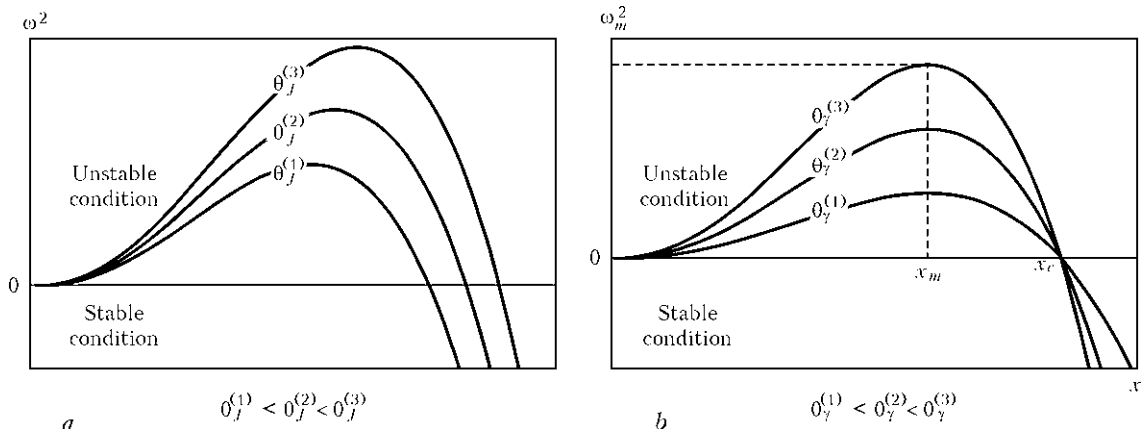


Figure 5. Influence of current (a) and surface tension (b) on velocity of instability propagation



The best agreement between experimental data and results, derived with PIT method (see Figure 3), is observed in the case of large values of welding current ( $I > 240$  A), which are characterized by spray metal transfer. PIT model does not require any significant computational expenses or specialized software to determine the main characteristics of metal transfer. Similar to the previous model, however, PIT cannot clarify the influence of the kind of shielding gas or dimensions of electrode extension on the process of metal transfer. More over, at development of PIT method in works [4, 5] an important assumption was made that the total current is concentrated in the liquid jet volume, that is obviously not in agreement with experimental observations. Interrelation of value  $\delta$  with other technological parameters of the welding process is also beyond the scope of the model. Work [6] is an attempt to correct some of the above disadvantages of the model: current flowing through the jet surface is taken into account, and jet effective radius  $R_0$  is determined depending on current value.

**Model of drop formation in terms of hydrostatic approximation.** Numerous studies are devoted to the problem of finding the equilibrium form of liquid free surface in the gravity field and analysis of its stability, and their results are described in detail in [23, 24]. Analytical methods can be applied to solve this class of problems only in rare cases. As a rule, the body of numerical methods is used for this purpose (to find a solution). Theory of capillary surfaces can be readily generalized in the case of more complex processes, where electromagnetic forces are present and sometimes have the dominant effect, as well as forces generated by pressure of vapour, which evaporates from the free surface. Mathematical model of formation of electrode metal drop, allowing for the influence of electromagnetic forces, was proposed for the first time in [10]. Let us dwell on the main postulates of this model. The essence of the problem consists in determination of the shape and volume of an ultrastable drop, hanging from the electrode tip of specified radius. We will assume that the drop shape has the property of axial symmetry and can be described in the cylindrical system of coordinates as function  $R = R(z)$ ,  $0 \leq z \leq L_d$ , where  $L_d$  is the drop height. The considered model is based on hydrostatic equations

$$\begin{cases} \frac{\partial P}{\partial r} + j_z B = 0, \\ -\frac{\partial P}{\partial r} + j_r B - \rho g = 0 \end{cases} \quad (11)$$

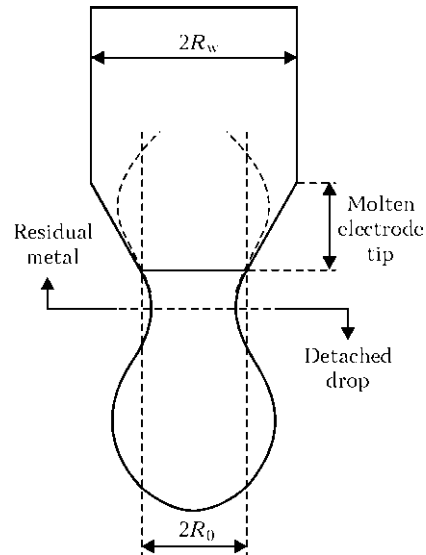


Figure 6. Schematic of drop formation in terms of PIT model [5]

and Laplace's law

$$\gamma \left( \frac{1}{R_1} + \frac{1}{R_2} \right) = P(R, z), \quad (12)$$

where  $P$  is the pressure in liquid;  $R_1, R_2$  are the main radii of surface curvature;  $j_r, j_z$  are the components of current density vector;  $B$  is the magnetic field induction. Main equations of the model have the following form:

$$\begin{cases} \frac{dP_0}{dz} = -\rho g + \frac{\mu_0 R^2}{16} \frac{d}{dz} \left( \frac{I^2}{\pi^2 R^4} \right), \\ P_0 = \frac{\mu_0 I^2}{4\pi^2 R^2} + \gamma \times \\ \times \left( -\frac{R''}{(1 + R'^2)^{3/2}} + \frac{1}{R(1 + R'^2)^{1/2}} \right), \end{cases} \quad (13)$$

$$0 \leq z \leq L_d,$$

where  $P_0(z) = P_0(0, z)$  is the pressure on drop axis;  $I = I(z)$  is the total current flowing in the drop section  $z = \text{const}$ . Equations (13) are complemented by boundary conditions.

$$R|_{z=0} = 0, \quad R|_{z=L_d} = R_w, \quad (14)$$

as well as integral condition

$$V_d = \pi \int_0^{L_d} R^2 dz. \quad (15)$$

When solving the problem, it is necessary to know how current, flowing through the drop cross-section, varies depending on height. In work [10] linear approximation  $I(z) = I_0 z / L_d$  is used for this purpose. Size of integration range  $L_d$  is an unknown and should be determined.

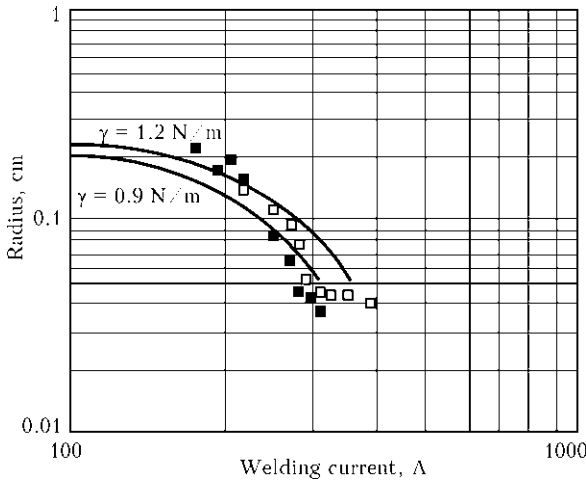


**Figure 7.** Dependence of detached drop radius on welding current: ■, □ – experimental data of [22, 25], respectively; solid curves – numerical modelling [10]

Numerical solution of problem (13)–(15) is found using Runge–Kutta method. It is also important to note that such a solution is not unique for the specified wire radius and drop volume. From the multitude of solutions, it is necessary to select only the one which meets the criterion of stability [23]. In [10] comparison of experimental data [22, 25] for the detached drop radius with calculated values of similar quantity, generated using the considered model, is also performed (Figure 7). Numerical computations were conducted for welding low-carbon steel at 1.2 mm electrode diameter. As shown by computational experiments, for fixed electrode radius there exists threshold current value  $I_{th}$ , at which problem (13)–(15) does not have a stable solution. The author believes that this current value corresponds to transition of drop mode of metal transfer into the spray mode. An approximation dependence is proposed to calculate this parameter

$$I_{th} = \sqrt{3.85 \cdot 4\pi^2 R_w \gamma / \mu_0}. \quad (16)$$

An important advantage of hydrostatic models is their relative simplicity. Performance of calculations on the base of these models does not require any significant computational resources. Such an approach, however, allows tracing drop formation just up to the stage of loss of stability. Processes of heat transfer in the metal volume also remain beyond the scope of the considered model. Thus, a more complete description of the process of drop formation at the tip of consumable electrode should be based on models describing hydrodynamic processes, proceeding in the drop.

**Thin jet approximation.** Model using total system of Navier–Stokes equations to describe hydrodynamic processes in the drop requires numerical realization of considerable computational resources that limits its application in a massive numerical experiment. Thin jet approximation [26], adapted to consumable electrode welding conditions [14], is considered as an alternative to this model. The following hypotheses were used in development of this model:

- melting front has a flat shape;
- wire feed rate corresponds to its melting rate;
- eddy motion of metal inside the drop is absent;
- arc column shape is assumed to be specified.

Model is based on the following system of equations:

$$\begin{cases} \frac{\partial V_0}{\partial t} + V \frac{\partial V_0}{\partial z} = -\frac{1}{\rho} \frac{\partial p_0}{\partial z} + \frac{3v}{h^2} \frac{\partial}{\partial z} \left( h^2 \frac{\partial V_0}{\partial z} \right) + g, \\ \frac{\partial h^2}{\partial t} + \frac{\partial (V_0 h^2)}{\partial z_\infty} = 0, \\ p_0 = 2\gamma K + \int_0^r j_z B dr, \end{cases} \quad (17)$$

where  $V_0 = V_0(z, t)$  is the axial component of velocity on drop axis;  $p_0 = p_0(z, t)$  is the pressure on drop axis;  $h = h(z, t)$  is the function describing the free surface shape;  $K$  is the mean surface curvature. Initial and boundary conditions for equations (17) have the following form:

$$h(z, 0) = h_0(z), \quad V_0(z, 0) = 0, \quad z \in (L_w, L_w + L_d^{(0)}), \quad (18)$$

$$\begin{aligned} V_0(L_w + L_d, t) &= \frac{dL_d}{dt}, \quad V_0(L_w, t) = v_w, \\ h(L_w + L_d, t) &= 0, \quad h(L_w, t) = R_w, \end{aligned} \quad (19)$$

where  $L_d^{(0)}$ ,  $h_0(z)$  is the drop length and its surface shape in the initial condition, respectively. Solution of problem (17)–(19) is in the region of  $L_w + L_d \geq z \geq L_w$  (Figure 8).

Drop length, similar to the case of hydrostatic model, is to be determined. Calculation results,

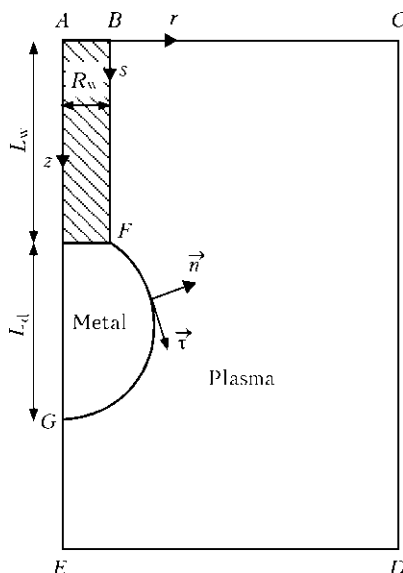


**Figure 8.** Schematic of calculation region

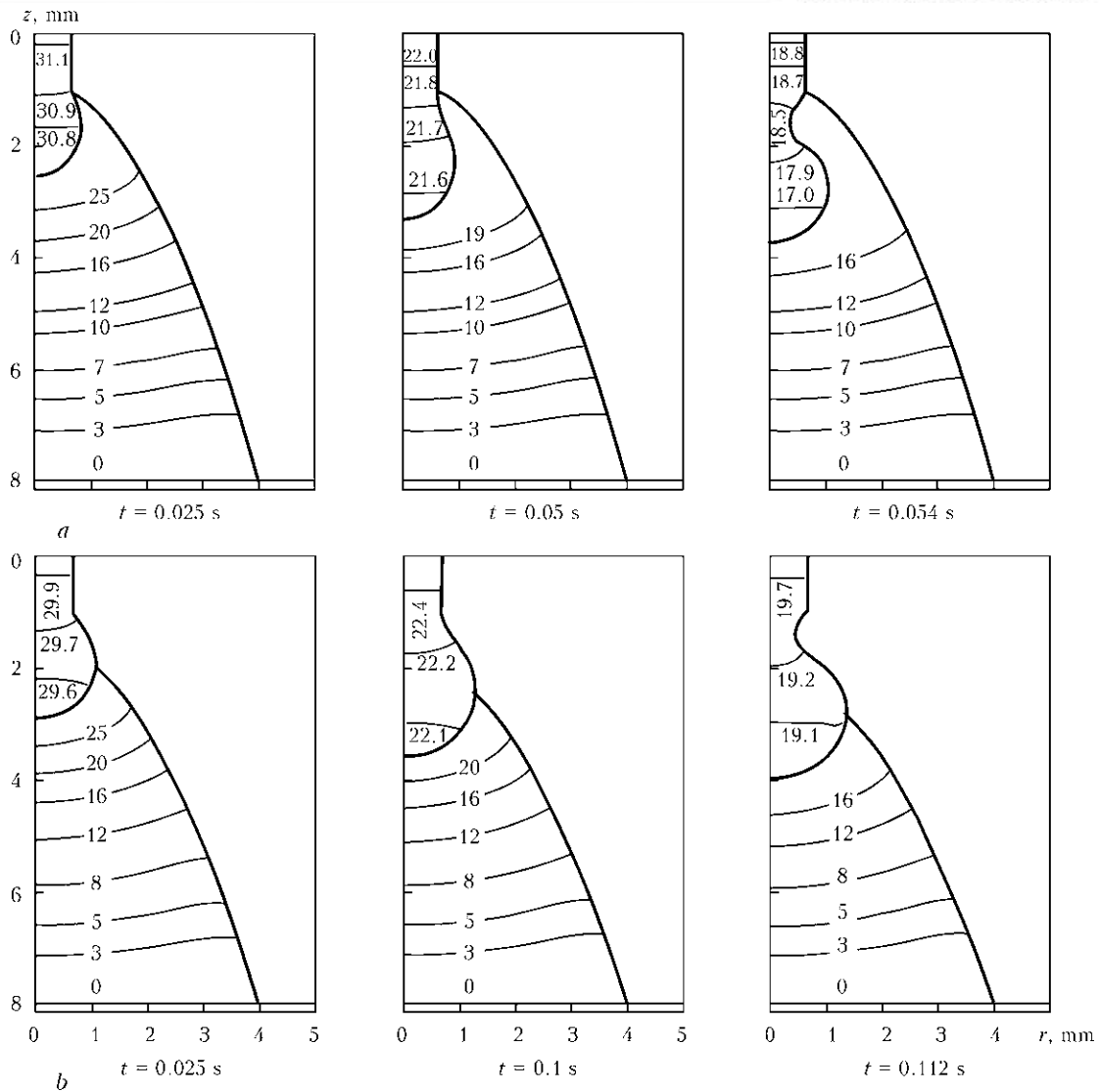


**Figure 9.** Dynamics of drop formation [14] for welding low-carbon steel in argon at  $I = 200$  A,  $R_w = 0.6$  mm and  $v_w = 4$  m/min: *a* – region of arc binding corresponding to fusion boundary; *b* – same, corresponding to maximum drop radius

obtained with the described model for two variants of arc binding to drop surface, are given in Figure 9.

Model of drop formation, based on thin jet equations, is a quite effective tool to obtain information about metal transfer characteristics. It, however, still does not allow describing a number of phenomena, having a dominant influence on heat transfer process. As shown by numerical estimates [27], metal inside the drop is involved into eddy motion, caused by Marangoni effect and influence of electromagnetic forces. Intensive stirring of drop metal is also confirmed by experimental studies [28]. As a result, convective mechanism of heat transfer in drop metal prevails over the heat conductivity process. As thin jet model does not allow description of effects associated with eddy motion of liquid metal, it does not seem possible to construct an adequate

self-consistent model of drop formation on its basis.

**Model of drop formation on the basis of total system of Navier–Stokes equations.** Among the multitude of drop formation models, this model can be rightfully called the most complex one, as it covers the main physical factors influencing the process running. Moreover, development of computational algorithm to solve the respective equations involves a lot of difficulties. Let us write the mathematical formulation of the problem in the cylindrical system of coordinates:

$$\begin{cases} \rho \left( \frac{\partial u}{\partial t} + u \frac{\partial u}{\partial r} + v \frac{\partial u}{\partial z} \right) = - \frac{\partial P}{\partial r} + \mu \left( \Delta u - \frac{u}{r^2} \right) - j_z B, \\ \rho \left( \frac{\partial v}{\partial t} + u \frac{\partial v}{\partial r} + v \frac{\partial v}{\partial z} \right) = - \frac{\partial P}{\partial z} + \mu \Delta v + g\rho + j_r B, \\ \frac{1}{r} \frac{\partial}{\partial r} (ru) + \frac{\partial v}{\partial z} = 0. \end{cases} \quad (20)$$



Here,  $u, v$  are the radial and axial components of velocity vector  $\vec{V}$ , respectively;  $\mu$  is the dynamic viscosity of drop metal. Integration domain  $ABFG$  for equations (20) covers liquid metal zone and electrode solid part (see Figure 8). Let us assume that at initial moment of time  $t = t_0$  there is no metal motion:  $\vec{V}|_{t=t_0} = 0$ . Boundary conditions for equations (20) have the following form:

$$u|_{AG} = 0, \quad v|_{AB} = v_w, \quad (21)$$

$$\left( P - 2\mu \frac{\partial V_n}{\partial n} \right) \Big|_{BFG} = 2\sigma K + P_{ev}, \quad (22)$$

$$\mu \left( \frac{\partial V_n}{\partial s} + \frac{\partial V_\tau}{\partial n} \right) \Big|_{BFG} = \frac{\partial \gamma}{\partial s}, \quad (\vec{V}|_{BFG} - \vec{V}_s, \vec{n}) = 0, \quad (23)$$

where  $\vec{V}_s$  is the surface motion velocity;  $V_n, V_\tau$  is the projection of velocity vector on the normal and tangent to the surface, respectively;  $P_{ev}$  is the reactive pressure of metal vapours at convective evaporation. Note that conditions (22) express the balance of normal and tangential stresses on metal drop free surface. Kinematic condition (23) follows directly from mass balance on the surface. At numerical solution of hydrodynamics problem, solid phase viscosity is taken to be rather large ( $10^6$  times greater than that of liquid metal). This allows suppression of metal motion in the solid phase, and also eliminates the need for adapting the finite element net to melting front shape and setting additional boundary conditions on its surface. Such an approach was proposed for the first time in [29] and is found in literature under the name of «effective viscosity method». To solve problem (20)–(23), it is important to know electromagnetic field characteristics  $j_r, j_z$ , which, in their turn, are

calculated through application of the model of electromagnetic processes:

$$(\nabla, \vec{j}) = 0, \quad (24)$$

$$\vec{j} = -\sigma \nabla \phi, \quad (25)$$

$$[\nabla, \vec{B}] = \mu_0 \vec{j}, \quad (26)$$

where  $\sigma$  is the electric conductivity of the medium;  $\phi$  is the scalar potential of electric field. Solution of electrodynamics problem (24)–(26) is in  $ACDE$  domain (see Figure 8) at superposition of the following boundary conditions:

$$j_z|_{AB} = I/\pi R_w^2, \quad j_z|_{BC} = j_r|_{CD} = 0, \quad \phi|_{ED} = 0. \quad (27)$$

Melt volume, penetration front shape and thermal condition of the liquid metal drop–wire solid section system are determined from solution of heat transfer equation

$$\begin{aligned} \frac{\partial H}{\partial t} + u \frac{\partial H}{\partial r} + v \frac{\partial H}{\partial z} = \\ = \frac{1}{r} \frac{\partial}{\partial r} \left( r \lambda \frac{\partial T}{\partial r} \right) + \frac{\partial}{\partial z} \left( \lambda \frac{\partial T}{\partial z} \right) + \frac{j^2}{\sigma}, \end{aligned} \quad (28)$$

where  $H$  is the specific enthalpy;  $\lambda$  is the coefficient of heat conductivity. Solution (28) is in  $ABFG$  domain at the following boundary and initial conditions:

$$T|_{AB} = T_0, \quad \lambda \frac{\partial T}{\partial n} \Big|_{BFG} = q_s - q_r - q_c - q_{ev}, \quad (29)$$

$$T|_{t=t_0} = T_0, \quad (30)$$

where  $T_0$  is the initial wire temperature;  $q_s$  is the specific heat flow due to thermal impact of the arc;  $q_r, q_{ev}, q_c$  are the heat losses due to radiation, metal evaporation and convective heat exchange with shielding gas, respectively.

Volume of fluid (VOF) method [30] is the most wide-spread approach to solve the problem of drop formation (20)–(23). In VOF method the free surface is «spread» in the volume of a certain layer, thickness of which corresponds to several lengths of computational net cell, whereas surface tension force is considered as the volume force acting within this layer [31]. VOF algorithm is implemented in a number of applied software packages to solve hydrodynamics problems, such as ANSYS CFX, Fluent, Open Foam, etc. In addition, access to VOF initial program code is free [32] that allows researchers adapting it to solve problems related to metal transfer in welding. There exist also a number of other methods, where the free surface is considered as a boundary separated between two media. These methods form a group, which is found in litera-

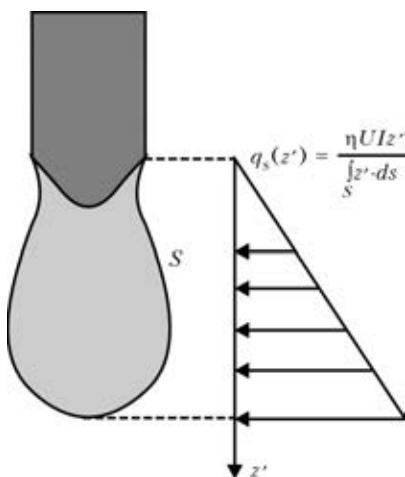


Figure 10. Heat flow distribution on the drop surface





ture under the name of front tracking methods (FTM) [33, 34]. Procedures with boundary separation allow a more detailed study of physical processes, occurring on the drop metal free surface. As an example, let us demonstrate application of FTM method to study drop formation and detachment in welding low-carbon steel in direct current mode. Physical properties of wire material and technological parameters, used in calculations, are given below.

**Physical properties of material and process parameters**

Density $\rho$ , kg·m <sup>-3</sup> .....	7200
Viscosity $\mu$ , Pa·s .....	0.006
Melting temperature $T_{\text{melt}}$ , K .....	1812
Surface tension factor $\gamma$ , N·m <sup>-1</sup> .....	1.2
Electrical conductivity $\sigma$ , cm·m <sup>-1</sup> .....	$8.54 \cdot 10^3$
Boiling temperature $T_b$ , K .....	3133
Specific heat of melting $\lambda$ , J·kg <sup>-1</sup> .....	$2.5 \cdot 10^4$
Specific heat capacity of the solid phase $c_{\text{sol}}$ , J/(kg·K) <sup>-1</sup> .....	700
Specific heat capacity of the liquid phase $c_l$ , J/(kg·K) <sup>-1</sup> .....	780
Current $I$ , A .....	350
Voltage $U$ , V .....	30.5
Wire feed rate $v_w$ , m·min <sup>-1</sup> .....	5.54
Wire diameter $d_w$ , mm .....	1.6
Thermal efficiency $\eta$ .....	0.21

During numerical experiment it is assumed that heat flow  $q_s$  is distributed by a linear law (Figure 10). Calculated form of the drop, velocity field and melting front shape are shown in Figure 11.

As was already noted, formation of electrode metal drop is determined by interaction of a number of physical phenomena running in electrode metal, including a drop on its surface, as well as in arc plasma. Mathematical modelling methods enable studying the influence of each physical factor on the processes of drop formation and detachment separately. Mathematical models, considered in this work, allow determination of the main characteristics of electrode metal transfer (drop volume, detachment frequency), describing the dynamics of drop shape variation, as well as processes of heat and mass transfer in the melt. The most adequate description of the considered processes is provided by a model based on total system of Navier–Stokes equations. As shown by computational experiments, drop shape and its dimensions are largely determined by the action of electromagnetic force, the magnitude of which, in its turn, depends on the pattern of electric current flowing in the electrode metal drop–arc column system.

In conclusion, let us show the main directions of development of models of metal transfer processes, and also note the insufficiently studied aspects of physical phenomena, accompanying the process of consumable electrode welding. Studying the dynamics of neck thinning and breaking at drop detachment, in particular formation of

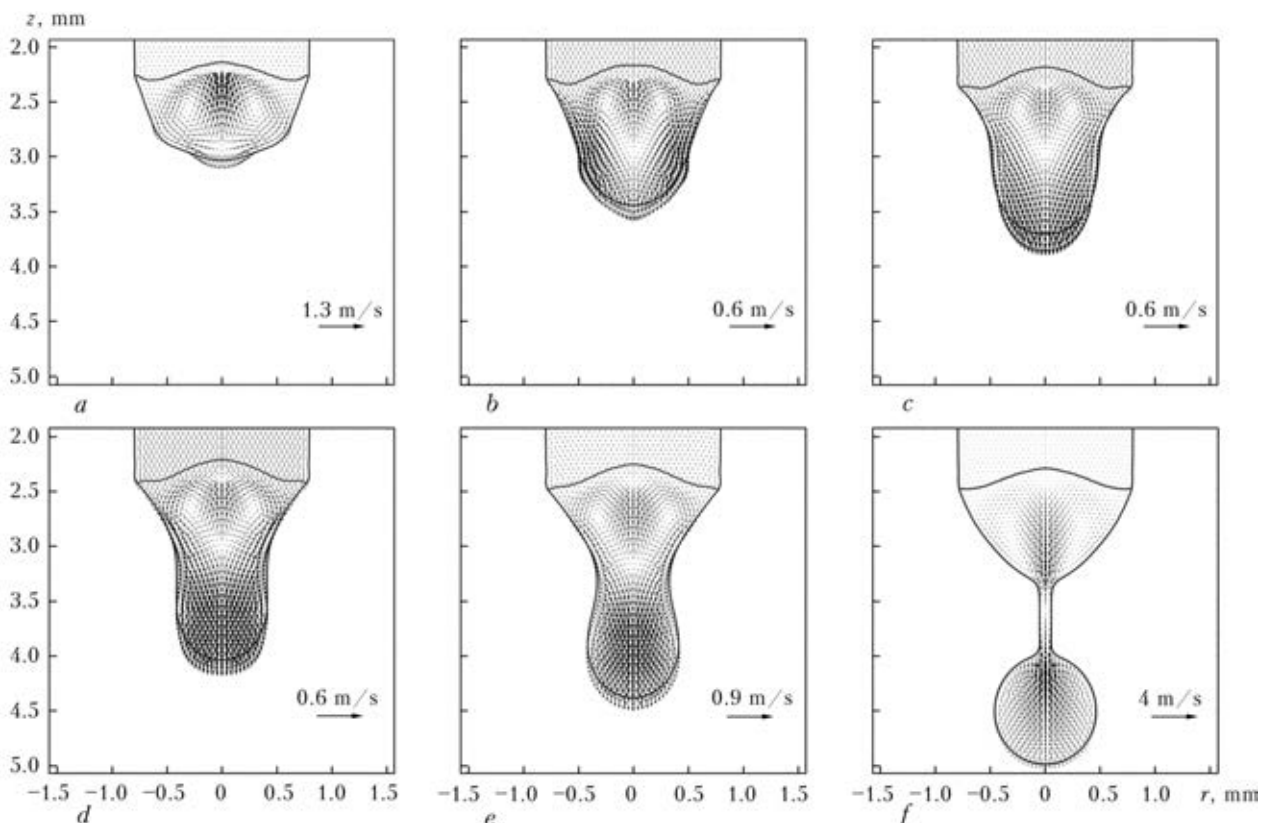


**Figure 11.** Drop shape and velocity field in the melt at different moments of time: *a* –  $t = 20.5$ ; *b* –  $21.88$ ; *c* –  $22.2$ ; *d* –  $23.1$ ; *e* –  $24$ ; *f* –  $24.93$  ms



satellite drops, is of considerable interest, as well as physical processes running in the already detached drop [35]. In addition, hydrodynamic processes in the drop metal lead to emergence of convective diffusion of alloying elements [28]. Transport of alloying elements with a low boiling temperature, from fusion boundary to drop free surface, increases their evaporation intensity. This problem is not given sufficient attention in literature. Note that metal evaporation from the drop surface can not only affect the dynamics of its free surface, but also have a significant influence on the processes running in arc plasma. As shown by experimental studies [36], this factor is the cause for formation of a local minimum of plasma temperature in the central part of arc column. The above effect is also confirmed by theoretical studies [37]. Finally, in most of the studies, devoted to modelling electrode metal drop formation in consumable electrode welding, a constant value of surface tension factor is used, whereas its value changes significantly with temperature, and also depends on chemical composition of material and shielding gas. Modern methods of investigation allow determination of the coefficient of surface tension of liquid metals in a broad temperature range. At modelling of metal transfer, it allows studying the influence of Marangoni convection on the processes of heat- and mass transfer in the drop.

1. Amson, J.C., Salter, G.R. (1962) An analysis of the gas-shielded consumable metal arc welding system. *Brit. Welding J.*, 41(4), 232–249.
2. Greene, W.J. (1960) An analysis of transfer in gas-shielded welding arcs. Pt 2. *AIEE*, 79(3), 194–203.
3. Waszink, J.H., Graat, L.H. (1983) Experimental investigation of the forces acting on a drop of weld metal. *Welding J.*, 62(4), 109–116.
4. Allum, C.J. (1985) Metal transfer in arc welding as a varicose instability. Pt 1: Varicose instabilities in a current-carrying liquid cylinder with surface charge. *J. Phys. D: Appl. Phys.*, 18(7), 1431–1446.
5. Allum, C.J. (1985) Metal transfer in arc welding as a varicose instability. Pt 2: Development of model for arc welding. *Ibid.*, 18(7), 1447–1468.
6. Park, A.Y., Kim, S.R., Hammad, M.A. (2009) Modification of pinch instability theory for analysis of spray mode in GMAW. *Ibid.*, 42(22), 225–503.
7. Choi, J.H., Lee, J., Yoo, C.D. (2001) Dynamic force balance model for metal transfer analysis in arc welding. *Ibid.*, 34(17), 2658–2664.
8. Jones, L.A., Eagar, T.W., Lang, J.H. (1998) A dynamic model of drops detaching from a gas metal arc welding electrode. *Ibid.*, 31(1), 107–123.
9. Voropaj, N.M., Kolesnichenko, A.F. (1979) Modeling of drop shape of electrode metal in gas-shielded welding. *Avtomatich. Svarka*, 9, 27–32.
10. Nemchinsky, V.A. (1994) Size and shape of the liquid droplet at the molten tip of an arc electrode. *J. Phys. D: Appl. Phys.*, 27(7), 1433–1442.
11. Semyonov, A., Demchenko, V., Krivtsov, I. et al. (2010) Modelling of process of electrode metal droplet formation. In: *Proc. of 5th Int. Conf. on Mathematical Modelling and Information Technologies in Welding and Related Processes* (25–28 May 2010, Katsiveli, Crimea, Ukraine), 183–192. Kiev: PWI.
12. Semenov, O., Demchenko, V., Krivtsov, I. et al. (2012) A dynamic model of droplet formation in GMA welding. *Modelling and Simulation in Materials Sci. and Eng.*, 20(4), 045003.
13. Krivtsov, I.V., Semenov, O.P., Demchenko, V.F. (2011) To theory of electrode metal droplet formation in GMA welding. *Dopovidi NANU*, 6, 90–96.
14. Semenov, O., Demchenko, V., Krivtsov, I. et al. (2012) Modelling of the droplet formation process in GMA welding. In: *Proc. of 10th Int. Sem. on Numerical Analysis of Weldability* (Austria, Seggau, 2012), 83–94.
15. Haidar, J., Lowke, J.J. (1996) Predictions of metal droplet formation in arc welding. *J. Phys. D: Appl. Phys.*, 29(12), 2951–2960.
16. Choi, S.K., Yoo, C.D., Kim, Y.S. (1998) Globular simulation of metal transfer in GMAW. Pt 1: Globular and spray transfer modes. *Welding J.*, 77(1), 38–44.
17. Choi, S.K., Yoo, C.D., Kim, Y.S. (1998) Dynamic simulation of metal transfer in GMAW. Pt. 2: Short-circuit transfer mode. *Ibid.*, 77(1), 45–51.
18. Fan, H.G., Kovacevic, R.A. (2004) A unified model of transport phenomena in gas metal arc welding including electrode, arc plasma and molten pool. *Ibid.*, 37, 2531–2544.
19. Wang, F., Hou, W.K., Hu, S.J. (2003) Modelling and analysis of metal transfer in gas metal arc welding. *Ibid.*, 36, 1143–1152.
20. Hu, J., Tsai, H.L. (2007) Heat and mass transfer in gas metal arc welding. Pt 1: The metal. *Int. J. Heat and Mass Transfer*, 50, 808–820.
21. Amson, J.C. (1965) Lorentz force in the molten tip of an arc electrode. *Brit. J. Appl. Phys.*, 16(8), 1169–1179.
22. Kim, Y.S., Eagar, T.W. (1993) Analysis of metal transfer in gas metal arc welding. *Welding J.*, 72, 269–278.
23. Finn, R. (1989) *Equilibrium capillary surfaces: Mathematical theory*. Moscow: Mir.
24. Hartland, S., Hartley, R.W. (1976) *Axisymmetric fluid-liquid interfaces: Tables giving the shape of sessile and pendant drops and external menisci, with examples of their use*. Amsterdam: Elsevier Sci. Publ.
25. Rhee, S., Kannatey-Asibu, E. (1992) Observation of metal transfer during gas metal arc welding. *Welding J.*, 71, 381–386.
26. Eggers, J., Dupont, T.F. (1994) Drop formation in a one-dimensional approximation of the Navier–Stokes equation. *J. Fluid Mech.*, 262, 205–221.
27. Nemchinsky, V.A. (1997) Heat transfer in a liquid droplet hanging at the tip of an electrode during arc welding. *J. Phys. D: Appl. Phys.*, 30(7), 1120–1124.
28. Wang, J.B., Nishimura, H., Katayama, S. et al. (2011) Evaporation phenomena of magnesium from droplet at welding wire tip in pulsed MIG arc welding of aluminium alloys. *Sci. and Technol. of Welding and Joining*, 16(5), 418–425.
29. Kou, S., Sun, D.K. (1985) Fluid flow and weld penetration in stationary arc welds. *Metall. Transact. A*, 16, 203–13.
30. Hirt, C.W., Nichols, B.D. (1981) Volume of fluid (VOF) method for the dynamics of free boundaries. *J. Comp. Phys.*, 39(1), 201–225.
31. Brackbill, J.U., Kothe, D.B., Zemach, C.A. (1992) A continuum method for modeling surface tension. *Ibid.*, 100(2), 335–354.
32. Nichols, B.D., Hirt, C.W., Hotchkiss, R.S. (1980) SOLA-VOF. A solution algorithm for transient fluid flow with multiple free boundaries. *NASA STI/Recon Techn. Report*, 81, 14281.
33. Wilkes, E.D., Phillips, S.D., Basaran, O.A. (1999) Computational and experimental analysis of dynamics of drop formation. *Phys. of Fluids*, 11(12), 3577–3598.
34. Degroote, J., Bruggeman, P., Vierendeels, J. (2009) A coupling algorithm for partitioned solvers applied to bubble and droplet dynamics. *Computers & Fluids*, 38(3), 613–624.
35. Nemchinsky, V.A. (2011) A droplet in the inter-electrode gap during gas metal arc welding. *J. Phys. D: Appl. Phys.*, 44, 445203.
36. Kozakov, R., Gott, G., Schopp, H. et al. (2013) Spatial structure of the arc in a pulsed GMAW process. *Ibid.*, 46, 224001.
37. Schnick, M., Hertel, M., Fuessel, U. et al. (2013) Energy balance in MIG arcs. *Ibid.*, 46, 224002.

Received 04.06.2014



# INFLUENCE OF NON-UNIFORMITY OF HEATING ON UPSETTING FORCE VALUE AND FORGING TIME IN FLASH-BUTT WELDING OF FLAT RING

A.V. MOLTASOV, S.M. SAMOTRYASOV, V.V. KNYSH, **P.N. CHVERTKO** and K.V. GUSHCHIN  
E.O. Paton Electric Welding Institute, NASU  
11 Bozhenko Str., 03680, Kiev, Ukraine. E-mail: office@paton.kiev.ua

One of the reasons of occurrence of stresses and displacements in the rings, manufactured by flash-butt welding (FBW), is the non-uniform temperature field, which is formed as a result of electric current shunting. In the frames of the present work the temperatures in different characteristic spots at the final stage of fulfillment of FBW of steel ring in machine K724 were measured. Measurements showed that at the investigated stage of welding process the temperatures of controlled spots are little changed with time, i.e. quasi-stationary heat flow takes place. Function of temperatures was preset in the form of Fourier series around the circumferential coordinate, moreover as a result of symmetry the odd members of this series were not taken into account. It appeared sufficient to be restricted by four first terms of the series. Change of temperatures in radial direction, determined from the conditions of stationarity of heat flow, showed that the action of temperature field in the ring hinders approaching of edges being welded. It results in the fact that a part of upsetting force is consumed for overcoming the elasticity forces caused by non-uniformity of heating. For the steel 20 ring considered the upsetting force, required for formation of joint, increased by 16.5 %. Besides, the presence of temperature stresses increases the force striving to rupture a butt after welding, thus leading to the necessity to prolong the butt forging time by 4 s. 7 Ref., 4 Figures.

**Keywords:** *flash-butt welding, flat rings, temperature field, stationary heat flow, temperature stresses, upsetting force, forging time*

One of the most efficient methods of joining the elements of structures of ring shape is flash butt welding (FBW). Machines for FBW [1] provide different value of upsetting force for welding of products. During development of technological modes of welding it is necessary to determine the value of edge approaching force to provide the sufficient upsetting force and overcome the ring resistance to deformation. Besides, it was shown in [2] that for conditions of welding of rings with a significant elasticity it is necessary to take into account the possibility of rupture of welded joint due to elasticity of the ring itself, if upsetting pressure is too quickly decreased after current switching off.

Earlier, it was considered during determination of forging time of welded joint [2] that the value of force, striving to rupture the welded joint, depends only on the forces of elasticity of ring shunting part, tending to impart the ring shape, which it possessed in cold state before joining of edges being welded. However, here the stresses and displacements, predetermined by non-uniformity of temperature field, which arises during performing of welding process as a result of shunting of electric current, were not consid-

ered. Temperatures of this field reach their maximum value at the final stage of welding process and then during cooling they begin to decrease slowly. Therefore, the given work is devoted to investigation of influence of temperature field, which is realized in welded ring at the FBW final stage, on the value of upsetting force and force, striving to rupture the joint.

The experimental measurements (Figure 1) showed that in the process of heating and cooling of FB-welded ring, the temperature field arises, which is the function of both radial  $r$  as well as circumferential  $\theta$  coordinate.

The non-uniformity of distribution of temperature in the circumferential direction in FBW of rings is also visually observed (Figure 2). It is clearly seen that the area of ring being welded, mostly far from clamping devices of welding machine, has a brighter glowing than the areas of shunting part, close to them. This is explained by the fact that clamping devices provide a high heat removal.

The change in temperatures in the controlled spots at the final welding stage is negligible (Figure 1, *b*) therefore, without introducing a great error, it can be considered that the temperature does not depend on time, i.e. the quasi-stationary heat flow is realized [3].

Let us represent the temperature in the form of the Fourier series:

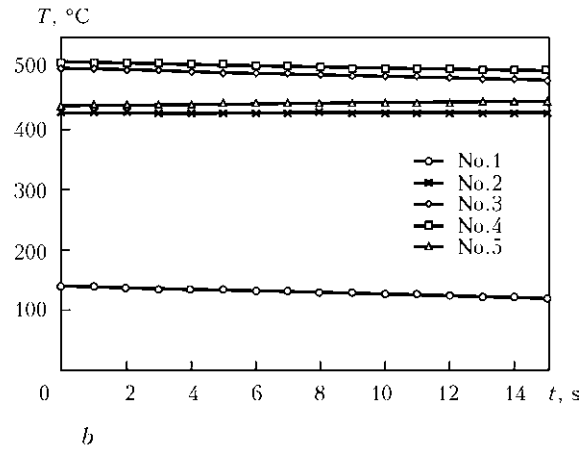
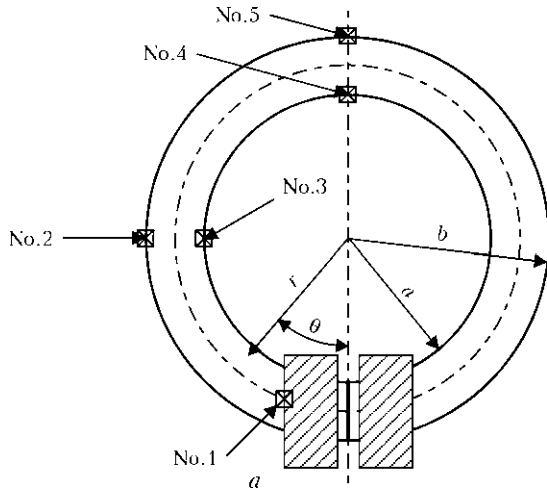


**Figure 1.** Diagram of location of spots of temperature control at the final stage of welding the ring (a), and dependence of temperatures of controlled spots on time (b)

$$T(r, \theta) = A_0(r) + \sum_1^n A_n(r) \cos n\theta, \quad (1)$$

terms, proportional to  $\sin \theta$ , are omitted, because the temperature in our case is distributed symmetrically relative to the butt.

To describe the real distribution of temperatures, let us be restricted by the four first terms, included into series (1), which will take the form

$$T(r, \theta) = A_0(r) + A_1(r) \cos \theta + A_2(r) \cos 2\theta + A_3(r) \cos 3\theta. \quad (2)$$

This series corresponds to the experimentally set values in the control spots (see Figure 1) if it meets two systems of equations at  $r = a$  and  $r = b$ :

$$\begin{cases} A_0(a) + A_1(a) + A_2(a) + A_3(a) = T_1, \\ A_0(a) - A_2(a) = T_3, \\ A_0(a) - A_1(a) + A_2(a) - A_3(a) = T_4; \end{cases} \quad (3)$$

$$\begin{cases} A_0(b) + A_1(b) + A_2(b) + A_3(b) = T_1, \\ A_0(b) - A_2(b) = T_2, \\ A_0(b) - A_1(b) + A_2(b) - A_3(b) = T_5, \end{cases}$$

where  $T_1-T_5$  are the experimental values of temperatures in the spots Nos 1-5, respectively (see Figure 1).



**Figure 2.** FBW of steel ring with  $a = 135$  mm and  $b = 190$  mm in machine K724

Solution of systems (3) has the following form:

$$A_0(a) = \frac{T_1 + T_4}{4} + \frac{T_3}{2},$$

$$A_1(a) + A_3(a) = \frac{T_1 - T_4}{2},$$

$$A_2(a) = \frac{T_1 + T_4}{4} - \frac{T_3}{2}, \quad A_0(b) = \frac{T_1 + T_5}{4} + \frac{T_2}{2}, \quad (4)$$

$$A_1(b) + A_3(b) = \frac{T_1 - T_5}{2}, \quad A_2(b) = \frac{T_1 + T_5}{4} - \frac{T_2}{2}.$$

It is not difficult to notice that a number of equations in systems (3) is not sufficient to determine the values of all the variables. Therefore, one of variables  $A_1$  or  $A_3$  is free. These variables should be selected so that to provide a monotonous growth of temperature in the interval of  $\theta$  varying from 0 to  $\pi$  and monotonous decrease in the interval of  $\theta$  varying from  $\pi$  to  $2\pi$ .

Substituting the experimental values of temperatures  $T_1 = 130$ ,  $T_2 = 430$ ,  $T_3 = 480$ ,  $T_4 = 510$  and  $T_5 = 450$  °C to system (3) and selecting the variable  $A_3$  by corresponding way, we shall obtain the following dependencies describing the changes of temperature in the circumferential direction at external and inner contour:

$$T(a, \theta) = 400 - 171 \cos \theta - 80 \cos 2\theta - 19 \cos 3\theta,$$

$$T(b, \theta) = 360 - 143 \cos \theta - 70 \cos 2\theta - 17 \cos 3\theta,$$

which are schematically presented in Figure 3.

The change of temperature in the radial direction was determined from the conditions of stationarity of the heat flow [4]

$$\nabla_1^2 T(r, \theta) = \frac{\partial^2 T}{\partial r^2} + \frac{1}{r} \frac{\partial T}{\partial r} + \frac{1}{r^2} \frac{\partial^2 T}{\partial \theta^2} = 0. \quad (5)$$

Condition (5) can be fulfilled providing that each of the items on the right side (2) meets the following condition:

$$\nabla_1^2 [A_0(r)] = 0; \quad \nabla_1^2 [A_1(r) \cos \theta] = 0; \quad (6)$$

$$\nabla_1^2 [A_2(r) \cos 2\theta] = 0; \quad \nabla_1^2 [A_3(r) \cos 3\theta] = 0.$$

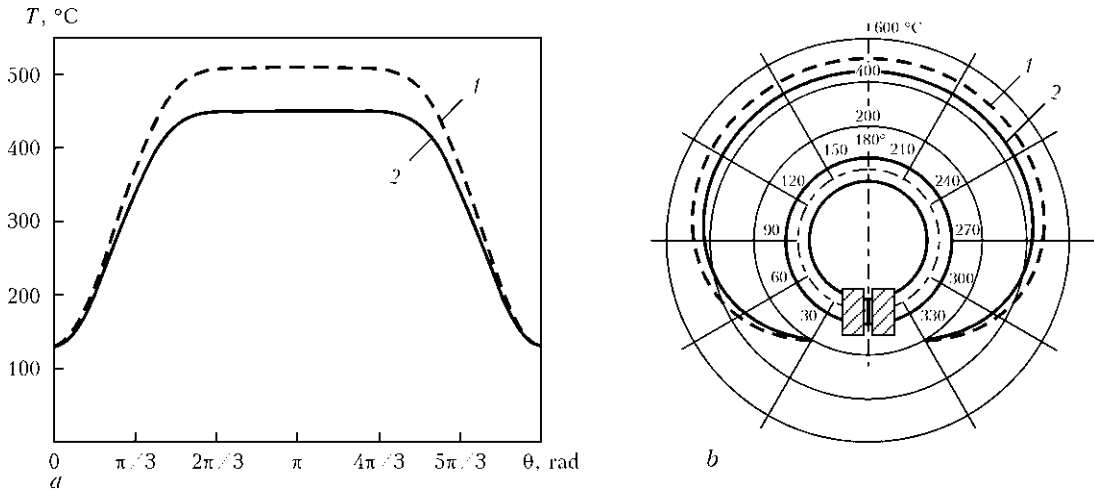


**Figure 3.** Diagrams of dependence of temperature on circumferential coordinate at  $r = a$  (1) and  $r = b$  (2) in Cartesian (a) and polar (b) coordinates

Let us represent the solution of equations (6) as follows:

$$\begin{aligned}
 A_0(r) &= K_0 + H_0 \ln r, & A_1(r) &= K_1 r + \frac{H_1}{r}, \\
 A_2(r) &= K_2 r^2 + \frac{H_2}{r^2}, & A_3(r) &= K_3 r^3 + \frac{H_3}{r^3},
 \end{aligned}
 \tag{7}$$

where  $K_i, H_i$  are the constants of integration determined from the conditions  $A_0(r) = A_0(a), A_1(r) = A_1(a), A_2(r) = A_2(a), A_3(r) = A_3(a)$  at  $r = a$  and  $A_0(r) = A_0(b), A_1(r) = A_1(b), A_2(r) = A_2(b), A_3(r) = A_3(b)$  at  $r = b$ :

$$\begin{aligned}
 K_0 &= \frac{A_0(a) \ln b - A_0(b) \ln a}{\ln b - \ln a}; \\
 K_1 &= \frac{1}{b^2 - a^2} (bA_1(b) - aA_1(a)); \\
 K_2 &= \frac{1}{b^4 - a^4} (b^2A_2(b) - a^2A_2(a)); \\
 K_3 &= \frac{1}{b^6 - a^6} (b^3A_3(b) - a^3A_3(a)); \\
 H_0 &= \frac{A_0(b) - A_0(a)}{\ln b - \ln a}; \\
 H_1 &= \frac{ab}{b^2 - a^2} (bA_1(a) - aA_1(b)); \\
 H_2 &= \frac{a^2b^2}{b^4 - a^4} (b^2A_2(a) - a^2A_2(b)); \\
 H_3 &= \frac{a^3b^3}{b^6 - a^6} (b^3A_3(a) - a^3A_3(b)).
 \end{aligned}
 \tag{8}$$

Therefore, function describing the change of temperatures in the ring,  $T(r, \theta)$ , was determined. For experimental data corresponding to the change of temperature in the circumferential direction (see Figure 3), the diagrams of variation of temperatures in the radial direction for different  $\theta$  values were plotted (Figure 4).

Determination of temperature stresses acting in the flat ring at the FBW final stage is reduced to the solution of two-dimensional problem of

thermoelasticity with stationary heat flow. To solve this problem the similarity between quasi-static problem of thermoelasticity and problem of isothermal theory of elasticity with corresponding volumetric and surface forces, considered in [5], was used.

As it was proved in [6] that the terms of series (1) at  $n > 1$  have no influence on stressed state, the components of stresses have the following form:

$$\begin{aligned}
 \sigma_r &= B_0 \frac{1}{r^2} + 2C_0 + D_0(1 + 2 \ln r) + \\
 &\quad + \left( 2B_1 r - \frac{2C_1}{r^3} + \frac{D_1}{r} \right) \cos \theta, \\
 \sigma_\theta &= -B_0 \frac{1}{r^2} + 2C_0 + D_0(3 + 2 \ln r) + \\
 &\quad + \left( 6B_1 r + \frac{2C_1}{r^3} + \frac{D_1}{r} \right) \cos \theta, \\
 \tau_{r\theta} &= \left( 2B_1 r - \frac{2C_1}{r^3} + \frac{D_1}{r} \right) \sin \theta,
 \end{aligned}
 \tag{9}$$

where  $B_0, C_0, D_0$  and  $B_1, C_1, D_1$  are the constants of integration.

In our case

$$\begin{aligned}
 B_0 &= -\frac{\alpha E H_0}{2(b^2 - a^2)} a^2 b^2 \ln \frac{b}{a}, & B_1 &= \frac{\alpha E H_1}{4(a^2 + b^2)}, \\
 C_0 &= \frac{\alpha E H_0}{4} \frac{b^2 \ln b - a^2 \ln a}{b^2 - a^2} + \frac{\alpha E H_0}{8}, \\
 C_1 &= -\frac{\alpha E H_1}{4(b^2 + a^2)} a^2 b^2, & D_0 &= -\frac{\alpha E H_0}{4} & D_1 &= -\frac{\alpha E H_1}{2},
 \end{aligned}$$

where  $\alpha$  is the coefficient of linear expansion,  $1/^\circ\text{C}$ .

It was established in [7] that upsetting force and force, striving to rupture the joint after welding, is related to the value of gap  $\delta_y$ , which represents the sum of primary gap between the edges being welded and shortenings of each of the ends

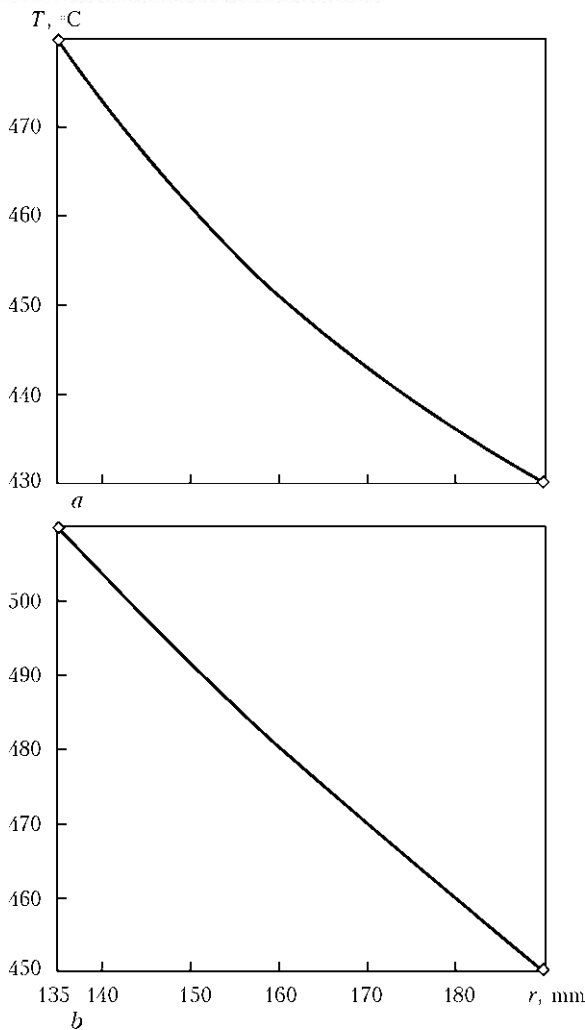


**Figure 4.** Dependence of temperature on radial coordinate for  $\theta = \pi/2$  (a) and  $\theta = \pi$  (b)

as a result of flashing and upsetting. However, as the ring is heated, it is necessary to add also displacements of edges being welded, caused by non-uniformity of heating, to the gap values.

As is shown in [6], presence of stresses (9) in the solid ring is equivalent to displacement of edges of ring with gap in the circumferential direction:

$$\delta_t = -2\pi\alpha \left( H_0 \frac{a+b}{2} + H_1 \right). \quad (10)$$

Moreover, if  $\delta_t$  is positive then the gap is increased, and if it is negative then the gap is decreased.

If to calculate the values  $H_0$  and  $H_1$ , which correspond to experimental data according to (8), then  $\delta_t$  is positive, i.e. the gap is increased. This result corresponds to data of investigations carried out in work [6] where it was proved that if in the pipe with cut the temperature of inner surface is higher than that of external one, then distance between the banks of cut is increased.

Upsetting force was calculated according to formulae from [7], and forging time was calculated from data of work [2] with account for displacements of edges being welded, caused by non-uniformity of heating, and also without its account.

For investigated steel ring (steel 20,  $\alpha = 1.5 \cdot 10^{-5} \text{ 1/}^\circ\text{C}$ ,  $E = 2 \cdot 10^5 \text{ MPa}$ ) the displacement, caused by non-uniformity of heating, amounted to 3.57 mm, that resulted in increase both of necessary upsetting force by 16.5 % and time of forging by 4 s.

### Conclusions

1. It is shown that the Fourier series can be efficiently used to describe the plane temperature fields. In particular, for temperature field, which is realized during cooling of the FB-welded ring, the sufficiently precise description of this field is provided when restricting by four first terms of this series.

2. Analytical dependence was established describing the temperature field in flat ring, which is realized at the final FBW stage. For the steel ring with inner radius  $a = 135 \text{ mm}$  and external radius  $b = 190 \text{ mm}$  the diagrams of distribution of temperatures in radial and circumferential directions were plotted.

3. It was grounded and proved by calculations that a part of upsetting force, necessary for formation of joint, is consumed to provide overcoming of elasticity forces caused by non-uniform heating. Therefore, elasticity forces for the case considered, caused by non-uniform heating, result in necessity of increase in upsetting force by 16.5 %. Presence of temperature stresses during cooling of ring results also in negligible increase in the force acting in welded joint, due to which forging time is needed to be prolonged by 4 s.

1. Kuchuk-Yatsenko, S.I., Chvertko, P.N., Semyonov, L.A. et al. (2013) Flash butt welding of products of high-strength alloys based on aluminium. *The Paton Welding J.*, **7**, 2–6.
2. Kochergin, K.A. (1952) *Selection of technology of resistance welding*. Leningrad: Sudpromgiz.
3. Carslow, Ch.S., Eger, D. (1964) *Heat conductivity of solids*. Moscow: Nauka.
4. Boley, B., Weiner, J. (1964) *Theory of thermal stresses*. Ed. by E.I. Grigolyuk. Moscow: Mir.
5. Timoshenko, S.P. (1937) *Theory of elasticity*. Leningrad; Moscow: ONTI.
6. Timoshenko, S.P., Goodier, J.N. (1975) *Theory of elasticity*. Moscow: Mir.
7. Chvertko, P.N., Moltasov, A.V., Samotryasov, S.M. (2014) Calculation of upsetting force in flash butt welding of closed-shape products. *The Paton Welding J.*, **1**, 46–50.

Received 24.03.2014



# MICROSTRUCTURE OF BRAZED JOINTS OF NICKEL ALUMINIDE

S.V. MAKSYMOVA, V.F. KHORUNOV, V.V. MYASOED, V.V. VORONOV and P.V. KOVALCHUK

E.O. Paton Electric Welding Institute, NASU

11 Bozhenko Str., 03680, Kiev, Ukraine. E-mail: office@paton.kiev.ua

Intermetallic alloys on the base of Ni<sub>3</sub>Al and NiAl phases belong to the new class of challenging casting structural materials. Application of Ni<sub>3</sub>Al-based materials allows increasing the service life of parts by 3–4 times, working temperatures of turbine inlet gas by 50–100 °C, reducing the mass of turbines and, as a consequence, increasing their specific thrust and efficiency. The wide application of alloys on Ni<sub>3</sub>Al base in industry requires the development of technological processes of producing permanent joints, including method of brazing, as the alloys, containing a high percent of  $\gamma'$ -phase, are referred to the class of hard-to-weld ones due to possible crack formation. At present, the nickel brazing filler alloys (BFA), containing silicon and boron as depressants, are used for brazing high-temperature high-alloy nickel alloys, thus leading to formation of brittle phases (silicides, borides) in joints, having a negative influence on fatigue life. Their elimination is connected with long-time conditions of heat treatment or almost impossible. The present work shows the possibility of application of eutectic BFA on nickel base, not containing boron and silicon. The results of metallographic examinations and X-ray spectral microanalysis of brazed joints of intermetallic alloys on the base of  $\gamma'$ -phase (Ni<sub>3</sub>Al) are given. Shown are the morphological peculiarities of structure formation of brazed joints, produced by high-temperature vacuum brazing and BFA on base of Ni–Cr–Zr and Ni–Co–Cr–W–Mo–Al–Nb–B systems. 7 Ref., 3 Tables, 15 Figures.

**Keywords:** *intermetallic alloys, nickel aluminides, vacuum brazing, brazing filler alloy, brazed seam, spreading tests, microstructure, X-ray spectral microanalysis*

Intermetallic alloys on the base of Ni<sub>3</sub>Al and NiAl phases belong to the new class of challenging casting structural materials, containing a large amount of  $\gamma'$ -phase and being a real alternative to metallic materials of the high-temperature application. Intermetallics Ni<sub>3</sub>Al and NiAl are characterized by an ordered crystalline lattice, that provides them a complex of high physical-mechanical properties, such as increased stability at temperatures up to 1200–1300 °C, decreased density (7.3 and 5.9 g/cm<sup>3</sup>, respectively), high modulus of elasticity and resistance to oxidation. This opens up the wide prospects of their application under high-temperature conditions, allows decreasing the mass of designed structures and increasing their coefficient of efficiency [1–5]. To widen the application of alloys on Ni<sub>3</sub>Al base in industry, it is necessary to develop technological processes of producing permanent joints including brazing, as the alloys with high content of  $\gamma'$ -phase (92–95 %) are referred to the hard-to-weld class due to a risk of crack initiation.

At present, for brazing the high-temperature high-alloy nickel alloys the brazing filler alloys (BFA) (Ni–Cr–Si–B, Ni–Cr–Co–B, Ni–W–Co–B, Ni–Cr–Al–B, Ni–Cr–Al–Si–B and Ni–Si–B)

are used, in which silicon and boron play the role of depressants. They lead to formation of brittle phases in joints (silicides and borides), the elimination of which is connected with long-term process of heat treatment or almost not possible in practice. The presence of borides in brazed joints is not desirable due to their negative effect on fatigue life. Examples of application of BFA of Ni–Cr–Fe–Si–B (MBF20) and Ni–Co–Ti–Zr systems are given in works [6, 7].

In the given work the microstructural features of joints of intermetallic alloys on  $\gamma'$ -phase base (Ni<sub>3</sub>Al), made by high-temperature vacuum brazing using an industrial BFA VPr27 (Ni–Co–Cr–W–Mo–Al–Nb–B) and experimental BFA of Ni–Cr–Zr system are considered.

To perform the experiments, intermetallic nickel alloys of two compositions (wt. %: Ni–14Al and Ni–14Al–5Mo–4Co–2.5W), as well as Ni–Cr–Zr BFA were melted. Melting was performed by electric arc method with argon blowing on cold substrate with a five-fold turning over and remelting. The produced ingots had a drop-like shape (Figure 1, *a*). Method of induction remelting was also used with ingot formation in sectional cooled mould (Figure 1, *b*). In some cases the metal melt was drawing into 4 mm diameter quartz tube using vacuum. The produced rods of 10–15 mm length and 4 mm diameter were expended into washers of 1.2 mm height and

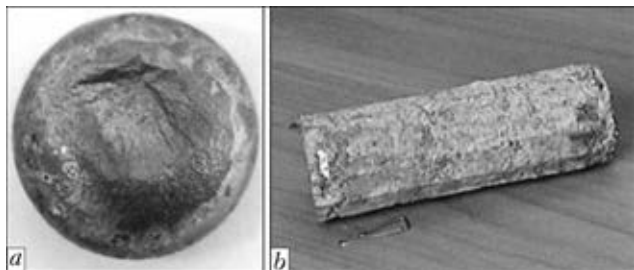


**Figure 1.** Appearance of experimental ingots melted by using arc (a) and induction (b) heating

cleaned by abrasive paper. Such plates were used for experiments on BFA spreading of and optimizing the technological process brazing.

The specimens were assembled by using resistance welding machine, then they were brazed in vacuum  $1.33 \cdot 10^{-4}$  Pa by use of radiation heating. Heating temperature was controlled by two thermocouples: main one located in furnace, and auxiliary one located next to specimens (Figure 2).

To determine the contact angle of wetting the experiments were carried out on BFA spreading according to non-standard procedure: BFA preforms in cast form were placed in the middle of melted intermetallic alloys, fixed by resistance welding and loaded into furnace. For statistics, three specimens with each BFA were loaded for one charge, they were mounted on ceramic substrate in furnace together with thermocouple and heated. The brazed joints were examined using optic (Neophot-32) and scanning electron (Tescan MIRA 3 LMU) microscopy, X-ray spectral microanalyses were carried out in energy-dispersed spectrometer Oxford Instruments X-MAX 80 with program package INCA.

The results of experiments showed that at  $T_b = 1200$  °C,  $\tau = 5$  min the Ni-Cr-Zr BFA has a good spreading over Ni-Al substrate, spread drop solidification occurs with the formation of clean surface (Figure 3, a). The given BFA is referred to eutectic alloy, characterized by a narrow interval of solidification ( $T_S = 1175$  °C,  $T_L = 1200$  °C), that has a positive influence on its spreading ability. Industrial BFA VPr27 ( $T_S =$



**Figure 2.** Appearance of specimens prepared for brazing

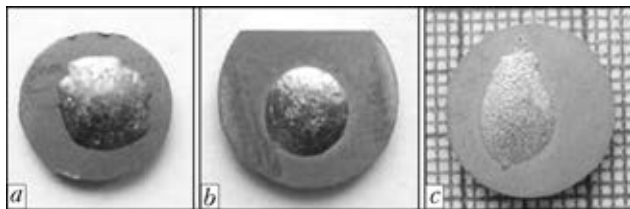


**Figure 3.** Spreading at  $T_b = 1200$  °C of experimental Ni-Cr-Zr BFA over Ni-Al ( $\tau = 5$  min) (a) and Ni-Al-Mo-Co-W ( $\tau = 15$  min) (b) substrate and industrial BFA VPr27 over Ni-Al-Mo-Co-W substrate ( $\tau = 15$  min) (c)

$= 1030$  °C,  $T_L = 1080$  °C) also provided a good wetting of surface of Ni-Al-Mo-Co-W intermetallic alloy (Figure 3, c).

To determine the contact angle of wetting, which is one of main factors in study of BFA spreading, the specimens after BFA melting were cut normal to the base material plane (plate), microsections were manufactured, contact angle, formed by surface of BFA drop and base metal, was measured, and then the metallographic examinations and X-ray spectral microanalysis were made. The obtained results showed that in use of industrial BFA VPr27 the contact angle is 12° (Figure 4, a), while in applying of experimental Ni-Cr-Zr BFA it is decreased to 6° (Figure 4, b), that confirms its better spreading ability.

The X-ray spectral microanalysis revealed the erosion of base metal and zonal liquation at the interface between BFA VPr27 and intermetallic alloy with formation of two zones, different in chemical composition (Figure 5, Table 1). The enrichment of BFA metal, adjacent to base metal,

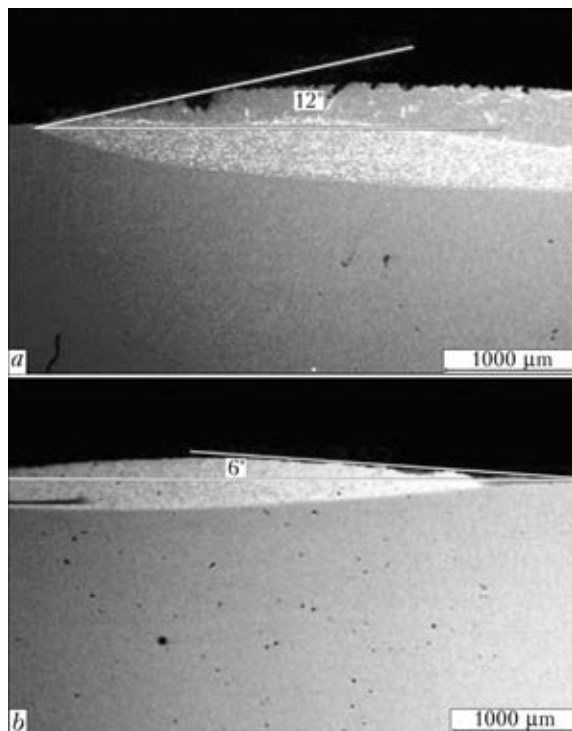


**Figure 4.** Microstructure of molten VPr27 (a) and Ni-Cr-Zr (b) BFA on intermetallic substrate



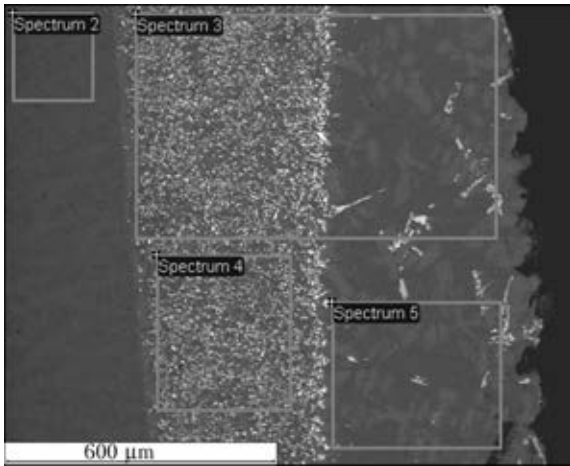


**Figure 5.** Microstructure and zonal liquation in examining regions in spreading of BFA VPr27 over Ni–Al–Co–W substrate

with tungsten (up to 14.19 %) and molybdenum (4.59 %) was also found. Diffusion of aluminium from base metal into molten BFA was observed, resulting in its concentration amounted to 3.97 %, in the zone, adjacent to base metal, and in the upper BFA (external) zone it increased up to 5.16 %. Concentration of the rest elements was differed negligibly (see Table 1).

To reduce the erosion of base metal, brazing of as-cast nickel aluminides by powdered BFA VPr27 was performed at the lower temperature (1170 °C) during 3 min. The brazed joints of Ni–Al binary alloy were formed with full fillets, in which the liquation processes were observed (Figure 6). Structure of fillet regions is greatly differed from the structure of brazed seams both by the morphological constitution and also by chemical composition. On the background of matrix of solid solution on nickel base the complex intermetallic phases are distinguished, enriched with tungsten (up to 56), molybdenum (up to 9), cobalt (up to 5) and nickel (up to 15 wt.%), which are solidified mainly in the zone adjacent to base metal. Moreover, the single inclusions of Cr–30Ni–8W–4Mo–5Co (wt.%) are observed.

The brazed seams are also characterized by chemical inhomogeneity. The regions are observed, in which phase Cr–14Ni–19W–8Mo–6Co–0.7Nb (wt.%) is formed in the seam centre.

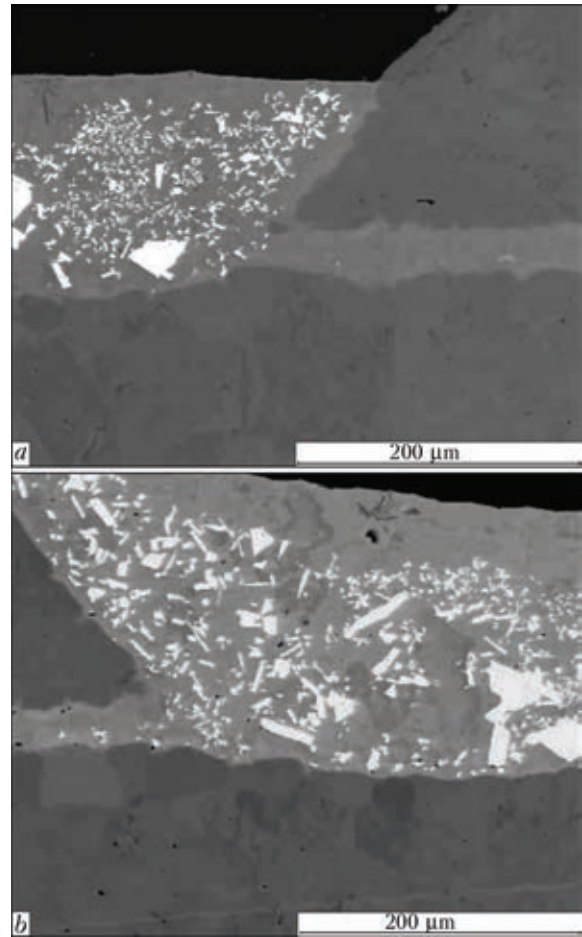


**Figure 6.** Joints of Ni–Al alloy made by BFA VPr27 in the state after brazing (a) and heat treatment at 1050 °C for 30 min (b)

In some regions it is precipitated in the form of separate light grains. Single pores are also observed (Figure 7). Grey matrix of seam, i.e. the zone adjacent to material being brazed, is a solid solution on nickel base, containing about 7 wt.% Al and other elements in negligible amount. In the near-seam zone of base metal on nickel base the X-ray spectral microanalysis showed, except 13 wt.% Al, the presence of negligible amount of BFA alloying elements, wt.%: 0.24 Mo; 0.40 W; 0.24 Nb. Heat treatment at 1050 °C for 30 min had no influence on structure of brazed joints, the amount of composed phases and their size remained without changes (see Figure 6, b).

**Table 1.** Distribution of elements in examining regions during spreading of industrial BFA VPr27 over Ni–Al–Mo–Co–W alloy

Number of spectrum (see Figure 5)	Composition, wt.%							
	Al	Cr	Fe	Co	Ni	Nb	Mo	W
2	10.03	–	–	4.85	76.42	–	6.11	2.59
3	4.17	5.24	0.26	8.04	66.99	1.25	3.32	10.73
4	3.97	5.12	0.31	7.52	63.37	0.93	4.59	14.19
5	5.16	5.48	0.18	8.53	74.07	1.03	1.97	3.57

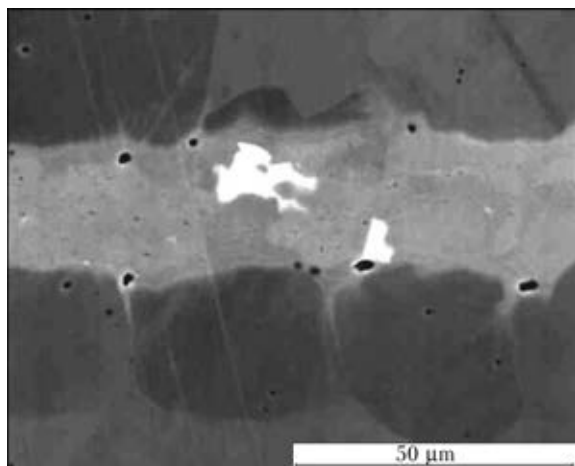


**Figure 7.** Microstructure of brazed seam on nickel aluminide made by BFA VPr27

Brazing at the same condition of alloy Ni–Al–Mo–Co–W, alloyed with refractory elements, differed by another formation of structure both in fillet regions and also in seams (Figure 8). Judging from results of X-ray spectral microanalysis, the seam matrix is the Ni-based solid solution alloyed by Al (7), Cr (5), Co (8), Mo (1), W (2). Phase of complex W-based composition, enriched by Mo (22), Ni (27), Cr (6 %), is pre-

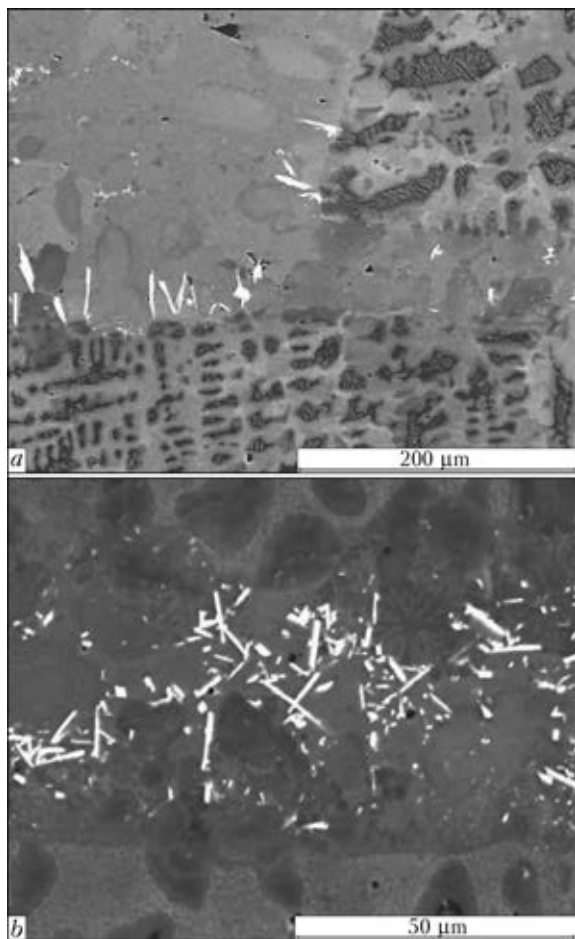


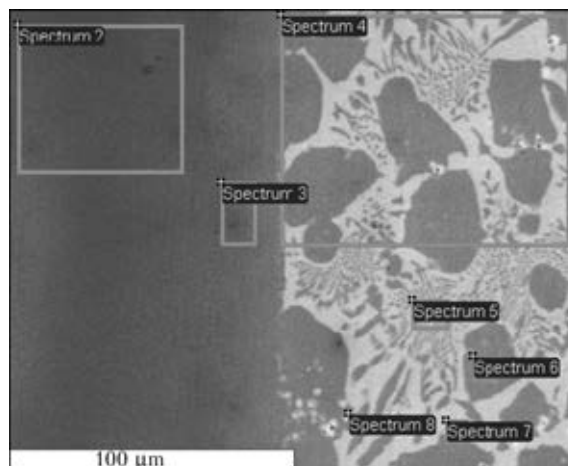
**Figure 8.** Structure of Ni–Al–Mo–Co–W alloy joint made by BFA VPr27 at  $T_b = 1170\text{ }^\circ\text{C}$ ,  $\tau = 3\text{ min}$ : *a* – fillet region; *b* – brazed seam

**Table 2.** Distribution of elements in examining regions of brazed joint of Ni–Al alloy in applying of Ni–Cr–Zr BFA

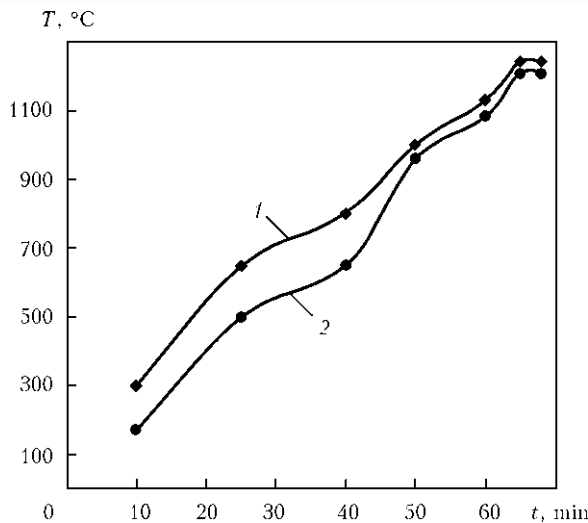
Number of spectrum (see Figure 9)	Composition, wt.%			
	Al	Cr	Ni	Zr
2	11.67	–	88.33	–
3	8.45	0.54	91.01	–
4	0.40	4.97	82.31	12.32
5	0.37	3.23	80.06	16.34
6	0.45	8.49	90.37	0.69
7	0.11	0.85	74.11	24.93
8	–	1.18	19.47	79.34

cipitated in the form of dispersed needle-like particles. Mass share of aluminium in these particles is decreased to 0.4 %. As to the morphological constitution this phase can be referred to the intermetallic compound on the base of refractory elements due to typical proper geometry peculiar to them (Figure 8). In the fillet region this phase occupies a rather low percent of the area (~ 1 %) as compared to the seam. The main structural component is the solid solution on Ni base (76 %), containing also such hardening alloying elements as Cr (6), Co (8), Al (4 %) and negligible share (by ~1.5 %) of rest elements, such as Nb, Mo and W.

The carried out investigations showed that the morphological constitution of brazed joints is affected not only by temperature-time parameters of technological process of brazing, but also by chemical composition of material being brazed. Thus, in use of alloyed Ni–14Al–5Mo–4Co–2.5W alloy as a base material the precipitates of W-enriched phase are observed in the form of dispersed needle-like particles of 1.5–2.0 μm width both in fillet region and also in brazed seam (see



**Figure 9.** Microstructure of Ni–Al alloy / Ni–Cr–Zr BFA interface



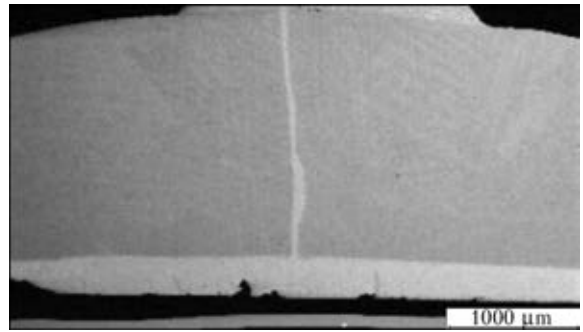
**Figure 10.** Thermogram in brazing by Ni-Cr-Zr BFA at  $T_b = 1170\text{ }^\circ\text{C}$ ,  $\tau = 3\text{ min}$ : 1 – thermocouple in chamber; 2 – on specimen

Figure 8). In brazing of binary Ni-14Al alloy the phase, enriched by tungsten, is precipitated in the form of rather coarse inclusions. In the fillet region their size is about  $40\text{ }\mu\text{m}$ , in seam it is about  $18\text{ }\mu\text{m}$ .

In addition, microstructure of molten BFA on intermetallic substrate is differed from that of brazed seam. This can be explained by the effect of geometric parameters (capillary gaps, length of base metal-BFA interface), as well as BFA amount on the proceeding of diffusion processes during heating. In spreading of Ni-Cr-Zr BFA over the substrate of binary Ni-Al alloy the zonal solidification is absent (see Figure 4 b; Figure 9). The molten BFA is solidified in the form of eutectic alloy formed by primary grains of solid solution on nickel base and intermetallic, containing up to 25 % Zr (see Figure 9, Table 2). Negligible amount of single dispersed precipitates of phase on zirconium (79.34 %) base is observed. Aluminium is not almost diffused into the molten BFA, that is confirmed by the results of X-ray spectral microanalysis.

Vacuum brazing of butt joints with Ni-Cr-Zr BFA was carried out at  $1210\text{ }^\circ\text{C}$  for 3 min holding. The temperature mode of brazing was recorded in the form of thermogram (Figure 10). In brazing of Ni-Al alloy and alloyed Ni-Al-Mo-Co-W alloy the BFA of Ni-Cr-Zr system is melted, material being brazed is wetted, and flow into capillary gap and to the reverse side of specimen with formation of full dense fillets (Figure 11), thus being the confirmation of good fluidity of the eutectic BFA.

After brazing the experimental specimens were cut into plates for further investigations. Metallographic examinations of brazed joints of intermetallic alloy Ni-14Al showed that Ni-Cr-



**Figure 11.** Macrosection of butt joint of Ni-Al alloy made by Ni-Cr-Zr BFA

Zr BFA can form sound seams of variable width from  $30\text{ up to }50\text{ }\mu\text{m}$ . In the seam central zone the Ni-based eutectic phase, enriched with zirconium up to 7 wt.%, is solidified in the form of a thread-like band of  $5\text{ }\mu\text{m}$  width. At the joint boundary the zone of common grains of base metal is observed, where the seam in its classical conception is absent (Figure 12, b). It should be noted that concentration of zirconium in the dark part of seam does not exceed 0.49 wt.%, while aluminium concentration reaches 7 wt.%, that proves the proceeding of diffusion processes at the interface. X-ray spectral microanalysis determined that eutectics was formed by solid solution on nickel base and intermetallic phase, enriched with zirconium up to 21 % (Table 3, Figure 13).

After heat treatment of brazed joints at  $1150\text{ }^\circ\text{C}$  for 30 min the seam width was  $32\text{ }\mu\text{m}$ .

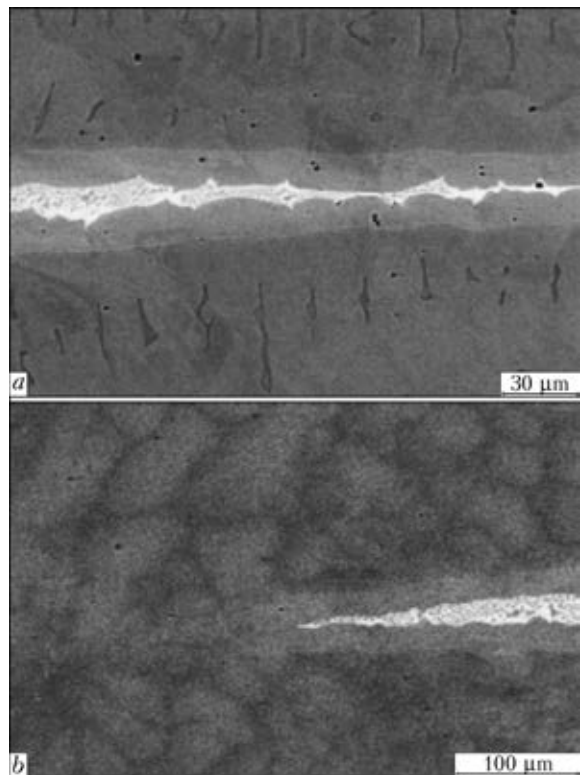


**Figure 12.** Microstructure of brazed seam on Ni-Al alloy made by Ni-Cr-Zr BFA (a), and zone of common grains of base metal (b)



**Table 3.** Distribution of elements in examining regions of brazed joint of Ni–Al alloy made by Ni–Cr–Zr BFA

Number of spectrum (see Figure 13)	Composition, wt.%						
	Al	Cr	Co	Ni	Zr	Mo	W
2	8.57	–	4.76	78.13	–	5.52	3.02
3	4.61	3.05	3.10	83.10	–	3.39	2.75
4	0.47	4.45	0.11	79.72	14.60	–	0.64
5	0.34	2.22	0.16	76.30	20.98	–	–
6	0.42	4.58	0.41	78.50	15.26	–	0.83
7	0.46	4.33	0.19	79.34	14.93	–	0.75

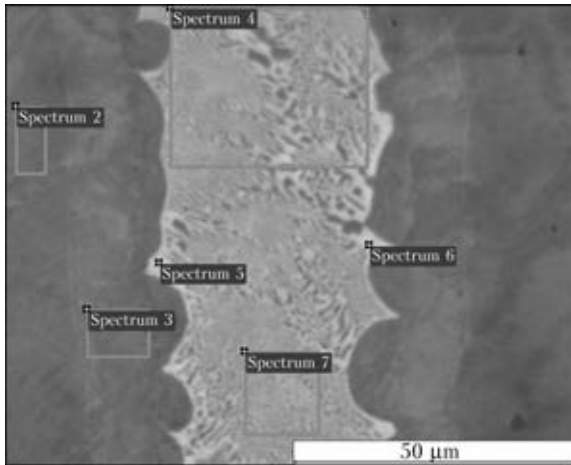


**Figure 13.** Regions of local microanalysis after brazing of Ni–Al alloy by Ni–Cr–Zr BFA

Composition of intermetallic phase, which is solidified in seam centre, is somewhat changed: on the background of light phase of zirconium intermetallic, containing 20–23 wt.% Zr, the second phase is formed in the form of globules of dark color of about 1.5 µm size, which contains 13–15 wt.% Zr. Precipitates of dark phase (solid solution) in some seam regions has a continuous nature, their composition corresponds to compound 87.66Ni–6.76Al–4.59Cr–0.99Zr.

The seam zone, adjacent directly to base metal, contains about (wt.%) 1Zr, 6–7Al, 4Cr. After 30 min holding at 1150 °C due to diffusion processes between the material being brazed and

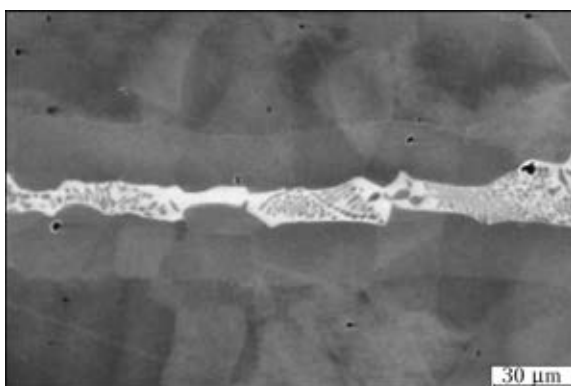


**Figure 14.** Eutectic structure of brazed seam (Ni–Al alloy, Ni–Cr–Zr BFA) after heat treatment at 1150 °C for 30 min

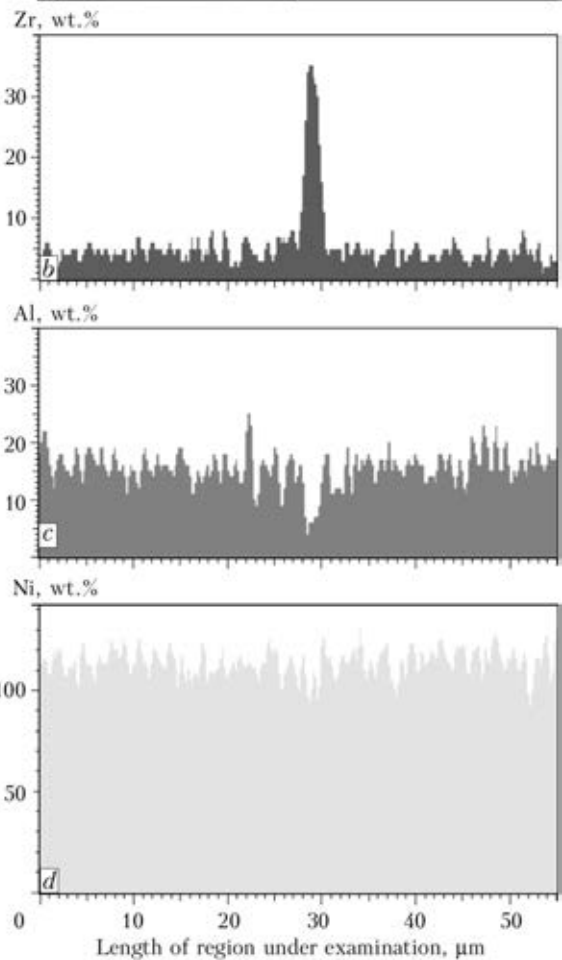
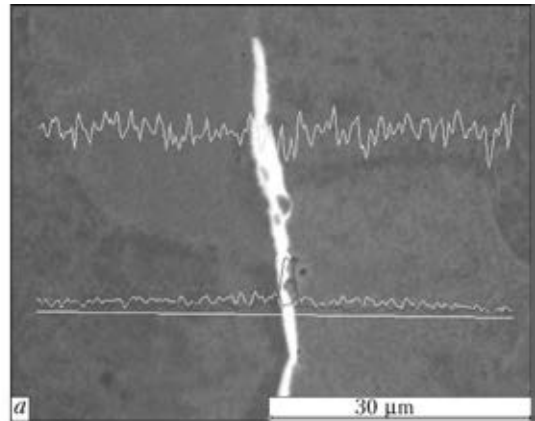


**Figure 15.** Microstructure (a) and distribution of zirconium (b), aluminium (c) and nickel (d) in brazed seam (Ni–Al alloy, Ni–Cr–Zr BFA)



seam metal the concentration of chromium and zirconium is increased in the latter by approximately 1 wt.%. In seams the eutectic structure is retained (Figure 14). The increase in time of holding up to 60 min did not show any effect on structure of seams: in central part the Zr-enriched eutectic is solidified; concentration of aluminium is reduced negligibly, and nickel concentration is not changed.

The conclusion was made on the basis of carried out investigations that eutectic BFA of Ni–Cr–Zr system have a good spreading over the nickel aluminide (contact angle of wetting is 6°), flow into vertical capillary gaps and form the sound seams with eutectic structure. In specimen length the rather homogeneous seam regions are formed, in which the interlocking grains of base metal are observed.

Metallographic examinations are the intermediate stage in the BFA development. The works of the next stage will include the determination of mechanical properties of brazed joints.

1. Grinberg, B.A., Ivanov, M.A. (2002) *Ni<sub>3</sub>Al intermetallics: Microstructure, deformation behavior*. Ekaterinburg.
2. Povarova, K.B., Kazanskaya, N.K., Buntushkin, V.P. et al. (2003) Thermostability of structure of alloy based on Ni<sub>3</sub>Al and its application in blades of small-sized gas turbine engines. *Metally*, **3**, 95–100.
3. Buntushkin, V.P., Kablov, E.N., Bazyleva, O.A. et al. (1999) Alloys based on nickel aluminides. *MiTOM*, **1**, 32–34.
4. Buntushkin, V.P., Bronfin, M.B., Bazyleva, O.A. et al. (2004) Influence of alloying and structure of castings on heat resistance of Ni<sub>3</sub>Al intermetallics at high temperature. *Metally*, **2**, 107–110.
5. Kablov, E.N., Buntushkin, V.P., Povarova, K.B. et al. (1999) Low alloy light heat-resistant high-temperature materials based on Ni<sub>3</sub>Al intermetallics. *Ibid.*, **1**, 58–65.
6. Khorunov, V.F., Perevezentsev, B.N., Ubirajlo, O.G. (2013) Examination of structure and chemical heterogeneity of joints of intermetallic Ni<sub>3</sub>Al alloy. In: *Proc. of Int. Sci.-Techn. Conf. on Brazing*, 255–264. Toliatti: TGU.
7. Khorunov, V.F., Maksymova, S.V. (2013) *Prospective systems of filler metals for brazing of heat-resistant alloys based on nickel and titanium. Physical-technical problems of modern materials science*, Vol. 1, 105–134. Kiev: Akadempriodika.

Received 12.03.2014



# INFLUENCE OF HEATING RATE ON INFLAMMATION TEMPERATURE OF MULTILAYER Ti/Al FOIL

D.N. KUZMENKO, A.I. USTINOV, S.G. KOSINTSEV and L.V. PETRUSHINETS

E.O. Paton Electric Welding Institute, NASU

11 Bozhenko Str., 03680, Kiev, Ukraine. E-mail: office@paton.kiev.ua

Self-sustaining exothermal reaction of synthesis in multilayer foil consisting of intermetallic forming elements may proceed by means of self-propagation of high-temperature synthesis reaction front through foil (self-propagating high-temperature synthesis (SHS) or as a result of synthesis reaction running through the entire volume (autoinflammation (AI)). The latter is realized under the condition of foil heating up to a certain critical temperature, at which the synthesis reaction runs in the entire volume without external heat supply. In the work influence of foil heating rate on AI temperature was studied in the case of Ti/Al multilayer foil. It is shown that there exists a certain critical heating rate, below which foil AI is not observed, and at heating rates above the critical rate AI temperature decreases with increase of heating rate. Dependence of AI temperature on heating rate is nonmonotonic: at low heating rates AI temperature abruptly decreases, and at further increase of heating rate AI temperature remains practically unchanged. Such nonmonotonic dependence of foil AI temperature on heating rate is associated with running of the process of thermally activated solid phase reactions in it, which are accompanied by formation of intermetallic interlayers on the boundary between titanium and aluminium layers, preventing diffusion mixing of elements. With increase of heating rate, interlayer thickness decreases, promoting AI temperature lowering. 11 Ref., 4 Figures.

**Keywords:** multilayer foil, autoinflammation, electron beam vacuum deposition, thermal explosion, heat evolution

It is known that consolidated systems, based on elements capable of entering into synthesis reaction, have become widely applied, primarily due to the possibility of synthesizing refractory compounds, intermetallics and ceramics in the reaction process, as well as depositing coatings on their base, and producing permanent joints [1, 2]. The latter is due, mainly, to the fact that the synthesis process in such systems is accompanied by intensive heat evolution, which is sufficient for realization of welding or brazing process with limited use of external energy sources [3–5]. In the case of local heating of the joint zone through reaction of self-propagating high-temperature synthesis (SHS), heat removal is an essential factor, limiting its application [6]. Conditions for initiation of autoinflammation (AI) in multilayer foil were studied only on powder materials. Therefore, practical implementation of this approach in welding requires determination of the conditions for AI initiation in the multilayer system.

It is known that the nature of heat evolution depends on the method of solid-phase reaction initiation in the system [7]. If system preheating is performed locally, solid-phase reaction can be

initiated in the heating area, which will be capable of propagation through the system without external heat supply (SHS-reaction). Here, heat evolution will be localized, chiefly, on the reaction front [7, 8]. When the entire system volume is uniformly heated up to the temperature of synthesis reaction initiation in it (AI temperature), heat evolution proceeds in the entire volume. This allows achieving the maximum intensity of its evolution (thermal explosion) [2].

It is believed that to ensure the conditions of SHS process realization in a reaction system it is necessary to apply a heat pulse, the power of which is commensurate with the heat of intermetallic formation, and for AI the system must be heated to a certain critical temperature, at which the synthesis reaction will run without additional heat supply [2, 8].

First experimental studies of AI conditions were conducted on systems, produced by consolidation of powders of pure elements [1, 2]. In the case of systems with high heat of intermetallic formation, such as Ni/Al, Ti/Al, etc., it was shown that for AI initiation the system had to be heated up to aluminium melting temperature. The latter is due to the fact that in powder materials individual particles are covered by oxide film, and its breaking up is the necessary condi-



tion of the start of reaction between them. Aluminium oxide film is the most stable (aluminium oxide melting temperature is 2040 °C), so that its removal from aluminium particle surface at low temperatures is impossible. It turned out, however, that it is enough to break up the oxide film integrity to start diffusion interaction between the elements. This can be achieved, for instance, at aluminium melting. Owing to bulk effect at its melting, the oxide shell on aluminium particles cracks and aluminium, flowing out of the particle, enters into a reaction with another element [2].

In multilayer systems, produced in the process of layer-by-layer vacuum deposition of intermetallic-forming elements, the situation is different. In this case there is no barrier in the form of oxide film between element layers, hampering their diffusion interaction. Therefore, already at slight heating of such a multilayer structure, element diffusion reaction can run in it [2]. It is clear that such a reaction system structure will have an essential influence on the conditions of synthesis reaction initiation in it. So, for instance, according to results of [7], AI of Ti/Al foil was observed at its heating up to the temperature of about 350 °C.

At the same time, it is known that solid-phase reactions in Ti/Al foil run intensively already at temperatures of about 300 °C, that is accompanied by formation of intermetallic phase interlayers on layer boundaries. The formed intermetallic layers can be barriers for diffusion mixing of elements. It was theoretically shown earlier that presence of such an interlayer has an essential influence on propagation velocity of SHS reaction front [9]. It can be assumed that depending on the rate, at which the foil is heated, the interlayer thickness will change, that should influence its AI temperature.

In this work dependence of foil AI temperature on heating rate was studied in the case of Ti/Al multilayer foil.

**Experimental procedure.** Multilayer Ti/Al foils, consisting of alternating layers of titanium and aluminium, were produced by the method of layer-by-layer electron beam deposition of elements on horizontally rotating substrate, fixed on a vertical shaft, by the procedure described in [10]. Microstructural analysis of foil cross-section (Figure 1) showed that layer alternation period (i.e. thickness of Ti + Al multilayer) was equal to 68 nm at total thickness of multilayer film of 26 µm.

Schematic of the setup for AI temperature measurement is shown in Figure 2. Features of

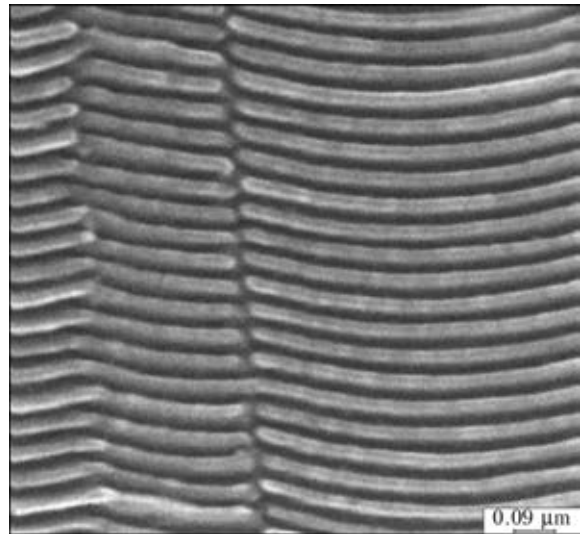


**Figure 1.** Cross-sectional microstructure of foil obtained by SEM (light strips correspond to titanium layers, dark strips are aluminium layers)

the procedure are due to small weight (of about 50 mg) and small thickness (26 µm) of samples. To reduce the influence of external factors and lower heat losses in the sample, the measuring block, in which the multilayer foil was placed, was shielded by aluminium foil.

AI process was studied with application of mechanically cut out strips of multilayer foil 1.5 cm wide and 2.5–3.0 cm long. The studied strip was fastened by its ends in a holder of nichrome filaments. Foil was heated by infrared radiation from a flat heater made from nichrome wire, which was located under the foil at a fixed distance. Heater power and radiation heating intensity, accordingly, were selected so as to ensure the specified foil heating rate, close to a linear one, right up to AI temperature. Sample temperature was taken by two chromel-alumel ther-

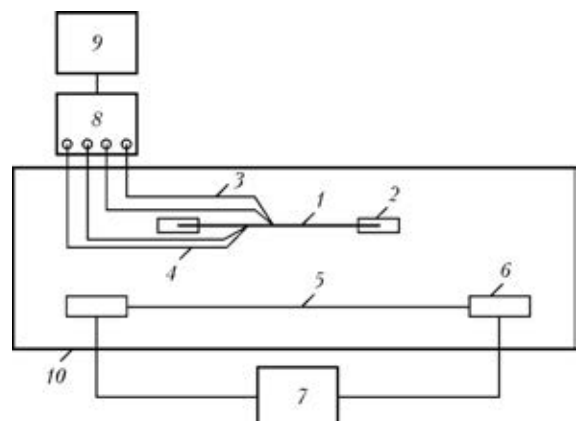


**Figure 2.** Schematic of experimental set up: 1 – sample; 2 – holder; 3, 4 – upper and lower thermocouple, respectively; 5 – nichrome holder; 6 – copper contacts; 7 – laboratory autotransformer; 8 – ADC; 9 – computer; 10 – aluminium shield



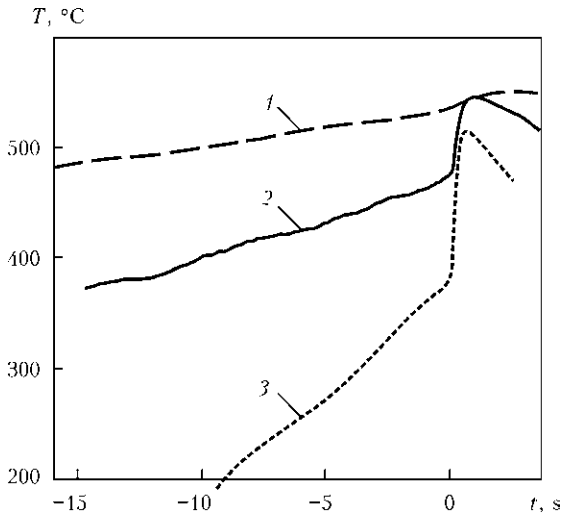


**Figure 3.** Dependence of temperature on time at constant heating with rates of 2.5 (1), 4.6 (2) and 21.2 (3) °C/s

mocouples of 0.7 mm thickness, which were in contact with the sample from two sides.

Thermocouple readings were recorded by an analog-digital converter (ADC) with data entering into a computer. Difference of thermocouple readings on foil opposite surfaces was within 30–50 °C in the entire studied temperature range. Mean temperature by two thermocouple readings was taken as sample temperature.

**Results and their discussion.** Figure 3 shows thermograms of heating of Ti/Al foil at different rates. Moment of the start of an abrupt jump of foil temperature (multilayer foil AI) is taken as process count time. Mean heating rate was determined by the slope of straight line section, approximately 200 °C before AI, which describes dependence of temperature on time in the best way. It is seen that foil temperature rises uniformly at the specified rate up to achievement of

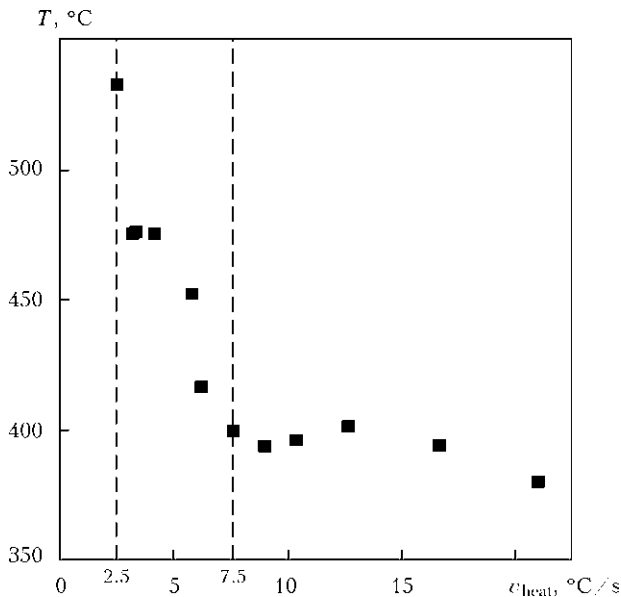


**Figure 4.** Dependence of multilayer foil inflammation temperature on its heating rate

a certain critical value, at which its abrupt rise (jump) takes place. Such abrupt temperature rise is accompanied by bright glowing through the entire foil volume, that is indicative of intensive heat evolution as a result of running of solid phase reaction (AI).

Presented thermograms show that with lowering of heating rate foil temperature at the moment of AI rises, and at rates below 2.5 °C/s (critical rate) no AI of foil is observed. Note that foil inflammation temperature, obtained for different heating rates, is in the range of 350–500 °C that is by 200–300 °C lower than the temperature of inflammation of powder samples of a similar composition (Ti + Al) [1, 2].

As is seen from the thermograms, presented in Figure 3, foil AI takes place at different temperatures of the sample. AI temperature changes markedly, depending on foil heating rate. For instance, for heating rate of 21.2 °C/s (3) it is 380 °C, while for 4.6 °C/s (2) it is 475 °C.

Moreover, note the fact that at heating rate lowering, magnitude of sample temperature jump at AI decreases right to its complete disappearance at foil heating at rates below the critical one. As sample temperature is determined mainly by the quantity of elements, entering into the reaction at the moment of AI, from thermogram analysis it can be assumed that with lowering of foil heating rate the volume fraction of elements, which have not reacted before the start of AI process, becomes smaller.

Measurements were the basis for plotting the dependence of AI temperature on heating rate, shown in Figure 4. Obtained data show that foil AI is realized for heating rate higher than a certain critical value  $v_{cr} \sim 2.5$  °C/s. For the case of heating rates below 2.5 °C/s no AI indications were observed, that corresponds to quasistationary running of intermetallic forming reaction. At heating rates higher than the critical value, AI temperature changes. Its dependence on heating rate can be conditionally divided into two ranges: in the first range (2.5–7.5 °C/s) AI temperature decreases markedly with increase of heating rate, and in the second one (at rates higher than 7.5 °C/s) AI temperature is weakly dependent on heating rate.

Thus, three qualitatively different patterns of running of the reaction of intermetallic formation in multilayer foil can be in place, depending on its heating rate. In the case of heating rates below  $v_{cr}$ , solid phase reaction runs under the condition of continuous increase of foil temperature. As intensity of reaction running is determined by two factors, namely temperature, increase of





which enhances the diffusion mobility of atoms, and thickness of intermetallic interlayer between the reactive layers, increase of which prevents diffusion mixing of elements, it can be assumed that at heating rates below the critical one increase of interlayer thickness occurs faster than diffusion mobility is increased. It follows that at heating rates above the critical one, at achievement of AI temperature the intermediate interlayers formed at foil heating up to this temperature, did not prevent intensive diffusion mixing of elements.

It is clear that with increase of heating rate interlayer thickness will decrease that promotes AI temperature lowering. This accounts for lowering of AI temperature in the range of heating rates from  $v_{cr}$  to a certain transition rate  $v_{tr}$ , above which AI temperature practically does not change at further increase of heating rate. At such rates of heating above  $v_{tr}$ , intermetallic interlayer, apparently, does not have enough time to form up to the moment of reaction start and structure of multilayer foils heated at different rates practically does not differ from each other at the moment of AI.

Results of works [9, 11] can be proof of the fact that it is exactly intermetallic interlayer thickness dependent on heating rate that influences AI temperature in the long run. In these studies it was shown that velocity of SHS-reaction front propagation slows down with increase of interlayer thickness, and at a certain critical thickness SHS process can be inhibited.

Thus, in the case of Ti/Al multilayer foil it was shown that its AI temperature depends non-linearly on heating rate. There exists a threshold rate of foil heating (in this case  $v_{cr} \sim 2.5$  °C/s), at which its AI does not take place. At increase of heating rate above the critical one (in the range of 2.5–7.5 °C/s) an abrupt lowering of the temperature of AI is observed (from 530 °C

at the rate of 2.5 °C/s to 400 °C for 7.5 °C/s), which slows down and becomes weakly dependent on heating rate, when its certain transition value has been reached (above  $v_{tr} \sim 7.5$  °C/s). The established non-linear dependence of temperature of multilayer foil AI on its heating rate is associated with a change of its structure, as a result of formation of an intermediate interlayer on the interface of titanium and aluminium layers during heating up to temperatures, at which intensive diffusion mixing of elements can occur.

1. Merzhanov, A.G. (1983) *Self-propagating high-temperature synthesis*. Moscow: Khimiya.
2. Merzhanov, A.G. (2000) *Solid flame combustion*. Chernogolovka: ISMAN.
3. Ustinov, A.I., Falchenko, Yu.V., Ishchenko, A.Ya. et al. (2008) Diffusion welding of gamma-TiAl alloys through nanolayered foil of Ti/Al system. *Intermetallics*, **16**, 1043–1045.
4. Wang, J., Besnoin, E., Duckham, A. et al. (2003) Room temperature soldering with nanostructured foils. *Appl. Phys. Lett.*, **83**, 3987–3989.
5. Duckham, A., Spey, S.J., Wang, J. et al. (2004) Reactive nanostructured foil used as a heat source for joining titanium. *J. Appl. Phys.*, **96**, 2336–2342.
6. Zaporozhets, T.V., Gusak, A.M., Ustinov, A.I. (2011) Conditions of propagation of the SHS reaction front in nanolayered foils in contact with heat-conducting material. *The Paton Welding J.*, **8**, 37–41.
7. Rogachev, A.S., Grigoryan, A.E., Illarionova, E.V. et al. (2004) Gas-free combustion of multilayer bimetallic Ti/Al nanofoils. *Fizika Goren. i Vzryva*, **40**(2), 45–51.
8. (2003) *Concept of SHS development as a field of scientific-technical progress*, 7–12, 92–108. Chernogolovka: Territoriya.
9. Zaporozhets, T.V., Gusak, A.M., Korol, Ya.D. et al. (2013) Inverse problem for SHS in multilayer nanofoils: Prediction of process parameters for single-stage SHS reaction. *Int. J. SHS*, **22**(4), 217–226.
10. Ishchenko, A.Ya., Falchenko, Yu.V., Ustinov, A.I. et al. (2007) Diffusion welding of finely-dispersed AMg5/27 % Al<sub>2</sub>O<sub>3</sub> composite with application of nanolayered Ni/Al foil. *The Paton Welding J.*, **7**, 2–5.
11. Trenkle, J.C., Koerner, L.J., Tate, M.W. et al. (2008) Phase transformations during rapid heating of Al/Ni multilayer foils. *Appl. Phys. Lett.*, **93**, 081903.

Received 18.09.2014



# IMPROVEMENT OF THE PROCEDURE OF MODE PARAMETER CALCULATION FOR GAS-SHIELDED MULTIPASS WELDING

D.S. BUZORINA<sup>1, 2</sup>, M.A. SHOLOKHOV<sup>2</sup> and M.P. SHALIMOV<sup>1</sup>

<sup>1</sup>Ural Federal University

19 Mira Str., 62002, Ekaterinburg, RF

<sup>2</sup>SHTORM Ltd.

115 Narodnoj Voli Str., Ekaterinburg, RF. E-mail: ekb@shtorm-its.ru

Application of automatic and robotic welding systems in modern welding fabrication requires development of algorithms for welding mode parameter control, namely parameter assigning and adaptive correction, depending on conditions. In addition to the main parameters of welding mode (welding current, voltage, speed) and groove geometry, electrode extension and shielding gas composition also have their effect on parameters, determining weld formation and effectiveness of using arc thermal energy for welded joint formation. Dependences of bead cross-sectional area and total thermal efficiency of welding process on electrode extension and shielding gas composition were experimentally established. These dependences were taken into account when improving the earlier developed procedure for calculation of welding mode parameters. Equations take into account both the technological parameters (groove angle, electrode position in the groove, welding speed), and shielding gas composition and electrode extension. 7 Ref., 2 Figures.

**Keywords:** *multipass arc welding, consumable electrode, total thermal efficiency, coefficient of areas, welding mode parameters*

In welding technology design an important moment is determination of welding mode parameters, providing welded joints with specified characteristics. Broad application of automatic and robotic welding systems in modern welding fabrication requires development of algorithms of welding mode parameter control, namely assigning and adaptive correction of parameters, depending on conditions. Adaptive correction of welding modes should be based on accurate determination of the influence of each of the process parameters and their combination on weld performance [1]. Most of mathematical models, constructed for welding process control, are based on statistical dependences between energy parameters of welding mode (welding current, arc voltage, speed, etc.) and parameters characterizing welded joint quality (geometrical characteristics, mechanical properties, etc.) [2].

Work [3] proposes a procedure of parameter calculation, which is based on the results of investigation of the influence of technological factors (groove angle  $\alpha$ , electrode position in the groove  $x$ , welding speed  $v_w$ ) on parameters determining weld formation and effectiveness of arc thermal energy utilization for welded joint formation.

Analysis of literature data showed that in addition to main welding mode parameters (current, voltage, speed) and groove geometry, allowed for in the above-mentioned procedure [3], the studied parameters (bead cross-sectional area and thermal efficiency of welding process) are also influenced by electrode extension [4] and shielding gas composition [4, 5].

It is known that shielding gas composition has a significant influence on technological characteristics and penetration shape. At constant voltage at increase of CO<sub>2</sub> fraction up to 50 % in the mixture, the arc becomes shorter, the weld is narrower, penetration depth and bead height become greater, and penetration area increases [4].

Electrode extension in continuous wire welding influences welding process stability. This is due to variation of electrode heating in the extension by passing current. Admissible electrode extension depends on its diameter, specific electric resistance and welding current. At small extensions welding zone visibility is impaired, and partial melting of current conduit is possible, and at large extensions process stability can be disturbed. Extension increase allows increasing the coefficient of electrode melting and reduces penetration depth [4]. By the data of [6] at increase of electrode extension the weld width and penetration depth decrease (all other conditions being equal), and weld convexity becomes greater. Mechanism of electrode extension influence on penetration depth consists in that at in-



creased extension the amount of deposited metal becomes greater, liquid metal flowing under the arc is intensified; effect of shielding of unmolten base metal by liquid metal interlayer is manifested, leading to shallower penetration of metal being welded [7].

Thus, for practical application of the procedure of calculation of multipass welding mode parameters [3], for instance, in development of algorithms of welding mode parameter control, the equations should allow for both the main process parameters (groove angle, electrode position in the groove, welding speed), and shielding gas composition and electrode extension, which influence weld formation.

The objective of this work is establishing dependences between parameters, characterizing weld formation and welding process parameters, in particular shielding gas composition and electrode extension, as well as determination on the basis of derived dependences of multipass welding mode parameters, ensuring absence of lacks-of-fusion.

In the general form equations for determination of bead cross-sectional area and total thermal efficiency can be expressed as follows:

$$F_b = F_b^v(\alpha, x, v_w) \theta_I^F(I_w) \theta_{\%CO_2}^F(\%CO_2) \theta_{l_e}^F(l_e), \quad (1)$$

$$\eta_t = \eta_t^v(\alpha, x, v_w) \theta_I^\eta(I_w) \theta_{\%CO_2}^\eta(\%CO_2) \theta_{l_e}^\eta(l_e), \quad (2)$$

where  $F_b^v(\alpha, x, v_w)$ ,  $\eta_t^v(\alpha, x, v_w)$  are the functions of dependence of bead cross-sectional area and thermal efficiency on groove angle, electrode position in the groove, welding speed, respectively, and are found from formulas given in [3]:

$$F_b = (47.5 - 0.031\alpha + 4.21x - 0.956v_w - 0.113\alpha x + 0.003\alpha v_w - 0.143xv_w + 0.004\alpha xv_w)(0.0134I_w - 1.559); \quad (3)$$

$$\eta_t = (0.125 - 0.006\alpha + 0.018x + 0.024v_w + 0.00006\alpha^2 + 0.0006x^2 - 0.0005v_w^2 - 0.0005\alpha x + 0.00012\alpha v_w - 0.00013xv_w)(0.0047I_w + 0.084), \quad (4)$$

where  $F_b$  is the bead cross-sectional area, mm<sup>2</sup>;  $\eta_t$  is the total thermal efficiency of welding process;  $\alpha$  is the groove angle, deg;  $x$  is the electrode position in the groove, mm;  $v_w$  is the welding speed, m/h;  $I_w$  is the welding current, A;  $\theta_I^F(I_w)$ ,  $\theta_{\%CO_2}^F(\%CO_2)$ ,  $\theta_{l_e}^F(l_e)$  are the functions of dependence of bead cross-sectional area on welding current, shielding gas composition (percentage of CO<sub>2</sub> in Ar + CO<sub>2</sub> mixture) and electrode extension, respectively;  $\theta_I^\eta(I_w)$ ,  $\theta_{\%CO_2}^\eta(\%CO_2)$ ,  $\theta_{l_e}^\eta(l_e)$  are the functions of dependence of total thermal

efficiency of welding process on welding current, shielding gas composition (percentage of CO<sub>2</sub> in Ar + CO<sub>2</sub> mixture) and electrode extension, respectively.

A number of experiments were performed to determine functions

$$\theta_I^F(I_w), \theta_{\%CO_2}^F(\%CO_2), \theta_{l_e}^F(l_e), \\ \theta_I^\eta(I_w), \theta_{\%CO_2}^\eta(\%CO_2), \theta_{l_e}^\eta(l_e).$$

When studying the influence of electrode wire extension and shielding gas composition, the following two assumptions were made: shielding gas composition and electrode wire extension have an influence independent on earlier studied parameters ( $I$ ,  $U_a$ ,  $v_w$ ,  $x$ ,  $\alpha$ ) on bead cross-sectional area and total thermal efficiency of welding process, and shielding gas composition and electrode wire extension do not have any mutual influence on bead cross-sectional area and total thermal efficiency of the welding process.

Experimental data were used to plot graphs of the influence of electrode extension on bead cross-sectional area and on total thermal efficiency of the welding process (Figure 1).

Graphs given in Figure 1, *a*, show that at increase of welding current in the studied range the nature of bead cross-sectional area dependence on electrode extension practically does not change. Therefore, at determination of  $F_b$  the earlier assumption of absence of mutual influence

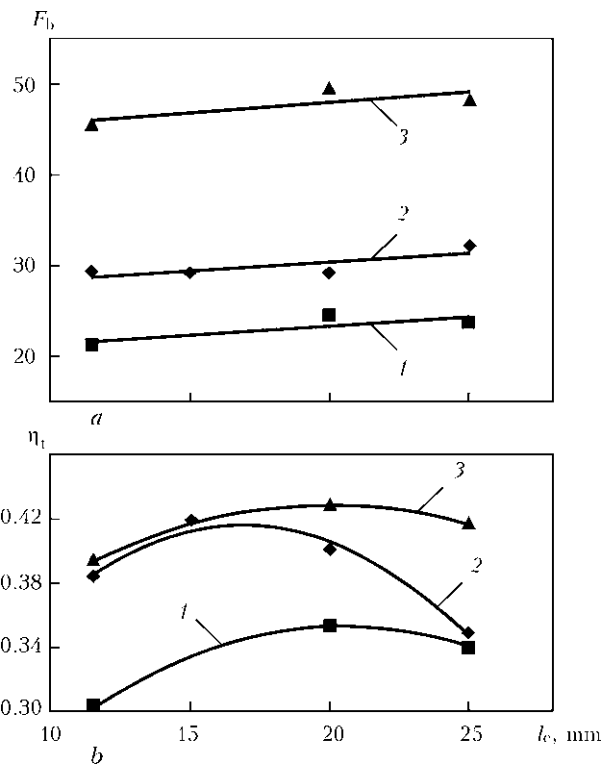


Figure 1. Influence of electrode extension on bead cross-sectional area (*a*) and on total thermal efficiency of welding process (*b*): 1 – 180; 2 – 220; 3 – 260 A



of  $l_e$  and  $I_w$  on  $F_b$  can be taken. After processing experimental results, the function of dependence of bead cross-sectional area on electrode extension can be written in the following form:

$$\theta_l^F(l_e) = 0.001l_e + 0.956. \quad (5)$$

Another shape of the dependence is observed at consideration of the influence of electrode extension on total thermal efficiency of the welding process (Figure 1, b). Analysis of the derived results shows that at increase of welding current the nature of electrode extension influence on total thermal efficiency changes, and, therefore, a conclusion can be made about mutual influence of  $l_e$  and  $I_w$  on  $\eta_t$  of the welding process. Function  $\theta_l^\eta(l_e)$  can be presented in the form of a quadratic polynomial of two arguments ( $I_w, l_e$ ), and after processing experimental data by regression analysis it is expressed as follows:

$$\theta_l^\eta(l_e) = -I_w^2 \cdot 10^{-4} - 0.001l_e^2 + 0.05I_w + 0.03l_e - 3.98. \quad (6)$$

Figure 2 shows the response surface of function  $\theta_l^\eta(l_e)$ , depending on welding current and electrode extension.

Derived results and data presented provide indirect confirmation of earlier conclusions [3] about complex mutual influence of welding mode parameters on weld formation. There exists a combination of factors providing maximum effective application of arc energy.

When studying the shielding gas composition, it was found that at increase of  $CO_2$  fraction in shielding gas mixtures (from 0 up to 30 %) bead cross-sectional area becomes greater. In this case, increase of bead cross-sectional area is due to enlargement of penetration area, that is in agreement with the known literature data [5].

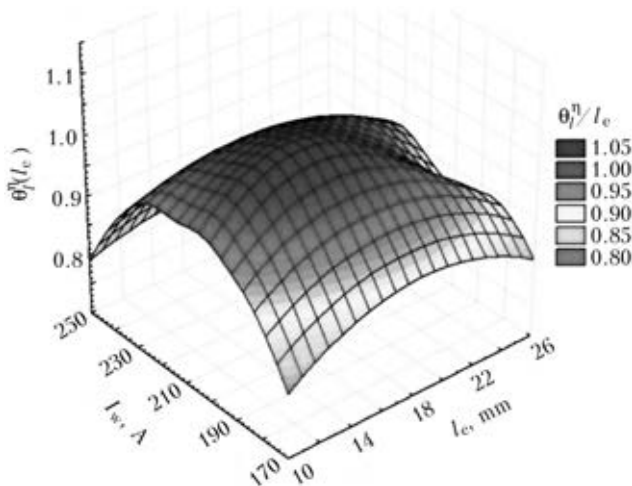


Figure 2. Response surface of function  $\theta_l^\eta(l_e)$  depending on welding current and electrode extension

Processing of experimental results yielded functions of dependence of bead cross-sectional area and thermal efficiency on  $CO_2$  percentage, respectively:

$$\theta_l^F(\%CO_2) = 0.003 \cdot \%CO_2 + 0.945, \quad (7)$$

$$\theta_l^\eta(\%CO_2) = 0.003 \cdot \%CO_2 + 0.907. \quad (8)$$

Then general equations (3) and (4) will become:

$$F = (47.5 - 0.03\alpha + 4.21x - 0.96v_w - 0.113\alpha x + 0.003\alpha v_w - 0.143xv_w + 0.004\alpha xv_w) \times (0.013I_w - 1.56)(0.001l_e + 0.956) \times (0.003 \cdot \%CO_2 + 0.945),$$

$$\eta_t = (0.125 - 0.006\alpha + 0.018x + 0.024v_w + 0.00006\alpha^2 + 0.0006x^2 - 0.0005v_w^2 - 0.0005\alpha x + 0.00012\alpha v_w - 0.00013xv_w)(0.005I_w + 0.084)(-I_w^2 \cdot 10^{-4} - 0.001l_e^2 + 0.05I_w + 0.03l_e - 3.98)(0.003 \cdot \%CO_2 + 0.907).$$

Considering the dependences earlier proposed by authors in [3] and derived in this work, dependences of bead cross-sectional area and thermal efficiency on electrode extension (5), (6) and  $CO_2$  percentage (7), (8), equations for determination of welding mode parameters can be presented as follows:

- welding current:

$$I_w = \frac{-b + \sqrt{b^2 - 4ac}}{2a}, \text{ A}; \quad (9)$$

- coefficients  $a, b$  and  $c$  are found from formulas

$$a = -0.015 \frac{\pi d^2}{F_d},$$

$$b = 0.64 + 0.06x + \frac{\pi d^2}{F_d} (3.34 + 0.35x - 0.01\alpha),$$

$$c = -74.05 + 0.05\alpha - 6.56x - \frac{\pi d^2}{F_d} (185.97 - 0.6\alpha x - 0.58\alpha + 27.81x) - \frac{(1 + \kappa)F_d}{(0.001l_e + 0.956)(0.003 \cdot \%CO_2 + 0.945)},$$

where  $d$  is the electrode diameter, mm;  $F_d$  is the deposited metal area,  $mm^2$ ;  $\kappa$  is the coefficient of areas (in consumable electrode welding in the used modes  $\kappa = 0.18-4$ );

- voltage

$$U_{ef} = \frac{B_{ef}v_{w.f}}{\eta_t I_w}, \text{ V}; \quad (10)$$

- value of coefficient  $B_{ef}$  is determined by formula



$$B_{ef} = \gamma_m H_{melt} \frac{(1+k)}{4} \pi d^2;$$

• value of thermal efficiency of welding process is found from formula

$$\begin{aligned} \eta_t = & (0.125 - 0.006\alpha + 0.018x + 0.024v_w + \\ & + 0.00006\alpha^2 + 0.0006x^2 - 0.0005v_w^2 - 0.0005\alpha x + \\ & + 0.00012\alpha v_w - 0.00013xv_w)(0.0047I_w + \\ & + 0.084)(-I_w \cdot 10^{-4} - 0.001I_e^2 + 0.05I_w + 0.003I_e - \\ & - 3.98)(0.003\%CO_2 + 0.91), \end{aligned}$$

where  $\gamma_m$  is the specific metal density, kg/m<sup>3</sup>;  $H_{melt}$  is the enthalpy at melting temperature allowing for latent heat of melting, J/kg;  $k$  is the fusion coefficient;

• welding speed

$$v_w = \frac{\pi d^2(0.078I_w - 8.32) \cdot 60}{4F_d}, \text{ m/h.} \quad (11)$$

### Conclusions

1. Functions of dependence of welding process thermal efficiency and bead cross-sectional area on electrode extension and shielding gas composition were derived in the analytical form.

2. Derived equations for calculation of parameters of the mode of multipass mechanized gas-shielded welding on the basis of determination of total thermal efficiency of welding process

allow calculation of welding modes (with the accuracy of about 12 %) under the condition of guaranteed penetration (at specified coefficient of areas). These equations allow for both process parameters (groove angle, electrode position in the groove, welding speed), and shielding gas composition and electrode extension. Equations can be applied in development of the technology of multipass welding of carbon, low- and medium-alloyed steels in argon-based mixtures of shielding gases.

1. Poloskov, S.I., Erofeev, V.A., Maslennikov, A.V. (2005) Determination of optimal parameters of automatic orbital welding based on computer modeling. *Svarochn. Proizvodstvo*, **10**, 6–13.
2. Lebedev, V.A. (2011) Control of penetration in mechanized welding and surfacing. *Ibid.*, **1**, 3–11.
3. Sholokhov, M.A., Buzorina, D.S. (2013) Calculation of mode parameters of wall bead deposition in down-hand multi-pass gas-shielded welding. *The Paton Welding J.*, **7**, 61–65.
4. Potapievsky, A.G. (1974) *Consumable electrode shielded-gas welding*. Moscow: Mashinostroenie.
5. Lashchenko, G.I. (2006) *Methods of consumable electrode arc welding*. Kiev: Ekotekhnologiya.
6. Zhernosekov, A.M. (2004) Effect of electrode stick-out on weld parameters in pulsed-arc welding of steels. *The Paton Welding J.*, **8**, 51–52.
7. Berezovsky, B.M. (2003) *Mathematical model of arc welding*. Vol. 2: Mathematical modeling and optimization of different type weld formation. Chelyabinsk: YuUrGU.

Received 26.02.2014

# FATIGUE CALCULATION FOR WELDED JOINTS OF BEARING ELEMENTS OF FREIGHT CAR BOGIE

L.M. LOBANOV, O.V. MAKHNENKO, G.Yu. SAPRYKINA and A.D. PUSTOVOJ

E.O. Paton Electric Welding Institute, NASU

11 Bozhenko Str., 03680, Kiev, Ukraine. E-mail: office@paton.kiev.ua

Statistics of accident rate at Ukrainian and Russian railways is an evidence of increase in the recent years of the accidents, related with failure of cast bearing elements of two-axle three-component freight car bogies. Analysis of service reliability of cast structures of side frame and bolster of 18-100 type bogie shows that appearance of fatigue cracks is the main reason of reject. It is reasonable to search an alternative application of welding technologies in manufacture of indicated parts from sheet products for the purpose of increase of their safety and survivability. It is shown that existing Norms for designing of welded joints and assemblies of railway cars significantly overstate real cyclic load resistance of welded joints in comparison with the Recommendations of the International Institute of Welding. This disadvantage is typical for number of reference documents acting in Russia and Ukraine, which regulate calculation of fatigue resistance of welded joints and assemblies. This promotes negative results in designing with respect to required life of welded elements. Development of safe and technological welded elements of freight car bogie requires application of the recent achievements in the field of fatigue strength of welded joints. 13 Ref., 4 Tables.

**Keywords:** *welded structures, welded joint, freight car, three-element bogie, side frame, frame failure, fatigue resistance, stress amplitude*

Statistics of accident rate at Ukrainian and Russian railways is an evidence of increase in the recent years of the accidents, related with failure of cast bearing elements of two-axle three-component freight car bogies. Analysis of service reliability of cast structures of side frame and bolster of 18-100 type bogie and its modifications shows that appearance of fatigue cracks is the main reason of reject [1, 2]. Increase of fatigue resistance and survivability of the bogie bearing elements is extremely relevant.

Using of welding technologies for manufacture of indicated parts from sheet products for increase of their service reliability characteristics under alternating loads is promising [3].

Welded structures of the freight car bogies are widely used in Western Europe. The attempts were made in Ukraine and Russia on development of structures of all-welded bearing elements of two-axle three-component freight car bogies, which can replace the cast structures [4–8]. However, any of the developed welded structures of side frames and bolster is not used today in regular tracking industry, since their structures in most cases had insufficient optimizing from point of view of welded joint fatigue resistance.

Safety of welded variant of bearing components should be provided in development of competitive welded structures of the bearing ele-

ments, which can replace the cast elements of 18-100 type bogie, due to increase of resistance and survivability in comparison with the cast structure. Calculation of fatigue resistance of developing all-welded structures of the elements of freight car bogie is regulated using acting Ukrainian and Russian Norms of calculation and design of 1520 mm track railway cars of Ministry of Railways (non-self-propelled) [9] (further the Norms) based on coefficients of margin of fatigue resistance for different zones of evaluation (base metal and welds) considering distribution of coefficient of vertical dynamics in the ranges of service rates (loading spectrum).

Unfortunately, real cyclic load resistance of the welded joints is significantly overstated in acting Norms for designing of welded joints and assemblies of the railway cars, that promotes negative results of designing with respect to required life.

The values of these loads depend on car movement speed, condition of track etc., i.e. there is a whole spectrum of cyclic loads, elements of which have different appearance probability in time of car servicing. This problem is sufficiently well studied and the Norms include the corresponding recommendations, allowing quantity determination of power characteristics of cyclic loading under service conditions. Disadvantage of the Norms is the recommendations with respect to values of cyclic load resistance of bearing welded joints.

**Table 1.**  $(\overline{K}_{\sigma})_{\alpha}$  value for some typical elements of bearing structures of cars in accordance with Norms [9]

Characteristics of element and calculation zone	$(\overline{K}_{\sigma})_{\alpha}$
Standard sample with polished surface on GOST 25.502-79	1.0
Rolling or cast strip with 20 cm <sup>2</sup> section without stress concentrators along base metal	1.3-1.5
Bolsters from structural shapes (flange, channel, zed, angle) and blanked from sheet products along flange base metal (far from stress concentrators)	1.3-1.5
Box bolsters, welded from structural shapes and blanks by butt welds along upper and lower flanges without transverse stiffeners and diaphragms, along weld	1.4-1.6
Box bolsters, welded from structural shapes by fillet welds without transverse stiffeners and diaphragms, along weld	1.5-1.7
Bolsters from structural shapes and blanks, bands of box bolsters from sheet products, welded by double-sided straight transverse butt welds, in weld zone	2.0-2.4
The same, double-sided 45° scarf welds	1.8-2.2
The same, double-sided straight welds, treated flush with base metal surface	1.5-1.7
The same, one-sided straight welds (with lack of root penetration or without root run)	4.0-4.8

Fatigue limit  $\sigma_{a, N}$  (on amplitude) in the Norms, under condition that  $\sigma_{a, N}$  corresponds to non-failure probability  $P = 0.95$ , for welded frames and bolsters from sheet and structural shapes in use of semi-automatic and manual welding, is

$$\sigma_{a, N} = \frac{\overline{\sigma}_{-1}}{(\overline{K}_{\sigma})_{\alpha}} (1 - z_d v_{\sigma}), \quad (1)$$

where  $\overline{\sigma}_{-1}$  is the average (median) value of fatigue limit of smooth standard sample from part material (on GOST 25.502-79) at symmetric cycle of bending ( $R = -1.0$ ) on  $N$  cycle basis;  $(\overline{K}_{\sigma})_{\alpha}$  is the average value of coefficient of reduction of fatigue limit of part in relation to fatigue limit of standard sample;  $z_d$  is the  $\sigma_{a, N}$  reciprocal distribution as random quantity;  $v_{\sigma}$  is the coefficient of variation of fatigue limit under condition that  $\sigma_{a, N}$  corresponds to non-failure probability  $P = 0.95$  ( $(1 - z_d v_{\sigma}) = 0.88$ ).

Data from the Norms [9] on  $(\overline{K}_{\sigma})_{\alpha}$  value for typical elements of car bearing structures are given in Table 1.

It follows from dependence (1) that, since  $\overline{\sigma}_{-1}(N)$  depends on strength of base metal and rise with  $\sigma_t$  growth, then user of the Norms can suppose that increase of structural steel strength  $\sigma_t$  promotes, according to (1), rise of  $\sigma_{a, N}$ . Meanwhile, a well-known fact is clearly indicted in the IIW Recommendations [10] based on processing of number of experimental data. It is a provision that  $\sigma_{a, N}$  value at sufficiently representative sample of tests does not depend on  $\sigma_t$  for untreated welded joints of structural steels of ferrite (pearlite) classes of strength limit  $\sigma_t$  from 400 to 900 MPa. Thus, low-cycle fatigue resistance of the welded joints will be approxi-

mately the same for welded frame and bolster from low-carbon steel, having strength limit  $\sigma_t = 400$  MPa, and from high-strength low-alloy steel with  $\sigma_t = 900$  MPa.

There are also significant remarks in relation to values of  $(\overline{K}_{\sigma})_{\alpha}$  coefficients, recommended for welded joints in the Norms. Thus,  $(\overline{K}_{\sigma})_{\alpha}$  value at 1.5-1.7 level is recommended for longitudinal welded joints of the bolsters, manufactured from sheet products, i.e. for steel with  $\sigma_t = 450$  MPa and  $\overline{\sigma}_{-1} = 225$  MPa on  $10^7$  cycle basis,  $\sigma_{a, N}$  value for welded joints according to (1) equals

$$\sigma_{a, N} = \frac{225}{1.7} \cdot 0.88 = 117 \text{ MPa.}$$

The fatigue limit (on amplitude) on  $2 \cdot 10^7$  cycle basis for the welded joints following the IIW Recommendations [10] is

$$\sigma_{a, N} = 0.5 \text{FAT} f(R) f(N), \quad (2)$$

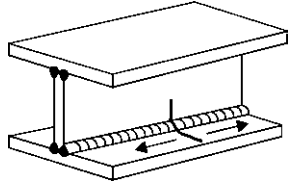




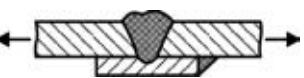
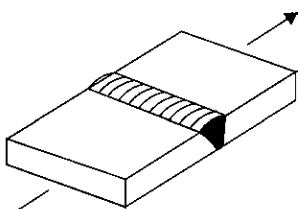
where FAT is the fatigue limit (on range) on  $2 \cdot 10^6$  cycle basis at symmetric cycle, determined by welded joint class (Table 2);  $f(R)$  is the function of coefficient of asymmetric cycle of loading  $R$  and level of residual stresses.  $f(R)$  value at  $R = -1.0$  lies in  $f(R) = 1.6$  level at residual stress less than 0.2, and  $f(R) = 1.0$  at higher residual stresses;  $f(N)$  is the parameter, considering limited fatigue.  $f(N)$  in the range of  $10^4 < N < 10^8$  cycles is determined by dependence

$$f(N) = \left( \frac{C}{N} \right)^{1/m}, \quad (3)$$

where  $N$  is the welded joint life;  $C = 2 \cdot 10^6$ ,  $m = 3$  at  $10^4 < N < 10^7$  cycles. It can be assumed that amplitude is not changed at  $N > 10^7$  cycles.

Thus,  $\sigma_{a, N}$  according to [10] does not exceed 26 MPa for longitudinal welded joints of bolsters

**Table 2.** Fragments of FAT values for different welded joints from IIW Recommendations [10]

Number	Part sketch	Description	FAT (for steel)
300		Fillet (tee) welded joints with longitudinal loading	
321		Longitudinal continuous welds with double-bevel groove, automatic welding without interruptions, non-destructive testing (stresses in the flange)	125
322		Longitudinal continuous welds without double-bevel groove, automatic welding without interruptions, non-destructive testing (stresses in the flange)	100
323		Longitudinal continuous fillet welds, manual welding with double-bevel groove and without it (stresses in the flange)	90
200		Butt joints (transverse loading)	
Double-sided joints			
211		Weld with transverse loading, double-vee groove or single-bevel V-preparation, removed reinforcement. 100 % non-destructive testing	112
212		Transverse weld, flat welding under workshop conditions. Non-destructive testing, weld reinforcement <0.1 of thickness	90
213		Transverse weld, which does not satisfy condition No. 212. Non-destructive testing. <i>Note:</i> weld with angle of reinforcement ≤50°, welds with reinforcement angle >50°	80
One-sided joints			
214		Transverse weld with non-consumable backing, root crack	80
215		Transverse weld on permanent backing, fastened at >10 mm distance from plate end. Same, <10 mm from plate end	71 63
216		Transverse butt welds, one-side welding, without backing, full penetration. Root is controlled by non-destructive methods without non-destructive testing	71 36

at FAT = 90–125 MPa,  $f(R) = 1.0$  and  $f(N) = 0.585$  ( $N = 10^7$  cycles).

Respectively, allowable amplitudes  $[\sigma_{a, N}] = \sigma_{a, N} / n$ , where  $n$  is the coefficient of safety.  $n$  values on the Norms are taken in the ranges 1.3–1.8 for elements of car bodies of all types depending on level of data reliability on  $\sigma_{a, N}$ , and  $n = 2$  is recommended for new structures. Safety coefficient is set in  $n = 1.15$ – $1.40$  ranges for critical structures on IIW Recommendations. The respective allowable amplitudes are received for considered longitudinal welded joints under such an assumption:

$$[\sigma_{a, N}] = 117 / 2 = 58.5 \text{ MPa}$$

$$\text{and } [\sigma_{a, N}] = \frac{26}{1.15-1.40} = 24-19 \text{ MPa.}$$

It can be seen that allowable values of amplitudes of nominal stresses  $[\sigma_{a, N}]$  at regular alter-

nating loading on  $10^7$  cycle basis for longitudinal welded joints of bolsters according to the Norms are 145–210 % higher of that on IIW Recommendations.

Comparison of allowable  $[\sigma_{a, N}]$  values for one- and double-sided butt welds, located transverse with respect to effect of nominal stresses, was carried out similarly to longitudinal welded joints. The results of comparison, presented in Table 3, confirm that real cyclic load resistance of the welded joints is significantly overstated in the acting Norms. Such examples show that life of welded bearing structures of the railway cars, designed in the ranges of the Norms, can be insufficient. Probably, it is one of the reasons why safe and technological structures of the all-welded bearing elements of three-component freight car bogie, capable to compete with the cast parts, have not been developed yet.



**Table 3.** Comparison of allowable values of amplitudes of nominal stresses  $[\sigma_{a, N}]$  at regular alternating loading on  $10^7$  cycle basis for different welded joints by the Norms [9] and DBN [11] as well as IIW Recommendations for structures from steel with tensile strength  $\sigma_t = 450$  MPa

Type of welded joint	Norms [9] (at $n = 2$ )		IIW Recommendations [10]			DBN [11] (at $n = 2$ )
	$(\overline{K}_\sigma)_a$	$[\sigma_{a, N}]$ , MPa	FAT, MPa	$n$	$[\sigma_{a, N}]$ , MPa	$[\sigma_{a, N}]$ , MPa
Longitudinal fillet	1.5–1.7	58–66	90–125	1.15 1.40	26–32 19–23	23
Transverse double-sided butt	2.0–2.4	41–50	80–112	1.15 1.40	23–28 15–20	33
Transverse one-sided butt	4.0–4.8	21–35	36–80	1.15 1.40	17–20 7.5–9.0	16

Positive experience of application of IIW Recommendations in development of welded structures of freight car bogies should be noted. In 2002 GSKBV Ltd. (Mariupol, Ukraine) together with SUE «Vagony» (St.-Petersburg, RF) developed a new welded structure of three-element bogie of 18-1711 model with 25 tf axis loading [12]. Primary pilot samples of the bolsters did not pass bench fatigue tests. Thus, all-welded structure of the bolster was improved by the PWI specialists from point of view of increase of fatigue resistance of its welded joints [13]. Further, short-cut accelerated cyclic load tests were carried out for two pilot samples of the bolster. As a result, 30 mm length macrocrack was found in the first bolster at  $2.745 \cdot 10^6$  cycles, and no macrocrack was found after  $6 \cdot 10^6$  cycles of loading in the second bolster, and the tests were stopped. Thus, carried tests showed that developed welded structure of the bolster provides for necessary life and it is inferior to cast one on strength and weight indices and can be recommended for performance of full cycle of tests.

One of the documents acting in Ukraine and regulating calculation of fatigue resistance of ele-

ments of steel structures, including welded ones, is the State building standards (DBN) [11]. According to this document, boundary allowable quantity of cycles  $N_i$  in calculation of total failure rate of the steel structures is calculated in the following way:

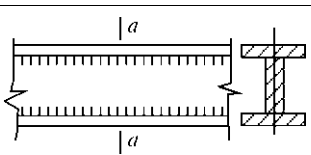
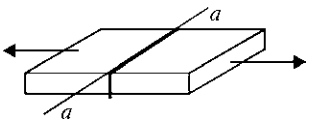
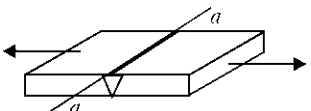
$$N_i = \frac{A_p \cdot 10^3}{\ln \left[ \frac{2\sigma_{a, i}}{(1 - \rho_i)R_{\rho i}} \right]} - B_p \cdot 10^3, \quad (4)$$

where  $\sigma_{a, i}$  is the amplitude stresses of cycle;  $\rho$  is the cycle asymmetry;  $R_{\rho i}$  is the calculation fatigue limit of section being calculated, determined on formulae

$$R_\rho = \frac{2\sigma_{-1}}{2 - D_n(1 + \rho)} \left( 1 - 1.63 \frac{S_{\sigma_{-1}}}{\sigma_{-1}} \right), \quad (5)$$

where values of parameters  $\sigma_{-1}$ ,  $D_n$ ,  $S_{\sigma_{-1}}$  are taken from Tables of [11];  $A_p$  and  $B_p$  are the parameters, which are set in Tables of [11]. At that, base metal, welded joints, high-strength bolted joints of elements and assemblies of the structures are divided on groups considering effect of forces

**Table 4.** Some groups of elements and joints during fatigue calculation [11]

Scheme of element and position of section being calculated	Element characteristics	Group of element
	Sections of double-tee, tee and other types, welded by continuous longitudinal band welds at force application along weld axis	3a and 3b
	Butt untreated weld at loading applied normal to weld line, at that joined elements have similar width and thickness	2
	Butt weld, produced on backing sheet, at loading applied normal to weld line	4a and 4b

with respect to calculation section and following the structural-technological characteristics. Table 4 shows groups of elements of different joints [11].

Thus, according to [11] the fatigue limit on  $10^7$  cycle basis will equal 42 MPa for longitudinal fillet welded joints of bolsters in cycle asymmetry  $\rho = -1$  and  $\sigma_{-1} = 62$  MPa,  $S_{\sigma_{-1}} = 12$  MPa and  $D_n = 0.89$  coefficients from expression (5).

Allowable amplitudes of nominal stresses  $[\sigma_{a, N}]$  equal an amplitude of cycle stresses  $\sigma_{a, i}$  at regular alternating loading on  $10^7$  cycle basis and  $\rho = -1$ , and can be determined from dependence (4)

$$\sigma_{a, i} = \exp \left( \frac{A_p \cdot 10^3}{10^7 + B_p \cdot 10^3} \right) \frac{(1 - \rho_i) R_p}{2} =$$

$$\exp \left( \frac{525 \cdot 10^3}{10^7 + 470 \cdot 10^3} \right) \frac{(1 + 1) \cdot 42}{2} = 45 \text{ (MPa)}.$$

In order to obtain more specific calculation of the allowable amplitudes of nominal stresses for side frames and bolsters of railway bogies based on DBN [11], the values received on formulae (4), for such critical structures, should be divided on safety coefficient  $n = 2$ . Table 3 includes the values of the allowable amplitudes of nominal stresses  $[\sigma_{a, N}]$  according to [11] for different welded joints without heat treatment in comparison with data from the acting Norms and IIW Recommendations. It can be seen that calculation of fatigue resistance of the welded joints based on DBN [11] provides for more conservative results in comparison with the Norms [9], which significantly overstate real cyclic load resistance of the welded joints that can result in errors in designing of new welded structures of bearing elements of the freight car bogies.

## Conclusions

1. Development of all-welded structures of bearing elements of the freight car bogie, which may replace cast elements of 18-100 type bogie, can provide for increase of their reliability and life, reduction of weight and accuracy of coordinating dimension of side frame in the ranges of one dimension type. Implementation of production of the bogie elements using welding technology is not so cost consuming in comparison with casting

technology that can create conditions for market saturation with quality elements of the freight bogie.

2. Welded structures of bearing elements of the railway freight car bogies, designed in scope of the acting Norms, can have insufficient life, which is conformed by practice.

3. Designing of safe and technological welded elements of the freight car bogie requires application of the recent developments in area of welded joint fatigue strength. The acting Norms of calculation and designing of railway cars, in particular for the welded joints of these structures, demand thoroughgoing working up, considering information of the International Institute of Welding (IIW Recommendations).

1. Pranov, V.A. (2012) *Increase of fatigue life of side frame of freight car bogie*: Syn. of Thesis for Cand. of Techn. Sci. Degree. Ekaterinburg: UralGURS.
2. Sokolov, A.M. (2012) About formation of complex program of research on problem of side frame fractures of freight car bogies. *Byull. Obied. Uch. Soveta OAO RZhd*, **3**, 3–11.
3. Makhnenko, O.V., Saprykina, G.Yu., Mirzov, I.V. et al. (2014) Prospects for development of load-carrying elements of freight car bogie. *The Paton Welding J.*, **3**, 33–38.
4. Volkov, V.A., Chepurnoj, A.D., Bubnov, V.M. et al. *Two-axle bogie for freight cars*. Pat. 2275308 RU. Publ. 27.04.2004.
5. Khominich, V.S., Trojnikov, M.A., Bogdanov, V.P. *Side frame of freight car bogie*. Cert. on utility model 37683 U1 RU. Publ. 10.05.2004.
6. Dejneko, S.Yu., Prikhodko, V.I., Bondar, N.A. et al. *Two-axle bogie of freight car*. Pat. 2246416 C2 RU. Int. Cl. K7 B61F5. Publ. 20.06.2004.
7. <http://www.nvc-vagon.ru>
8. Sharapov, A.A., Goloviznin, B.L., Malykh, N.A. et al. *Freight car bogie, side frame and bolster of freight car bogie*. Pat. 2373091 C2 RU. Int. Cl. K7 B61F5. Fil. 04.10.2007. Publ. 20.11.2009.
9. (1995) *Norms of calculation and design of 1520 mm track railway cars of Ministry of Railways (non-self-propelled)*. Moscow: GosNIIV-VNIIZhT.
10. (2006) Recommendations for fatigue design of welded joints and components. *IIW Doc. XIII-1965r14-03/XV-1127r14-03*.
11. (2011) *DBN V.2.6-163:2010: Structures of constructions and buildings. Steel structures. Standards of design, production and assembly*. Kyiv: Minregionbud of Ukraine.
12. Volkov, V.A., Chepurnoj, A.D., Bubnov, V.M. et al. *Two-axle bogie for freight cars*. Pat. 2275308 RU. Int. Cl. K7 B61F5/38; B61F5/26; B61F5/12; B61F3/02. Publ. 27.04.2004.
13. Makhnenko, V.I., Garf, E.F., Rimsky, S.T. et al. (2006) Welded freight bogie bolster project. *The Paton Welding J.*, **4**, 2–8.

Received 02.06.2014

# ESTIMATION OF POSSIBILITY FOR PRODUCING FULL-STRENGTH JOINT OF LARGE STEEL PARTS USING THE METHOD OF AUTOVACUUM BRAZING OF THREADED PROFILE

M.A. POLESHCHUK, M.G. ATROSHENKO, A.L. PUZRIN and V.L. SHEVTSOV

E.O. Paton Electric Welding Institute, NASU

11 Bozhenko Str., 03680, Kiev, Ukraine. E-mail: office@paton.kiev.ua

Mechanical properties of brazed threaded joints from similar and dissimilar steels produced by autovacuum brazing method are studied in thread transverse direction. It is determined that tearing strength limit in brazing of low-alloy structural steels corresponds to yield strength of steel after traditional heat treatment. The tearing strength of brazed threaded joints of 12Kh18N10T to 40Kh steels significantly exceeds the yield strength of stainless steel. Permanent joints, produced by means of thread with further autovacuum brazing, can be recommended for manufacture of parts of critical designation. 11 Ref., 1 Table, 3 Figures.

**Keywords:** *autovacuum brazing, threaded joints, dissimilar steels, mechanical properties*

Today special brazing methods allow producing brazed seams with strength equal or close to strength of parts to be joined from different steel grades. Such result is achieved at minimum possible width of the brazed seam using brazing filler alloys (BFA) with high melting temperature, since refractory BFA have larger elasticity modulus and provides higher strength to the brazed joint [1, 2].

A technology of receiving of full-strength brazed seams can be used for production of permanent threaded joints in large-sized parts, which should maintain large forces, caused by loads or pressure. In this case required strength of the part along the longitudinal axis is provided by selection of thread of corresponding profile, and that across the axis is determined by brazed joint strength. Such joints can be used for manufacture of the profile parts, including from dissimilar steels, in performance of load bearing seams of rings, forming thick-wall vessels, sections of thick-wall pipelines of power installation instead of electroslag or multi-pass arc welding [3].

The brazed threaded joints are used in different branches, for example, aircraft building, oil and gas industry etc. However, earlier applied methods of brazing allow penetration of BFA in the threaded joint only at depth of several turns. In this connection brazing of the threaded joints is carried out only for their sealing [4–6].

A method of autovacuum brazing (AVB) allows increasing the depth of BFA flowing in narrow capillary gap. This method provides for the possibility of joining of metals, including dissimilar ones, by means of filling of pressure seal

gap between the parts by BFA. Heating of steel parts to more than 1000 °C promotes for spontaneous cleaning of metallic surfaces, transformed into the pressure seal gap, from oxide films due to diffusion of oxygen from the surface to metal depth [7]. This process takes place up to the moment when all oxygen, present in the pressure seal gap, diffuses in a metal volume. At that, vacuum is formed in the gap. Spontaneous cleaning from the oxide films and absence of noticeable evaporation of BFA components in pressurized volume promotes for increase of the depth of its penetration into the gap [8].

The aim of present work is an estimation of fundamental possibility for production of the AV-brazed threaded joints. Capability of the BFA to penetration at significant depth in the threaded joint was determined at the first stage, and mechanical properties of the brazed joints, including strength in thread transverse direction, was checked at the second one.

Copper was taken as a BFA for performance of work. It is the most widespread BFA for brazing of carbon and low-alloy steels. Brazing temperature made 1150 °C.

The BFA melting temperature in order to provide high strength of the whole part should be higher than the temperature of quenching of steels used for manufacture of threaded joint, as long as heat treatment of finished part should be preceded by brazing.

It is a well-known fact that heating of steel in brazing to the temperature significantly higher than quenching one results in grain growth and loss of its ductility and toughness. Special investigations showed that further quenching with tempering of the steel parts, brazed at more than

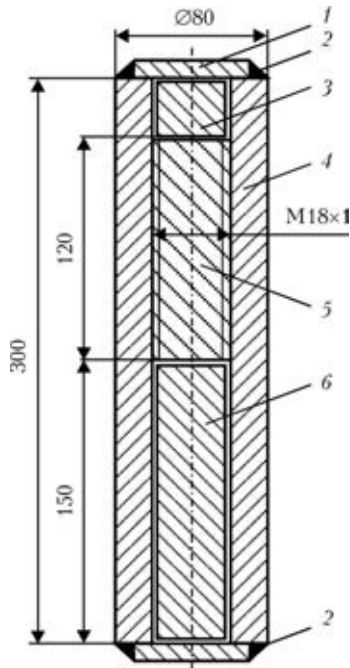


**Figure 1.** Scheme of sample for AVB in assembly: 1 – technological flange; 2 – seal seams; 3 – BFA; 4 – body; 5 – rod with thread; 6 – smooth rod

1000 °C, provides for complete reconstruction of metal strength properties as well as rises indices of ductility and toughness in comparison with the same indices of metal, which was not previously subjected to high temperature heating [9].

Special samples of two types were manufactured for experiment performance. One sample included a threaded joint, produced from one grade of steels (40Kh), and another from different steel classes (40Kh and 12Kh18N10T). Bodies of experimental samples were manufactured from round rolled metal of 80 mm diameter and 300 mm length. Through-holes of 18 mm diame-

ter were made in them. Thread M18×1 was screwed in the middle of length of these holes and the second part remained smooth.

Experimental bodies were produced from steel 40Kh, which after standard heat treatment (quenching in oil with further tempering) provides for mechanical properties of metal for wide range of forgings at the level of requirements of strength category SC-490 [10], in particular for manufacture of parts of critical designation.

Two rods were manufactured for each body. One with M18×1 thread and another with smooth surface, at that the gap between it and body made 0.02 mm per side.

One set of the rods was manufactured from 40Kh steel bar of 20 mm diameter and another was made from stainless steel 12Kh18N10T of the same diameter. M1 copper rod of 15 mm diameter and 30 mm length was used as a BFA.

All parts before assembly for brazing were thoroughly washed from emulsion, which was used for machining of the parts. The gaps from both sides were sealed using electric arc welding after assembly of the samples for brazing (Figure 1).

Brazing was carried out in furnace with air atmosphere, the bodies in the furnace were installed vertically, BFA upward.

Brazing thermal cycle was the following: heating to 1150 °C, 1 h holding, cooling at furnace to room temperature. The bodies after brazing were subjected to quenching with tempering using the mode standard for steel 40Kh. Then, the templates of 14 mm thickness were cut out in the body center along the longitudinal axis.

Visual inspection of these polished templates showed that copper BFA penetrates not only through the thread, but at the whole length of smooth brazing gap in similar sample with rod from 40Kh steel. No incomplete penetration was found (Figure 2) using lens at ten-fold magnification.

At the same time, the BFA filled the gap only partially in combined sample, and did not penetrate in the smooth gap at all. The reason of this can be a difference in heat expansion of structural and stainless steels. Thus, the difference in heat expansion at 20 mm length for such steels makes 0.14 mm and virtual gap before heating in smooth samples is 0.04 mm. However, it can not be a

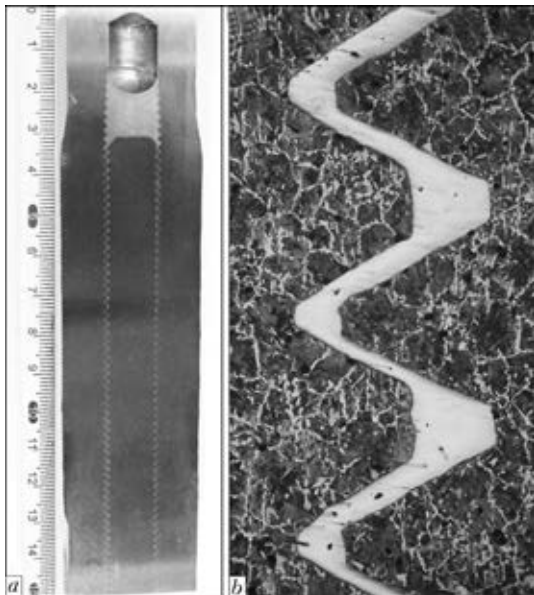


**Figure 2.** Macrosection of template (a) and microsection of threaded part of brazed 40Kh sample (b)

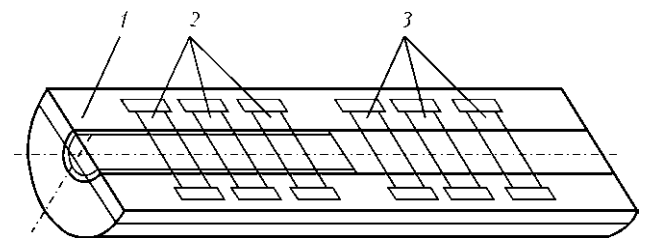


**Figure 3.** Scheme of cutting out of samples for mechanical tests: 1 – template; 2, 3 – samples with and without thread, respectively

Results of mechanical tests of base metal after heating for brazing and further heat treatment

Place of sample cutting out	Yield strength, MPa	Tensile strength, MPa	Elongation, %	Reduction in area, %
Steel 40Kh body	$\frac{540.9-581.8}{561.4}$	$\frac{771.8-778.4}{775.1}$	$\frac{17.5-19.1}{18.3}$	$\frac{62.4-65.4}{63.9}$
Steel 40Kh rod	$\frac{552.6-561.4}{557.0}$	$\frac{742.2-763.1}{752.7}$	$\frac{16.2-18.2}{17.2}$	$\frac{60.3-61.2}{60.8}$
Steel 12Kh18N10T rod	$\frac{207.7-215.0}{211.4}$	$\frac{555}{555}$	$\frac{61.3-61.7}{61.5}$	$\frac{69.5-69.8}{69.7}$

Notes. 1. Minimum and maximum values are given in numerator, average value on three samples – in denominator. 2. Requirement GOST to SC  $\geq 490$ .

single reason of absence of brazed joint formation, since copper is successfully used even for brazing of the parts from carbon steels, preliminary assembled by press fit [11].

The reason also preventing penetration of copper in the narrow gap of combined sample can be dissolving in it of the alloying components of stainless steel, first of all of chromium and nickel, that increases temperature of melting of alloyed copper to the brazing temperature.

The samples for mechanical tests of brazed joints were manufactured from the billets cut out across the longitudinal templates (Figure 3).

The tests were carried out by means of tension of the samples with 8 mm diameter test portion. At that, it included two brazed joint each, located at 18 mm distance from each other. Tensile tests promoted fracture along one joint.

Thus, tearing strength made 485.0–500.1 for 40Kh brazed joint with smooth surface, and that was 412.6–458.4 MPa for joint with thread. The samples from dissimilar steels 40Kh + 12Kh18N10T with thread had 294.7–323.7 MPa.

Visual examination of the samples after testing showed that the brazed joint failures across the longitudinal axis without plastic strain. Since a calculation value for estimation of part strength is taken as a value of yield strength of the material, from which given part is manufactured, then the results given above should be compared with the base metal yield strength. The results of mechanical tension tests of the samples from base 40Kh and 12Kh18N10T metals are presented in the Table.

Comparison of the results of tearing strength of the brazed joints with yield strength of the base metal showed that tearing strength of the brazed joint of steel 40Kh to the same steel with smooth surfaces makes 485–500 MPa. This corresponds to the requirements of standard for SC-490, but somewhat lower the yield strength of real samples of steel 40Kh after heat treatment (540–580 MPa), received in rolling direction. This well-known fact that properties of rolled metal in transverse direction will be lower. Therefore, obtained results of mechanical tearing tests of the smooth samples can be taken as good.

Tearing strength of the brazed joint with thread from similar steel (40Kh) in direction across its axis was somewhat lower (413–458 MPa). Lower value of tearing strength across the threaded joint in comparison with the smooth one can be explained by larger width of the gap between parts of the thread.

Joint strength (295–308 MPa) was noticeably higher the stainless steel yield strength (208–215 MPa) in testing of the brazed samples of 12Kh18N10T to 40Kh steels with thread.

Therefore, permanent joints, produced with the help of thread and further AVB, can be used for manufacture of parts of critical designation. Copper as a BFA can be efficiently used for production of such type of the joints from structural steels, and only for the threaded joints of relatively small depth in the case of combined ones (stainless–structural steels).

1. Khorunov, V.F. (2008) *Principles of brazing of thin-wall structures of high alloy steels*. Kiev: Naukova Dumka.
2. (1975) *Reference book on brazing*. Ed. by S.N. Lotsmonov. Moscow: Mashinostroenie.
3. Serebryanik, I.P. (2011) *Autovacuum noncapillary structural brazing*. Kiev: Alfa Reklama.
4. Kuznetsov, V.A. (2004) Determination of pressure gas value in brazing with reinforced gap filling by molten brazing filler alloy. In: *Proc. of Seminar on State-of-the-Art and Prospects of Development of Brazing*. Moscow: Znania.
5. Karabanov, V.V., Bokharov, I.O. (2012) Solution of problems of leakproofness and reliability of casing pipes. *Neft. Khozyajstvo*, 1, 42–45.
6. Muraviov, V.I., Mariin, B.N., Chernyshov, L.V. *Method of brazing of thin-wall pipes in telescopic joining*. Pat. 2193477 RF. Int. Cl. 23K 1/00. Publ. 27.11.2002.
7. Paton, B.E., Medovar, B.I., Puzrin, L.G. et al. (1968) About solution of air gases in solid metal during spontaneous cleaning of its surface. *Doklady AN SSSR*, 181(1), 70.
8. Puzrin, L.G., Bojko, G.A., Atroshenko, M.G. (1975) *Autovacuum brazing*. Kiev: Znania.
9. Grigorenko, G.M., Puzrin, A.L., Atroshenko, M.G. et al. (2012) Influence of high-temperature heating on properties of steels in brazing of composite bodies of high pressure blind flange. *Sovr. Elektrometallurgiya*, 2, 45–50.
10. *GOST 8 479–70: Forged pieces of structural carbon and alloy steel*. Introd. 01.01.71.
11. Brooker, H.R., Beatson, E.V. (1957) *Industrial brazing*. Moscow: Oborongiz.

Received 02.04.2014

# BRAZE-WELDED TUBULAR BILLETS FOR PIPELINES AND HIGH-PRESSURE VESSELS\*

A.A. PISMENNY, R.S. GUBATYUK, A.S. PROKOFIEV, A.F. MUZHICHENKO and A.S. SHINKARENKO

E.O. Paton Electric Welding Institute, NASU  
11 Bozhenko Str., 03680, Kiev, Ukraine. E-mail: office@paton.kiev.ua

Application of two-layer shells for formation of common wall is supposed to be prospective for reduction of weight of pipeline structures as well as pressure vessels. Calculation of three single-type pressure vessel structures, having common wall, which is made as two-layer shell, was carried out. At that, analysis was given for applied materials and their combination used for manufacture of internal and external shells of common two-layer wall of three types of pressure vessels considering their strength indices. It is determined that application of the same steel grade in two-layer structure does not result in efficient loading of common wall. Application of material with higher strength characteristics for manufacture of external shell results in efficient loading of their common wall, reduction of its thickness and growth of its internal stresses, i.e. reasonable loading. Considered are the issues of application of mesh-like material for manufacture of external shell as well as usage of high-frequency pressure braze-welding in production of perspective tubular billets, designed for pipelines and high-pressure vessels. Ref. 12, Tables 7, Figures 8.

**Keywords:** *pressure braze-welding, tubular billet, thin-wall shell, stresses, simulation model*

Pressure vessel bodies have, as a rule, cylindrical form. Pipes of corresponding dimension-types are used in their manufacture or the bodies are manufactured from tubular billets, including thin-wall ones, designed for production of longitudinal or spiral pipes with continuous weld. The spiral pipes have series of advantages. Since a weld is produced at angle to cylinder axis, its partial unloading from radial stresses, appearing in a wall of pressure vessel body, is provided [1].

Relevant operation of pressure vessel can be achieved in providing of uniform distribution of stresses in its wall. At that, stresses formed in cylindrical wall of the body should not exceed allowable values for material, used in manufacture of the vessel. Obviously, that application of materials with increased strength properties results in reduction of thickness of cylindrical wall of the pressure vessel as well as weight of such commercial products.

Relevant application of material and reduction of thickness of wall of the vessel cylindrical bodies is also possible, if they are produced compound, for example, the body wall is made from two-shells or more. It is a well-known fact that two co-axial shells, fit on with tension, provide more relevant distribution of stresses formed in their common wall [2].

Stresses, appearing as a result of effect of internal pressure in cylindrical wall of vessel body and acting in radial and axial direction, are not uniform. It was determined [2, 3] that the stresses in radial direction 2 times exceed the stresses acting in axial direction. These peculiarities should be taken in account in selection in structural material with corresponding strength characteristics and wall thickness.

There is an experience of manufacture [4, 5] of metal-composite vessels for compressed gases, structure of body of which is in fact two-shell. At that, external load-bearing shell is produced from composite material, namely synthetic hard-rail or roving, coiled over internal shell under tension.

Backgrounds of application of high-frequency braze-welding technology in manufacture of proposed prospective, from our point of view, structure of pressure vessels, are considered in present paper. At that, it is assumed to ensure relevant distribution of stresses in the vessel walls, improvement of its weight and strength indices as well as technological advantages in manufacture. Calculation-experimental model of the vessel was used. Such a model structure can be balloon model, cylindrical part of which is produced in form of two coaxial shells, fit on with tension. At that, internal cylindrical shell can have a sealing function, provide resistance in contact with operating medium as well as have good weldabil-

\*The work was carried out under the leadership of Profs A.S. Pismenny and O.V. Makhnenko.

ity with bottom parts of the balloon for obtaining of sound, seal and corrosion-resistant welds.

External shell of cylindrical part of the body can be manufactured from material with strength indices higher in comparison with that of internal shell.

Such two-shell cylindrical part of the body should have a series of advantages, namely provide more relevant distribution of stresses forming in their common wall, as well as reduce total weight of the whole balloon due to reduction of thickness of wall of the external shell in the case of its manufacture from higher-strength material.

The work considers three single-type structures of samples of the pressure vessels (balloons), wall of cylindrical body of which represents itself two-layer shell. The internal thin-walled (relation of diameter to wall thickness is 10 and more) shell of cylindrical body has similar geometry in all model structures. The external shell in calculation models is fitted on the internal shell with minimum tension, close to zero, at that its internal diameter matches with external diameter of the internal shell, and its external diameter is calculated for each applied material.

Determined are the stresses forming in external and internal shells as well as total stresses in common wall of the two-shell balloon. The following conditions were maintained at that:

- calculations were carried out taking into account the same internal operation pressure for all three types of balloons ( $p_{op. work} = 20$  MPa) and the same geometry of wall of the internal shell ( $d_{in 1} = 147.5$  mm;  $d_{ex 1} = 152$  mm), wall thickness of the internal shell is constant ( $S_1 = 2.25$  mm) for all three types of balloons;
- internal diameter of the external shell corresponds to external diameter of wall of the internal shell and is constant ( $d_{ex 1} = d_{in 2} = 152$  mm) for all three types of balloons;
- dimensions of wall of the external shell ( $d_{ex 2}, S_2$ ) were calculated based on stresses forming in the external shell and strength indices of used steel grade;
- the minimum value from calculation thicknesses of common balloon wall  $S_{bal}$  was used in the balloon structure;
- stresses in the separate shells as well as total stresses in the common vessel wall were determined without tension consideration;
- the calculation was carried out in accordance with acting reference documents and provisions of work [6], at that operating working pressure of balloon model was calculated based on coefficient of safety  $n = 2.7$ , on maximum allowable values of stresses forming in metal  $[\sigma]_{work} =$

$= \sigma_0/n$ , where  $\sigma_0$  is the critical dangerous strength. Depending on steel grade  $\sigma_0 = \sigma_y$  for soft materials and  $\sigma_0 = \sigma_t$  for brittle materials.

Combination of different steel grades for internal and external shells was used for optimizing of the model structure. Strength indices of steel grades used for each shell were respectively laid in the calculation models (three single-type structures of two-shell balloons).

Strength of the bottom parts was not calculated, however, thickness of bottom wall for given structure according to metal technical properties can not be lower than the thickness of body wall of the whole balloon [6].

Weld strength in the calculation models was taken equal the base metal strength. The weld strength for given mathematical calculation model, considering application of different material grades, is provided by means of rise of total thickness of wall of the cylindrical body by value of wall thickness increase, which in all cases should be more than 0.5 mm [6].

Technological peculiarities of production of longitudinal, spiral and circumferential welds were not considered in the calculation models in present work. Effect of stresses formed in internal and external shells as well as technological factors (different grades of materials and other factors) was taken into account based on the results of carried calculations in designing of real models of tubular billet structures and samples of pressure vessels.

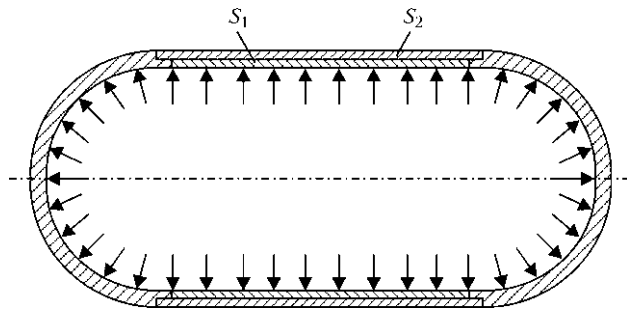
Figure 1 shows a sketch of structure of two-layer balloon, consisting of internal  $S_1$  and external  $S_2$  shells, and Table 1 gives the combinations of materials and relation of thicknesses of shells wall for the calculation models.

Table 2 shows the results of calculation of single-type structures of balloon samples 1–3.

Working stresses, forming in metal of internal  $\sigma_{work 1}$ , external  $\sigma_{work 2}$  and common wall of the balloon  $\sigma_{work bal}$  at operating working pressure applied to the balloon  $p_{op. work} = 20$  MPa, were determined for each sample.

Table 3 gives calculation values of forming working stresses  $\sigma_{work}$ , stresses in internal and external shells, and common wall of the balloon for each sample, from operating working pressure  $p_{op. work}$  applied to the balloon.

Values of maximum allowable working pressures forming in internal  $p_{allow 1}$  and external  $p_{allow 2}$  shells, as well as  $p_{allow bal}$  in common wall of balloon were calculated based on allowable values of stresses forming in metal (taking into account steel grade), determined as  $[\sigma]_{allow} =$



**Figure 1.** Sketch of two-layer balloon (for designations see the text)

= 0 / n, and their percent relationship (Tables 4 and 5) was determined.

Thus, approximately similar pressures are to be applied to the balloon of each sample in order to achieve allowable stresses in metal of the wall

**Table 1.** Combination of materials and relation of thicknesses of shell walls in three models

Number of sample (model)	S <sub>1</sub> + S <sub>2</sub> combination of steels	S <sub>1</sub> /S <sub>2</sub> , mm
1	St.08.kp + high-strength steel	2.25 / 4.11
2	20 + 20	2.25 / 13.29
3	St.08kp + St.08.kp	2.25 / 20.54

of each shell. Their values multiply exceed a nominal internal operating pressure.

The results of calculation show that allowable pressure in the balloon of each sample equals the sum of allowable pressures of internal and external shells. At that, the sum of allowable pressures

**Table 2.** Calculation values of thickness of external shell wall and common balloon wall

Parameter	Sample 1	Sample 2	Sample 3
Allowable stresses in wall metal, MPa:			
internal shell [σ <sub>1</sub> ]	74.0	114.3	74.0
external shell [σ <sub>2</sub> ]	370.4	114.3	74.0
Thickness of wall of internal shell S <sub>1</sub> , mm	2.25	2.25	2.25
Diameter, mm:			
internal shell d <sub>in 1</sub>	147.5	147.5	147.5
average d <sub>av 1</sub>	149.75	149.75	149.75
external d <sub>ex 1</sub>	152	152	152
Thickness of external shell wall S <sub>2</sub> , mm	4.11	13.29	20.54
Diameter, mm:			
internal shell d <sub>in 1</sub>	152	152	152
average d <sub>av 1</sub>	156.11	165.29	172.54
external d <sub>ex 1</sub>	160.22	178.58	193.08
Thickness of balloon common wall S <sub>bal</sub> = S <sub>1</sub> + S <sub>2</sub> , mm	6.36	15.54	22.79
Balloon diameter, mm:			
internal d <sub>in 1</sub>	147.5	147.5	147.5
average d <sub>av 1</sub>	153.86	163.04	170.29
external d <sub>ex 1</sub>	160.22	178.58	193.08
d <sub>ex bal</sub> /S <sub>bal</sub>	160.22/6.36 = 25.19	178.58/15.54 = 11.49	193.08/22.79 = 8.472
S <sub>2</sub> /S <sub>1</sub>	1.83	5.91	9.1

**Table 3.** Comparison of calculation stresses formed in metal of internal σ<sub>work 1</sub>, external σ<sub>work 2</sub> shell walls and common balloon wall σ<sub>work bal</sub> with allowable stresses [σ] from applied to the balloon working pressure p<sub>op, work</sub> = 20 MPa

Parameter	Sample 1	Sample 2	Sample 3
Allowable stresses [σ <sub>1</sub> ], [σ <sub>2</sub> ], MPa	[σ <sub>1</sub> ] = 74; [σ <sub>2</sub> ] = 370.4	[σ <sub>1</sub> ] = 114.3; [σ <sub>2</sub> ] = 114.3	[σ <sub>1</sub> ] = 74; [σ <sub>2</sub> ] = 74
Calculation stresses, MPa:			
internal shell σ <sub>work 1</sub>	6.7	6.7	6.7
external shell σ <sub>work 2</sub>	3.8	1.2	0.84
in common balloon wall, MPa:	2.4 < 5.2	1.049 < 3.95	0.747 < 3.77
σ <sub>work bal</sub> < $\frac{\sigma_{work 1} + \sigma_{work 2}}{2}$			



**Table 4.** Values of allowable stresses in metal of external  $[\sigma_1]$  and internal  $[\sigma_2]$  shells and common balloon wall  $[\sigma_{\text{allow bal}}]$ , MPa

Parameter	Sample 1	Sample 2	Sample 3
Allowable stresses, MPa:			
wall of internal shell $[\sigma_1]$	74	114.3	74
wall of external wall $[\sigma_2]$	370.4	114.3	74
Comparison of forming calculation stresses $[\sigma_{\text{allow bal}}]$ in balloon wall, MPa	$[\sigma_{\text{allow bal}}] > \frac{[\sigma_1] + [\sigma_2]}{2}$ 262.8 > 222.2	$[\sigma_{\text{allow bal}}] = \frac{[\sigma_1] + [\sigma_2]}{2}$ 114.3 = 114.3	$[\sigma_{\text{allow bal}}] = \frac{[\sigma_1] + [\sigma_2]}{2}$ 74 = 74

**Table 5.** Calculation values of forming allowable pressure  $p_{\text{allow}}$  inside shells and balloon, their comparison with operating working pressure  $p_{\text{op. work}} = 20$  MPa after achievement of allowable stresses  $[\sigma]$  by metal

Parameter	Sample 1	Sample 2	Sample 3
Allowable pressures, MPa:			
internal pressure $p_{\text{allow } 1}$	222.37 (10.23 %)	343.56 (15.76 %)	222.37 (11.23 %)
external shell $p_{\text{allow } 2}$	1950.4 (89.77 %)	1838.52 (84.24 %)	1761.9 (88.94 %)
common balloon wall $p_{\text{allow bal}}$	2172.7 (100 %)	2179.45 (100 %)	1980.7 (100 %)
$p_{\text{allow } 1} / p_{\text{op. work}}$	11.12	17.178	11.12
$p_{\text{allow } 2} / p_{\text{op. work}}$	97.52	91.92	88.1
$p_{\text{allow bal}} / p_{\text{op. work}}$	108.63	108.97	99.035

in samples 1 and 2 is virtually the same, and reduction of total allowable pressure for sample 3 is caused by the fact that it is referred to the category of thick-wall balloons (relation of external diameter to wall thickness in sample 3 is determined as  $d_{\text{ex bal}} / S_{\text{bal}} = 193.08 / 22.79 = 8.472 < 10$  (see Table 2)), that requires additional correction of carried calculations. Figure 2 is made based on the results of Table 5.

Values of limiting pressures forming in internal  $p_{\text{lim } 1}$  and external  $p_{\text{lim } 2}$  shells, respectively, and in common wall of the balloon  $p_{\text{lim bal}}$  were calculated, considering material grade and stresses forming in metal  $\sigma_0$ , determined as limiting values, and their percent relation was found (Tables 6 and 7).

At that, metal of internal, external shells and common wall of the balloon achieves the values of (dangerous) stresses  $\sigma_0$ . Figure 3 is made based on the results of Table 7.

Application of the shell, which represent itself sheet material with mesh-like structure of specific thickness, in nodes of which three or more rods intersect, is supposed to be perspective for external shell in the two-layer balloon structure. At that, the stresses are distributed in a formed welded joint in area between internal and external shells as well as in rods of the external shell.

There are nonsolid sheet materials – drawn-punched mesh of different types (TU 14-4-1789–96) as well as mesh hose (TU 26-02-354–85). Production of two-layer structural sheet material

**Table 6.** Values of dangerous stresses in metal of internal  $\sigma_{01}$ , external  $\sigma_{02}$  shells and common balloon wall  $\sigma_{0 \text{ bal}}$ , MPa

Parameter	Sample 1	Sample 2	Sample 3
Internal shell $\sigma_{01}$	200	308.7	200
External shell $\sigma_{02}$	1000	308.7	200
Comparison of calculation forming limiting stresses in common balloon wall $\sigma_{0 \text{ bal}}$ , MPa	$\sigma_{0 \text{ bal}} > \frac{\sigma_{01} + \sigma_{02}}{2}$ 709.6 > 600	$\sigma_{0 \text{ bal}} = \frac{\sigma_{01} + \sigma_{02}}{2}$ 308.6 = 308.7	$\sigma_{0 \text{ bal}} = \frac{\sigma_{01} + \sigma_{02}}{2}$ 199.99 = 200

**Table 7.** Calculation values of forming limiting pressures  $p_{\text{lim}}$  inside the balloon, MPa

Parameter	Sample 1	Sample 2	Sample 3
Internal shell $p_{\text{lim } 1}$	601 (10.24 %)	927.6 (15.763 %)	601 (11.23 %)
External shell $p_{\text{lim } 2}$	5265.5 (89.75 %)	4964 (84.378 %)	4761.4 (88.94 %)
Total balloon wall $p_{\text{lim bal}}$	5866.5 (100 %)	5884.68 (100 %)	5353.2 (100 %)

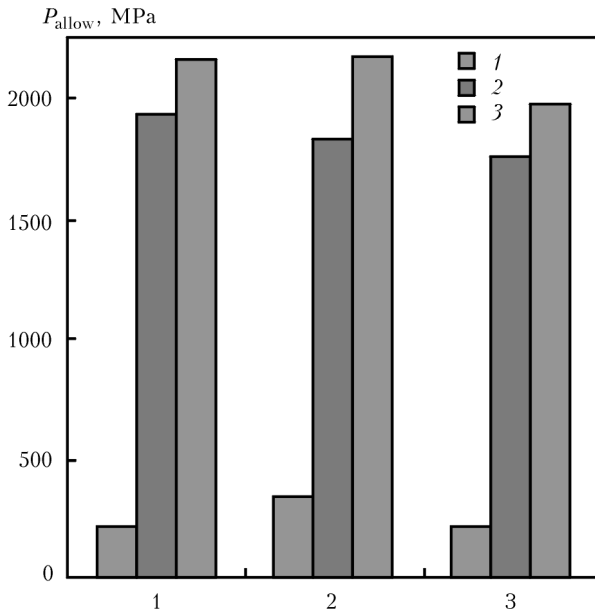


**Figure 2.** Values of forming allowable pressures in internal (1), external (2) and common (3) wall of the balloon in samples 1–3

can be perspective in development of tubular billets and balloon bodies (Figure 4). The material represents itself one layer of solid sheet material, joined with another layer (nonsolid sheet material) by welding over the whole adjacent area.

Production of such external shell from steel grades having increased strength allows:

- uniform distribution of loading in «rods» of the shell and partial reduction of its thickness;
- providing of reduction of shell weight by value of volume weight of cell metal of mesh-like sheet material.

It is a well-known fact that the radial (circumferential) stresses, appearing in the cylindrical shell under the effect of internal pressure, is 2 times larger than the axial stresses (stresses along the cylinder generatrix) [1–3]. Positioning

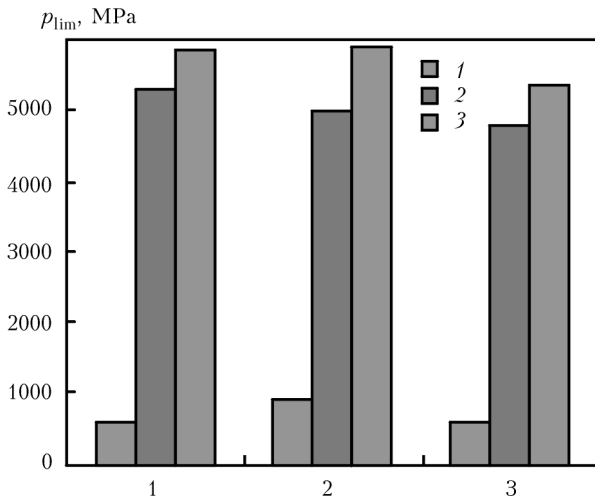


**Figure 3.** Values of forming limiting pressures in internal (1), external (2) and common (3) wall of the balloon in samples 1–3

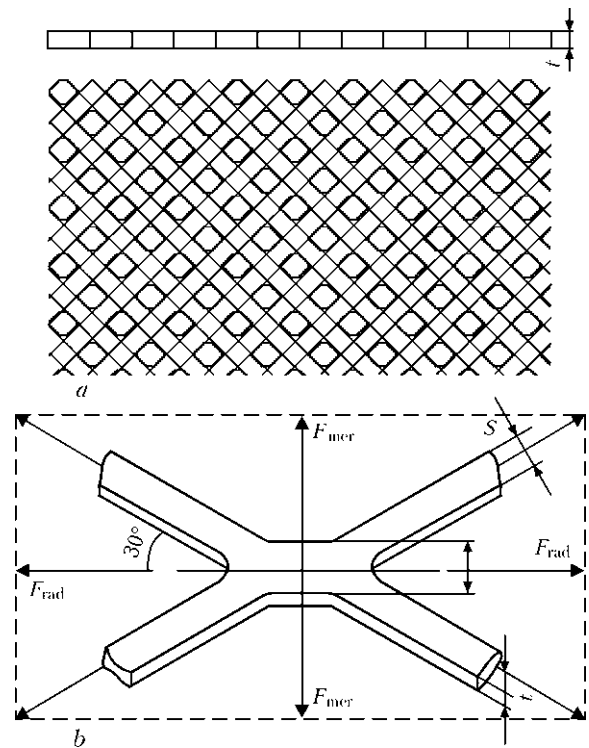


**Figure 4.** Sheet material with mesh-like structure (a) and nod, in which four rods intersect (b)

of intersecting rods at 60° angle in its specific putting on cylindrical surface (internal shell) allows developing uniform distribution in radial as well as axial directions in the rods of such shell from effect of internal pressure. At that, the density of distribution along the surface in radial direction will be 2 times higher the density in axial direction (Figure 5).

Computer simulation of internal pressure loading of the model of two-layer balloon, the external shell of which is produced from sheet material with mesh-like structure of specific thickness, confirms the relevance of application of given material (Figure 6). Formation of centers of stress concentrators in the nodes of mesh-like material can be eliminated by approximation of rhomb profile of mesh cell to elongated ellipse profile (Figure 7).

Important factor, effecting the application of that or another mesh-like external shell, is determination of sizes of the mesh cell. In the external shell they depend and are determined based on thickness of material, used for manufacture of internal shell and its strength characteristics. Thus, the calculation models of three single type structures of two-layer balloon use external shell cell of 10 mm maximum gap in manufacture of internal shell from steel St.05kp, and that makes 20–15 mm in manufacture of internal shell from steel 20. At that, thickness of external shell  $t$  and width of rod  $s$  have the similar values. However, final determination of size of

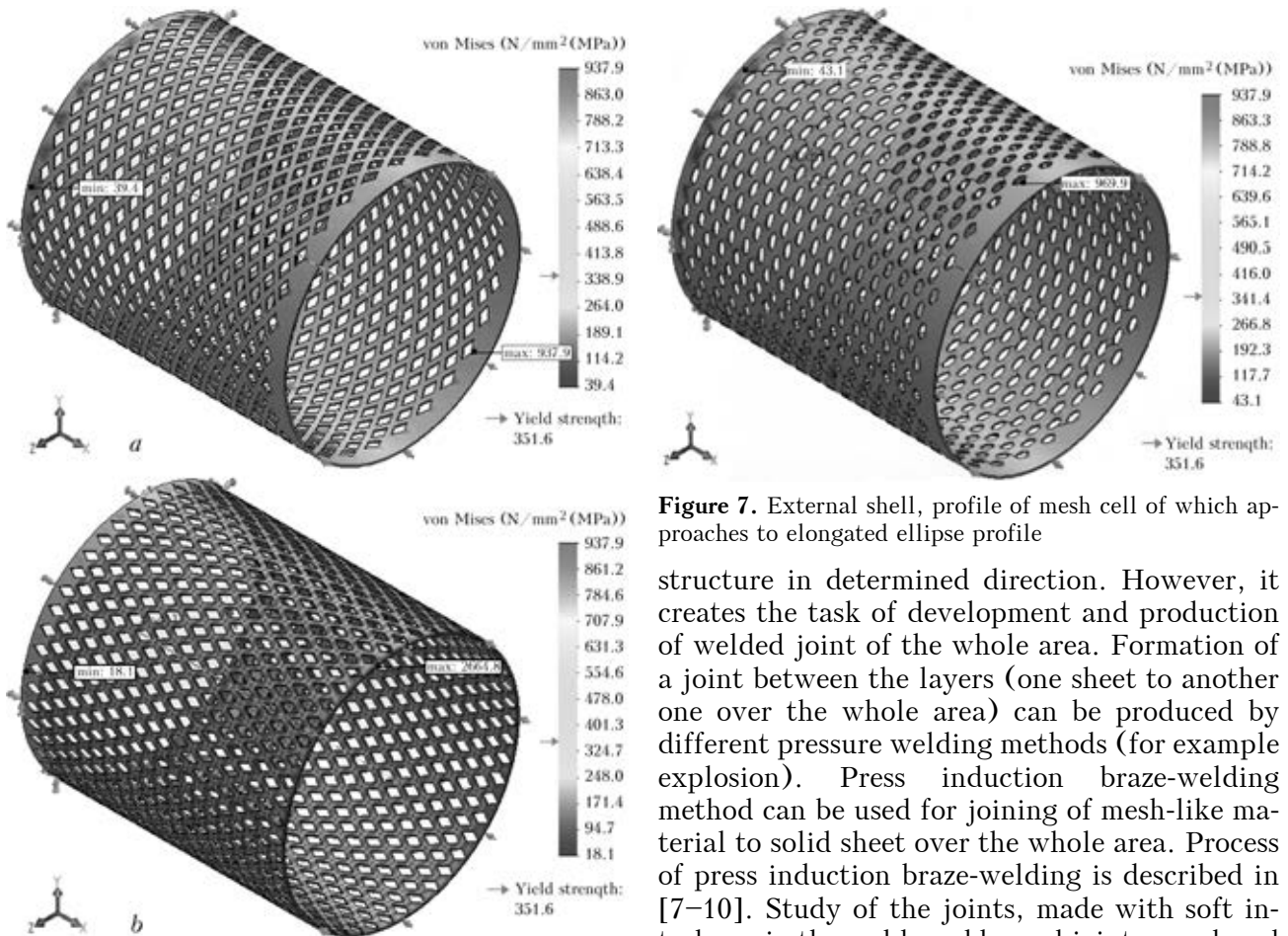


**Figure 5.** Level and distribution of stresses forming as a result of effect of internal pressure (internal cylindrical shell for the purpose of obviousness is not shown): *a* – external shell, manufactured from sheet material with mesh-like structure of specific thickness, in the nodes of which four rods intersect; *b* – external shell, 90° turn

the external shell cell requires testing of samples of two-layer wall and full-scale tests of two-layer balloon.

Development of such multi-layer sheet structures is perspective from point of view of material saving, reduction of specific weight and preservation of strength properties of such welded

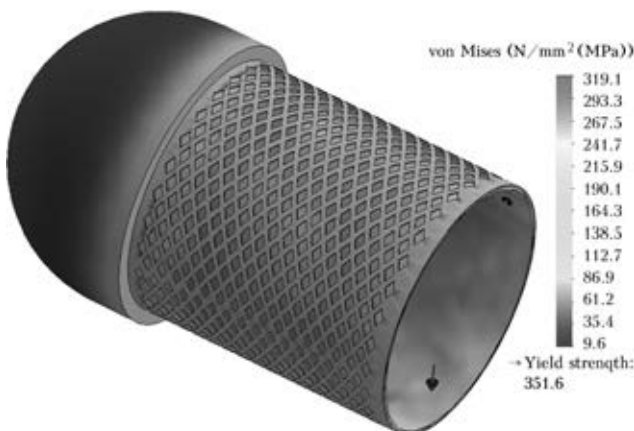


**Figure 6.** Simulation of loading of model of two-layer balloon by internal pressure

**Figure 7.** External shell, profile of mesh cell of which approaches to elongated ellipse profile

structure in determined direction. However, it creates the task of development and production of welded joint of the whole area. Formation of a joint between the layers (one sheet to another one over the whole area) can be produced by different pressure welding methods (for example explosion). Press induction braze-welding method can be used for joining of mesh-like material to solid sheet over the whole area. Process of press induction braze-welding is described in [7–10]. Study of the joints, made with soft interlayer in the weld, and brazed joints, produced with upsetting and plastic strain of weld zone [11, 12], preceded its appearance.

A joint in this work was produced by press induction braze-welding, using activating substances previously applied over the surface of solid sheet and further HFC heating. Weld formation takes place in area of specific length with thermomechanical effect in form of elasto-plastic strain with further pressure solidification, which

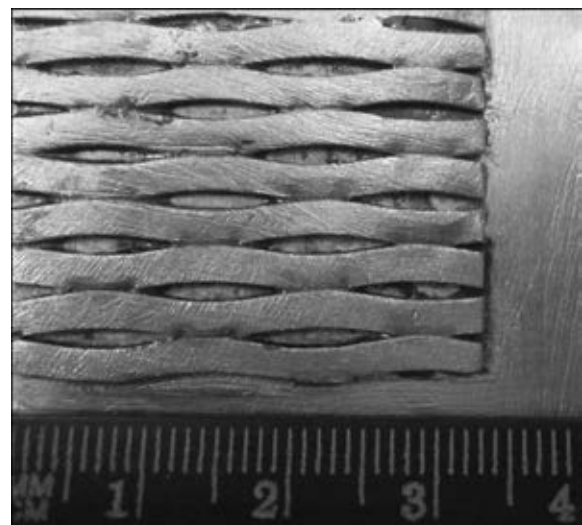


**Figure 8.** Fragment of whole area joint of mesh-like material to solid sheet material, produced by press braze-welding



approaches to uniform volume distribution. It allows receiving uniform weld metal composition with increase of its strength characteristics. Use of press braze-welding provides for development of multi-layer structures using the metals, welding of which by traditional methods is difficult (Figure 8).

Application of HFC heating in manufacture of two-layer shell of the vessel-balloon bodies allows performing thermal-mechanical shrinkage of the external shell relatively to internal one, i.e. technology of fitting on with tension, that significantly increases structural strength of compound wall of the whole balloon.

It is reasonable when the balloon wall is made compound, i.e. two-layer, in order to receive more uniform distribution of stresses along the thickness of balloon wall.

Manufacture of the internal shell from solid sheet material is caused by general requirement to the balloon, namely sealing and capability to withstand set calculation pressure. The welds should also be seal, dense and maintain set pressure. Designation of the external shell is to provide more uniform distribution of stresses along the total thickness of wall and unload the internal shell.

### Conclusions

1. Stresses in the internal shell during working pressure loading of the balloon is higher than that in the external shell of balloon body, at that the balloon common wall is underloaded.

2. Using of the same steel grade in two-layer balloon structure does not result in efficient loading of the balloon common wall.

3. Application of the material with higher strength properties in manufacture of the exter-

nal shell results in efficient loading of the balloon common wall, that in turn provides for the possibility of reduction of thickness of its wall, growth of internal stresses in it, i.e. relevant balloon loading.

4. Press fit on of the external shell of balloon body on the internal shell allows optimizing loading of the balloon common wall from effect of internal pressure.

1. Pismenny, A.S., Prokofiev, A.S., Gubatyuk, R.S. et al. (2012) Increase of strength characteristics of spirally-welded pipes of structural designation. *The Paton Welding J.*, **3**, 30–34.
2. Pisarenko, G.S., Yakovlev, A.P., Matveev, V.V. (1988) *Handbook on strength of materials*. Ed. by G.S. Pisarenko. 2nd ed. Kiev: Naukova Dumka.
3. Majzel, V.S., Navrotsky, D.I. (1973) *Welded structures*. Leningrad: Mashinostroenie.
4. Forum, A.M. (2009) Our balloons will withstand any storm! *AGZK+AT*, **2**, 31–33.
5. Sakhatov, R.M. (2009) Nonshatterable metal-composite cylinders BMK-300V and others. *Ibid.*, **4**, 51–55.
6. Chernega, V.I. (1976) *Safety servicing of steam boilers, vessels and pipelines* (Transact. of official documents). 2nd ed. Kiev: Tekhnika.
7. Tabelev, V.D. (1991) Peculiarities of joint formation in brazing with plastic deformation of base metal. *Avtomatich. Svarka*, **7**, 5–9.
8. Tabelev, V.D., Kareta, N.L., Panasenکو, A.I. et al. (1985) Structure and phase composition of welds made by capillary and pressure brazing. *Ibid.*, **11**, 26–29.
9. Lebedev, V.K., Tabelev, V.D., Pismenny, A.S. (1983) Butt pressure brazing. *Ibid.*, **9**, 25–27.
10. *DSTU 3761.2–98: Welding and related processes*.
11. Bakshi, O.I., Shrou, R.Z. (1962) Strength under static tension of welded joints with soft interlayer. *Svarochn. Proizvodstvo*, **5**, 6–10.
12. Lebedev, V.K., Pismenny, A.S., Kasatkin, O.G. et al. (1990) Physical modeling of upsetting in butt welding and braze-welding of pipes. *Avtomatich. Svarka*, **8**, 17–20.

Received 11.06.2014

# INDUSTRIAL ELECTRON BEAM INSTALLATION L-8 FOR DEPOSITION OF HEAT-PROTECTIVE COATINGS ON TURBINE BLADES

N.I. GRECHANYUK, P.P. KUCHERENKO, A.G. MELNIK, D.V. KOVALCHUK and I.N. GRECHANYUK\*  
SPE «Eltechmach» Ltd.»

25 Vatutin Str., Vinnitsa, Ukraine. E-mail: eltechmach@gmail.com

The electron beam technologies find ever wider application in the world in production and repair of turbine blades. Equipment for their realization is manufactured in Germany, USA, Ukraine and other countries. The work describes the design features and technological capabilities of industrial electron beam installation L-8 for deposition of heat-protective coatings on turbine blades, designed at the scientific and production enterprise «Eltechmach». The distinguishing feature of the installation is its capability to deposit all the modern heat-protective coatings in the one type of equipment and, if necessary, for one technological cycle. The problem of preheating of blades in lock chambers of the installation, their ion cleaning before deposition of heat-protective coating, and also formation of barrier microlayers between functional layers of heat-protective coatings was solved to delay the diffusion processes at their interfaces and to control the thickness of heat-protective coatings. 14 Ref., 3 Figures.

**Keywords:** *electron beam installation, heat protective coatings, gas turbine blades*

At the present time a special attention is paid to the creation of specialized electron beam equipment for deposition of heat-protective coatings (HPC) on turbine blades. Among the leading world producers are the companies ALD Vacuum Technologies, Von Ardenne, Pratt&Whitney, the E.O. Paton Electric Welding Institute of the NAS of Ukraine, etc. In particular, a number of industrial EB installations for deposition of HPC was manufactured by PWI and successfully operate [1–4]. The general feature of these installations is application of flat-beam electron guns with the service life of cathode of not more than 50 h.

The certain achievements in creation of the similar equipment were attained at the SPE «Eltechmach» [5–13].

The distinguishing feature of industrial EB installation L-8, designed by «Eltechmach», is the application of gas-discharge guns and possibility of deposition of all types and designs of protection coatings: metallic, ceramic, composite, cermet, single-layer, multilayer, gradient, etc. The HPC, complicated by their chemical composition and design, can be formed on the gas turbine blades in the given installation for one technological cycle.

## Technical data of industrial EB installation L-8

Dimensions of cylindrical cassette with products, mm, not more than:	
diameter .....	250
length .....	500
Speed of product rotation at the horizontal rod, rpm .....	0.5–50
Number of evaporators, pcs .....	4
Inner diameter of crucibles, mm .....	70
Length of ingots being evaporated, mm .....	not more than 500
Speed of ingots feeding, mm/min .....	0.5–350
Distance from the upper cut of crucibles to axis of cassette rotation or plane of spraying, mm .....	350
Number and rated power (kW) of electron guns:	
for evaporation of materials from crucibles .....	4×100
for heating of products .....	2×60
Type of electron guns – axial with cold cathode (on the base of high-voltage glowing discharge)	
Consumed power, kW, not more than:	
by high-voltage power sources .....	520
by auxiliary equipment .....	80
Rated accelerating voltage, kV .....	30
Working vacuum in chambers, Pa (mm Hg) .....	$6 \cdot 10^{-3}$ – $6 \cdot 10^{-2}$ ( $5 \cdot 10^{-5}$ – $5 \cdot 10^{-4}$ )
Dimensions of installation, mm, not more than:	
length .....	10500
width .....	9500
height .....	4300
Mass of installation (with power sources), t .....	not more than 25

The general view of the installation is given in Figure 1.

The installation represents the unit of vacuum chambers with mechanisms, devices and systems providing performance of technological process of deposition of coatings in vacuum. The scheme of chamber for deposition of coatings is given in

\* V.I. Melnik, I.V. Melnik and B.A. Tugaj participated in this work.

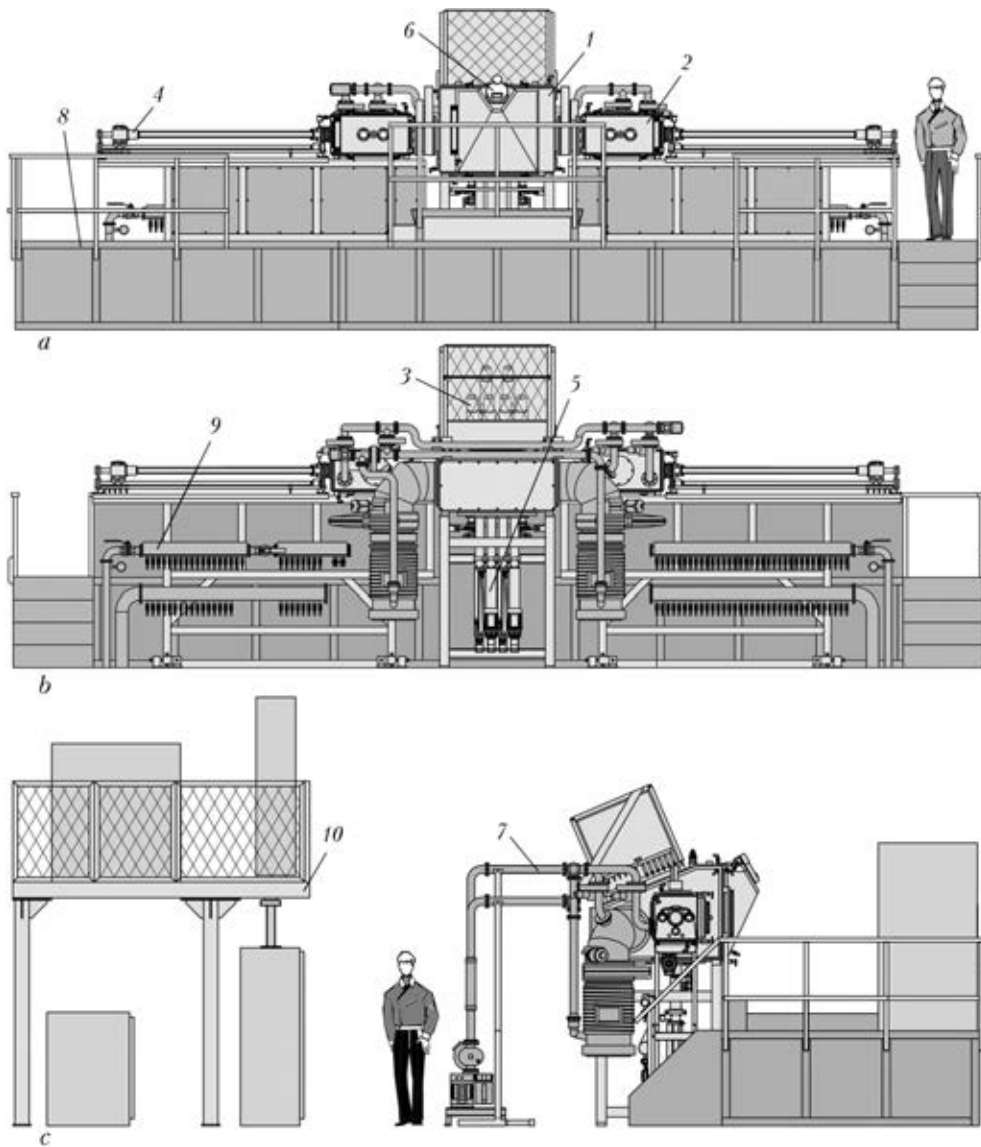


**Figure 1.** General view of installation L-8: *a* – front view; *b* – back view; *c* – left view; 1 – technological chamber; 2 – lock chamber; 3 – electron guns; 4 – mechanism of cassette (products) feeding; 5 – mechanism of ingot feeding; 6 – sight system; 7 – vacuum system; 8 – service area; 9 – cooling system; 10 – platform of high-voltage power sources

Figure 2. The appearance of the installation is given in Figure 3.

In the technological (working) chamber of installation (see Figure 2) the process of deposition of vapor flow on the billets, being coated, occurs. In working chamber the vacuum of  $5 \cdot 10^{-5}$ – $5 \cdot 10^{-4}$  mm Hg is maintained. Below the chamber the unit of evaporators is attached, in the composition of which four copper water-cooled crucibles and four mechanisms for feeding the evaporating ingots are included. The loading of ingots of evaporating materials into the mechanisms is performed atop through the crucibles. The electron guns are mounted on the upper cover of working chamber.

Two synchronically operating gates are designed for screening of parts being coated during initial heating of evaporating materials and parts

before setting up of stable technological mode of evaporation. Two other gates, mounted in the working chamber, serve for protection of shutters, dividing the lock and working chambers, from dusting and high temperature during carrying out of technological process.

On the upper wall of chamber the sensor for control of thickness of depositing coatings is mounted, and on the back wall – ball input with sight tube and peephole for the possibility of contact-free measurement of temperature. The measurement of temperature of products in installation is performed using high-technological infrared pyrometer and special software. The electromagnetic gas inlet valves with system of flow stabilization, providing the dosing inlet of technological gases, are mounted on technological and loading chambers.

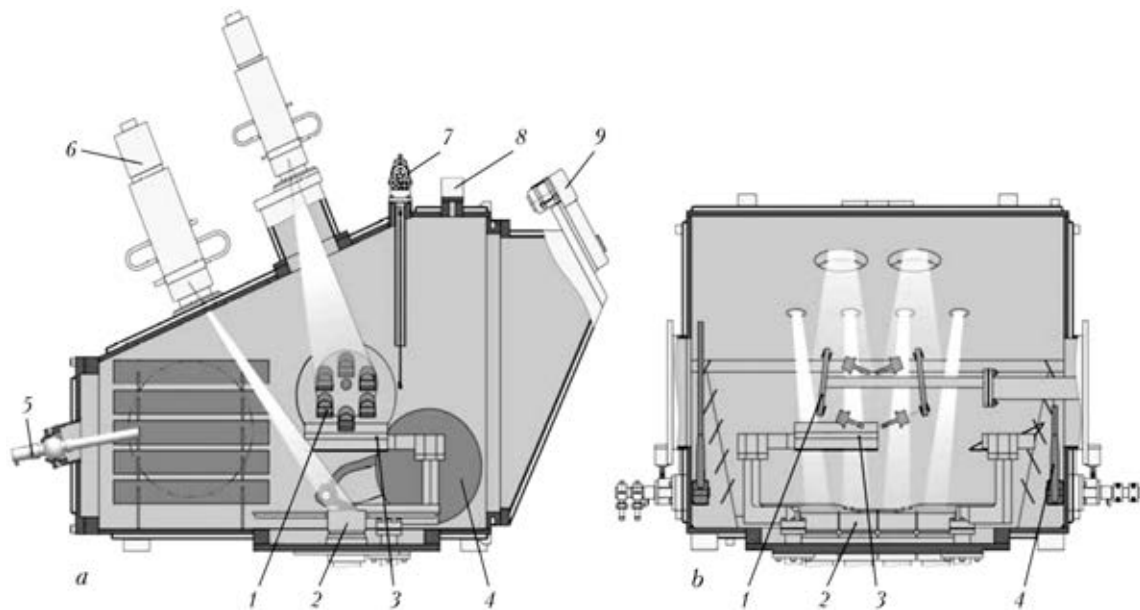


**Figure 2.** Scheme of technological chamber of installation: *a* – transverse section; *b* – longitudinal section; 1 – cassette with blades; 2 – crucibles; 3 – gates of evaporators; 4 – gates of shutters; 5 – ball input for mounting of pyrometer; 6 – electron gun; 7 – weighing sensor; 8 – inlet valve for technological gas; 9 – sight system

The adding of low amount of gas (argon) to the process of evaporation results in dispersion of vapor flow, which allows performing the more uniform deposition of material to open and shadow areas of the product [3].

In the installation the capability to perform a partial ionization of technological gas and metal vapor by supply of negative potential (up to 2 kV) to the products is also envisaged. The ionization facilitates the producing of coating with favorable structure without crystallographic defects, which arise in the condensed layer during inlet of gas [14].

The possibility of oxygen supply to the chamber during deposition of ceramics to provide its stoichiometric composition is also envisaged.

The lock chambers are designed for reloading of the products being coated. Separation of volumes of the chambers mentioned-above is carried out by two vacuum shutters of  $d = 320$  mm. The

presence of two auxiliary chambers increases the installation efficiency. The deposition of coatings on the products, supplied one by one from the lock chambers, is occurred without evacuation of technological chamber.

In the lock chambers of installation the possibility to carry out the ion cleaning of products before deposition of coatings is envisaged, which allows improving the adhesion of deposited layer with a part, and also depositing barrier micro-layers between the functional layers of HPC with the purpose of delaying the diffusion processes at their boundaries. For this purpose the installation is equipped with arc evaporators, which are mounted on each loading chamber, and system for the control of ion cleaning. In the control cabinet the power sources of arc evaporators and two adjustable sources of bias voltage are located, which is supplied to the rigging with products in the process of cleaning. Thus, the cleaning

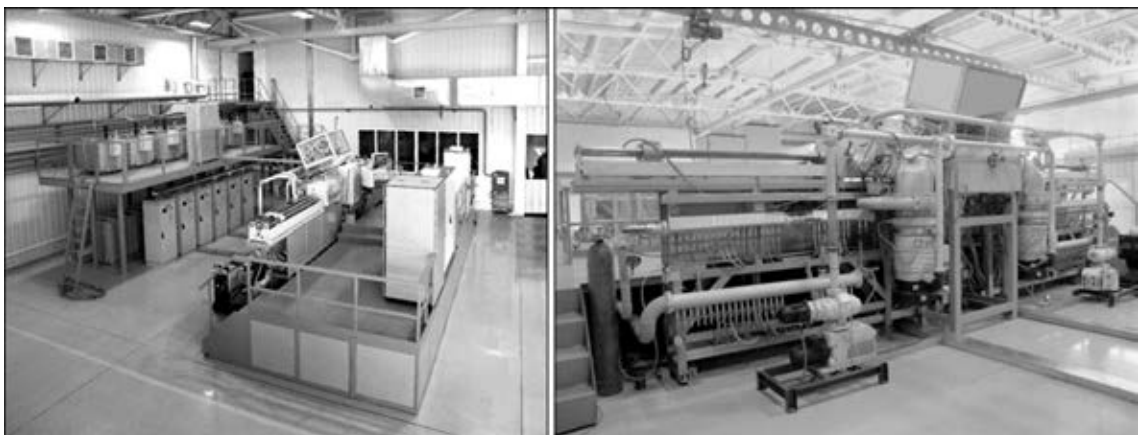


**Figure 3.** Appearance of EB installation L-8



can be performed in two modes: preliminary degassing and cleaning of products by glowing discharge in argon by supply of negative potential of up to 2 kV to the rigging with products relatively to the chamber casing, and cleaning by bombardment of parts with ions of metal using arc evaporator and supply of bias voltage to the rigging.

As the cathode the alloy CrLaFe is used in evaporator. As a result of burning of arc discharge in vacuum the ionization and spraying of cathode material occurs. The control of bias voltage at the products allows changing the rate of deposition of sublayer and temperature of heating of parts as a result of bombardment.

The mechanisms of horizontal feeding of products serve for movement of sprayed products from pre-chambers to working chamber and vice-versa and also for rotation of rigging with products. To compensate the possible deflection of rod in the extreme protruded position the front support of rod is made on pivots.

The introduction of horizontal rod to the chamber is performed so that the tightening of advancing and rotational movement of rod is performed by different tightening devices. Such a cross coupling prevents a quick coming out of order of a cup-type seal of advancing rod movement. The rods are equipped with current collector to supply the bias voltage through the hollow shaft to rigging with products. The bias voltage of up to 2 kV is required to perform the ion cleaning of products.

The vacuum system of the installation is designed using the completing parts of Oerlikon Leybold Vacuum (Germany) and VAT (Switzerland). The shutters and valves with pneumatic drive are used. During switching-off of electric power or drop in pressure of the compressed air all the valves and shutters are automatically closed under the action of built-in springs. The forevacuum pumps are characterized with low level of noise and are completed with filters for purification of exhausted fumes. The Roots pump has a built-in valve of protection against the excessive drop of pressure at inlet and outlet and allows beginning of pumping-out at the atmospheric pressure at inlet simultaneously with switching-on of the forevacuum pump. As a result, the speed of pumping of pumps combination is increased. The oil-vapor pumps are supplied with vapor catching trap and have built-in thermostats for protection against the oil overheating and exceeding of cooling water temperature.

The system of vacuum control provides the automatic emergency closing of shutters of high-

vacuum pumps during drop of vacuum in the chambers below  $10^{-1}$  mm Hg and also emergency stoppage of pipelines during pumping of mechanical pumps at sudden interruption of power supply.

The direct control of vacuum system is performed in automatic or manual mode using sensor panel of operator, which has a separate control window for this purpose. The information about the state of vacuum in main pipelines of vacuum system, pumps, chambers, etc. is displayed on the operator panel. To measure vacuum in the installation the vacuum gauges with output signal proportional to pressure are used. All measuring signals from vacuum meters are processed using industrial controller and displayed on the operator panel. The cooling system of the installation provides supply of cold water to the units and assemblies requiring cooling. The flow of water through the most critical units (crucibles, pumps, guns) is controlled using flow sensors. The temperature of cooling water is also controlled. When flow is absent or the preset value of temperature is exceeded, the protective switching-off of accelerating voltage sources is operated. Information about the water presence or absence is displayed on the screen of operator.

The sight system located on the front door of technological chamber represents a stroboscopic device for monitoring the surface of molten ingots in crucibles and heating of products.

Four EB guns of 100 kW power are installed for evaporation of materials from crucibles in such a way that each gun, designed for evaporation of ingot from the certain crucible, can also evaporate the material from the neighboring crucible. To heat the products, two guns of 60 kW power are used.

In the installation the gas-discharge EB guns are applied.

#### Technical parameters of EB guns of 100 kW power

Accelerating voltage, kV .....	not more than 30
Maximum beam current, A .....	3.3
Diameter of spot in the beam focus, mm .....	≈10
Angle of deflection of electron beam from the axis, deg .....	15
Frequency of electron beam scanning, Hz .....	not more than 50
Current of focusing lenses, A .....	not more than 0.95
Working pressure in technological chamber, Pa .....	not more than $10^{-1}$
Working gas .....	commercial hydrogen, mixture of hydrogen and oxygen, etc.
Maximum gas consumption, l·atm/h .....	not more than 10
Consumption of cooling water with temperature of $15\pm 5$ °C at pressure of 0.3 MPa, l/min .....	15

The use of cold cathode of low-alloyed aluminium alloy excludes any its distortion, which





provides a stable electron beam. The total life of cathode amounts to about 1000 h. The use of electromagnetic focusing system in the guns with cold cathode provides a quality beam with minimum diameter of focal spot of about 10 mm.

The principle of operation of gas-discharge gun is based on generating and formation of electron beam in high-voltage glowing discharge. During operation of the gun the high-voltage glowing discharge with plasma is burning in its discharge chamber (between cathode and anode), being localized near the anode and separated from the cathode by the area of cathode potential drop. Plasma emits positive ions, which are accelerated by the field in the area of cathode drop and bombard the cathode, causing the emission of electrons. The field of cathode potential drop accelerates the electrons and forms the converging electron beam with the crossover, located at the distance from cathode close to the radius of curvature of its emission surface (near the hole in anode).

The magnetic field, generated by the first focusing lens, forms an electron beam close to cylinder by its shape, and due to this it passes through the beam conductor to the technological chamber without power losses. Using the second focusing lens the beam is focused on the surface of melt and with the use of deflection systems the program beam scanning is performed.

The control of discharge current is provided by control of pressure of working gas in the gun at its continuous pumping-out together with technological chamber of the installation. For effective control of discharge current and stabilization of operation mode of gun the system of automatic inlet of gas is used.

The system for control of EB guns provides control and stabilization of beam currents, currents of electromagnetic lenses, control of position and scanning of beam, and also allows performing deposition of laminar (microlaminar) coatings.

The installation consists of six high-voltage power sources to supply six EB guns with direct current of high voltage. High-voltage power source provides conversion of three-phase alternating voltage to the direct voltage, limitation of short circuiting currents, switching-off of high voltage during breakdowns in guns, and also automatic repeated switching-on.

One set of high-voltage power source includes the following components: cabinet of starting-protection equipment, current-limiting choke, and high-voltage transformer.

High-voltage converter is composed of power high-voltage transformer, rectifier unit and high-voltage dividers placed into one oil-filled body.

The system of electric drive control provides control of mechanisms of ingots feed, mechanisms for feed and rotation of side shafts, sight system, crucible gates and gates of interchamber shutters.

The motors of mechanisms for feed of ingots are equipped with encoders, the output signal of which is supplied to the frequency converters and used to stabilize and widen the range of ingots feed speed control.

The signals from encoders on the mechanisms for feeding ingots and feeding of side shaft are also used by the system on the base of PLC for positioning and measuring of feed speeds of the mentioned mechanisms. The setting of zero values of rod position is performed automatically during response of end switches. The position of mechanisms and speed of shaft rotation are displayed on the screen of operator.

The system of control of side shafts feeding allows performing the reciprocal movement of rigging with products in the process of coating deposition in the preset limits and at the preset speed to provide uniformity of coatings, being deposited, around the perimeter of products.

The automated system for control and monitoring of technological parameter provides automatic acquisition and visualization of technological parameters in real time, documentation of information in the database, performance of functions of automatic and manual control of vacuum system of the installation.

The complex is composed of two main systems: system of control, acquisition, processing and visualization of technological information on the base of industrial program controller and sensor panel of operator, and information-recording system on the base of industrial computer with the operational system Windows®.

The software of the sensor panel of operator was developed in the form of multiwindow interface. In the window «Symbolic Circuit» the symbolic circuit of all the vacuum system with display of digital values of vacuum in seven points according to received data from the control system is presented. The system for control of vacuum pumping-out gives operator a possibility to work in manual, automatic and service modes.

In manual mode the operator is given a possibility to control the vacuum equipment on his own discretion. In this mode the control system puts into operation the program lockups, which do not allow operator to carry out incorrect actions as to the vacuum system. Moreover, only those control elements are displayed on the symbol circuit, with the help of which the actions



can be performed, and those become unavailable which are dead.

During switching to the automatic mode a block of buttons appears on the screen, which are used to perform functions of automatic pumping-out of vacuum chambers, inlet of air and also switching-off the installation after finishing of work and return of vacuum system to the initial state. The mode «Service» releases all the lockups and is used only for setting-up the system of management of engineering workers attending the installation. To activate the mentioned mode it is necessary to enter the access password.

In the window «Process» the values of accelerating voltages, beam currents of electron guns, speed of feeding ingots and their remnants, value of vacuum in the working and loading chambers, position of horizontal shafts, values of weighing sensor, temperature of product, presence of water flow in the cathodes and anodes of electron guns and crucibles, etc. are displayed.

The windows «Vacuum diagrams», «Temperature diagram» and «Beam currents» present the possibility of observation of the change of mentioned parameters in real time.

The efficiency of the installation is up to 60,000 coated blades per year. The installation passed successfully the industrial tests and is put into industrial service at SPA «Saturn» (Rybinsk, RF).

## Conclusions

1. The design was developed, electron beam installation L-8 for deposition of HPC on the gas turbine blades was manufactured and successfully put into industrial service.

2. The problem of preheating of blades in the lock chambers of the installation, their ion cleaning before deposition of HPC, and also formation of barrier microalloys between the functional layers of HPC to delay the diffusion processes at their interfaces was solved.

3. The problem of thickness control in the process of HPC deposition was solved.

- Pap, P.A., Malashenko, I.S., Ivanov, A.M. (1975) Laboratory installation for producing of protective coatings of different purposes by electron beam vacuum condensation. *Spets. Elektrometallurgiya*, Issue 27, 98–104.
- Chvertko, A.I., Shcherbitsky, V.V., Movchan, B.A. et al. (1982) Commercial electron beam installation UE-175M for deposition of protective coatings on gas turbine blades. *Ibid.*, Issue 50, 53–61.
- Movchan, B.A., Malashenko, I.S. (1983) *Heat-resistant vacuum-deposited coatings*. Kiev: Naukova Dumka.
- Movchan, B.A., Yakovchuk, K.Yu. (2004) Electron beam installations for evaporation and deposition of inorganic materials and coatings. *Advances in Electrometallurgy*, 2, 9–14.
- Grechanyuk, N.I., Kucherenko, P.P., Osokin, V.A. et al. (2000) State-of-the-art and prospects of producing of thermal barrier coatings for gas turbine blades and equipment for their deposition. *Novyny Energetyky*, 9, 32–37.
- Grechanyuk, N., Kucherenko, P., Osokin, V. et al. (2013) New materials, coatings and electron-beam equipment for their production. In: *Proc. of Int. Conf. on Electron Beam Technologies* (Varna, Bulgaria, 2013), 258–264.
- Grechanyuk, N., Kucherenko, P. *Installation for coating parts using electron beams*. Pat. 2451682 Canada. Publ. 23.05.2005.
- Grechanyuk, N., Kucherenko, P. *Installation for electron-ray coatication of coatings*. Pat. 6923868 B2 US. Publ. 2.08.2005.
- Grechanyuk, N.I., Kucherenko, P.P. *Installation for electron beam deposition of coatings*. Pat. 2265078 RF. Introd. 27.11.2005.
- Grechanyuk, N., Kucherenko, P., Grechanyuk, I. et al. (2006) Modern technologies and equipment for obtaining of new materials and coatings. In: *Proc. of 8th Int. Conf. on Electron Beam Technologies* (5–10 June, 2006, Varna, Bulgaria), 122–128.
- Grechanyuk, N.I., Kucherenko, P.P., Grechanyuk, I.N. (2007) New electron beam equipment and technologies of producing advanced materials and coatings. *The Paton Welding J.*, 5, 25–29.
- Grechanyuk, N., Medzinski, B., Grodzinski, A. (2010) Modern electron beam technologies for fabrication of various materials, powders and metal compositions from a vapour phase. *Przeglad Elektrotechniczny*, 5, 1–4.
- Grechanyuk, N., Melnik, A., Grechanyuk, I. et al. (2014) Modern electron beam technologies and physical vapor deposition of different materials. In: *Proc. of 11th Int. Conf. on Electron Beam Technologies* (8–12 June, 2014, Varna, Bulgaria), 115–121.
- Boone, D.H., Lee, D., Shafer, J.M. (1977) The electron beam coating of turbine components and ion plating. In: *Proc. of Conf. on Ion Plating and Allied Technologies* (Edinburgh), 141–148.

Received 01.09.2014

# COMPUTER-BASED TECHNOLOGIES AND THEIR INFLUENCE ON WELDING EDUCATION

S. KEITEL<sup>1</sup>, C. AHRENS<sup>2</sup> and H. MOLL<sup>2</sup>

<sup>1</sup>SLV Halle GmbH

33a Koethener Str., 06118, Halle, Germany. E-mail: keitel@slv-halle.de

<sup>2</sup>GSI mbH

85 Bismarckstraße, 47057, Duisburg, Germany

Ideas for the improvement of education in welding are close linked with the development of personal computer worldwide. Based on IIW guidelines it was a challenge to transform the new quality of computer-based technologies into programs to educate different players in welding. Computer-based training for engineer was the starting point of these activities in 2003. Until now roughly 1000 engineers were educated first by self study on computer and then using Internet-learning platform. In case of training of welders we followed a different way. Learning from training methods of high sophisticated sportsmen a virtual welding training system (VWTS) using real small arc was developed. Welder were trained step by step but with permanent instructions from the computer control unit to correct the practice. In addition there is a permanent changing between training by VWTS and real welding in a welding cabin. 10 Figures.

**Keywords:** *welding production, personnel, training, education programs, computer-based technologies, virtual systems*

**Significance of training and continuing education.** Training and qualification are considered by our society to be the most important requirements for recognition and moving up the social ladder. In the industrialised nations, as well as emerging or developing ones, they are thus important elements for the development of individuals and, at the same time, a prerequisite for social peace.

Training and continuing education represent powers of production, since demand for qualified personnel is continuously increasing to help realize the creation of constructions and safeguarding of production. The increase in complexity in products and processes can only be accomplished by well-trained personnel.

This is the case for both skilled workers and engineers. It is therefore essential to expand further development of training methodology to its full potential.

One of the most important driving forces for industrialised societies in the last 20 years is the advent of computer applications and Internet. For this reason welding technology and, in particular, training programs for future qualified welders must meet this challenge head on by developing those advantages that can be gained through the deployment of information technology.

In light of the construction last year (2012) of a new purpose-built training facility for weld-

ing technology by DVS and German Association for welding and related practices, new computer-supported training methods are being combined with more traditional ones to generate a concept that, above and beyond the field of welding, envelopes the entire sector of metal-working (Figure 1).

**Use of computers in direct relation to the training of professional welding personnel.** In reference to practical welding training or training of machine operators, we have identified the fol-



**Figure 1.** New development of the Bildungszentrum Rhein-Ruhr (BZRR) Gelsenkirchen-Schalke Site



Figure 2. VWTS as a virtual system

lowing factors, whereby computers have changed the world of welding:

- selection and regulation of welding parameters within the electric power source;
- monitoring of welder by means of process control (parameter surveillance and surveillance of welding workshop);
- ergonomics in the design of equipment;
- body posture for welding (technical evaluation);
- training for welder (development of hand coordination).

Emphasis should be placed on the following elements.

**Practical training for welders.** *Impact of electric power source on theoretical knowledge of a welder.* It is impossible to imagine our modern power source technology and component handling without computers. Power sources today are capable of storing complete welding technologies in finished programs, and provide every welder with efficient handling and error-free selection of the appropriate welding parameters.

More specifically, power sources are now capable of, regarding their regulation mechanisms, analyzing the welding process and adjusting to parameters. Particularly through the advent of pulse technology, the drop transfer is controlled,



Figure 3. Semi-virtual VWTS with real low-capacity electric arc

which in the end provides the welder with more time to concentrate on his/her manual skills. The power source thus assumes tasks that were heretofore dependent upon the manual skills of individual welder.

The simplified operation of power sources should, however, not lead to the welder being occupied merely with his/her manual skills. It is rather necessary today to put more emphasis on the welder's theoretical knowledge. He/she is the one who has to be able to recognize disruptions in the process and/or an improper selection of parameters. He/she is only capable of doing this when he/she has a thorough understanding of the welding process.

Welders today should also have a basic understanding of control technology, due to the fact that they sometimes have to be able to master both automatic and semiautomatic control processes.

*New methods in welding training.* A new paradigm has taken place recently in the organization of welding technology training, this is due to the ever-increasing investment in computer-supported training workstations. This equipment – virtual welding training systems (VWTS) – supports the conventional work of the instructor, in that it continuously monitors and corrects the student in his/her movements from beginning to end.

In principle, at least two methodologies can be implemented today, namely virtual and semi-virtual systems.

Figures 2 and 3 illustrate examples for application of the system in training. Figure 2 shows the system that generates a virtual weld in the monitor from the movements made by the welder. This and comparable systems guide the learning welder to real challenges through various levels of difficulty. Depending on the type of welding equipment, the workflow movements are however more or less different from the actual movements. But they are still quite suitable for the acquisition of fine-motor skills in welding.

As opposed to this, the semi-virtual systems function with a low-capacity electric arc. No real weld is produced, but the welder's movement on the metal plate (which is necessary to start the electric arc) can be followed as a melting line. The welder's movement workflow is recorded during the exercise and he/she receives visual and/or spoken instructions for correction. After welding, the following parameters are made available either in the monitor or printed out: torch position, welding speed, torch surface-distance and an overall comprehensive statement for evaluation.

The advantage of these facilities is that the original welding equipment may be used for the exercises. This involves for example an original torch with a cable-hose assembly with real materials and dimensions. The electric arc also supplies a weak current corresponding to a real glare shield in the form of a welder's helmet (see Figure 3).

*Manual skills in welding with electric arc.* Welding is then finally learned using the conventional process, since the energy impact of electric arc and the dynamic of weld pool are difficult to simulate. This means that the VWTS today can only cover 20–30 % of the overall learning curve for welding.

However, in comparison with competitive sport, a combination of methods will be used in the future that increases the challenges step by step, thus facilitating the welder's learning curve depending on his/her individual capacities.

In order to support the training process, differentiated VWTS can be used, for example, in combination or in sequence. It has been found that a suitable method is to combine the purely virtual systems with semi-virtual systems.

At the end of the process, however, the priority is the implementation of learned skills and their application in various positions and on metal plate of various thickness. This learning method has stood the test of time according to IIW Guideline 089–12.

The typical welding booth for training is shown in Figure 4.

*Use of welding booths and cabinets.* Training for welders usually takes place in a welding booth to protect those who are not involved from emissions of radiation and fume. Also, the welding teacher wears a dark helmet during welding training sessions. Training for the technique of welding to date therefore takes place in a kind of «darkroom», in which only the welder's (and instructor's) weld pool can be observed.

VWTS are offering for the first time the possibility of transferring the training process into custom-built, workshop-like training rooms and welding booths.

The welder-trainee can thus be observed and corrected regarding his/her sustainability of movement. Demonstrations given by the instructor, or exercises executed by the student can thus also be observed and assessed in groups.

*Role of instructor.* Computer-assisted methods in welding training with the benefit of VWTS enrich the educational process. They can complement, but not replace the traditional welding instructor. It is primarily human qualities and



Figure 4. Welder during training in welding booth

handicraft experience that provide young people in training with essential added-value. The instructor demonstrates not only theoretical skills and fundamental workflow movements for welding; rather, he/she makes decisions regarding which methods and which sequences should be used to best facilitate the advancement of knowledge. His/her communication skills are able to instil in young people the enthusiasm for welding.

This is why training sessions with instructors are so significant. They are the multipliers in the training process and determine success. This is true for continuing education within a company, initial training in educational facility and, as is the case in Germany, a dual system (Figure 5).

*Combination with metal-working.* If one seeks to thoroughly develop the skills of young people in fundamental training, a complex study of metalworking with the emphasis on welding has proved itself over the years. A good example of this is the workshop of the GSI training centres (Rhein-Ruhr), which involves training in welding with the application of new VWTS methods combined with training in metal-working. A systems mechanic, who has been trained in this manner receives, after exposure to such a dual concept, a nationally-recognized skilled-worker cer-



Figure 5. Expert assessment of results immediately after welding



**Figure 6.** Training workshop of BZ RR (a), training facility of GSI and DVS (b)

tification. Figure 6 illustrate various stations within the training workshop.

The fact that training can be carried out not only in a stationary workshop, but in a mobile one (Figure 7).

This is also a highly-widespread and modern method for the training of welders. The welding instructor must be more flexible by adjusting to operational requirements, while often times having to overcome language barriers as well.

**Traning for welding engineers.** Welding engineers are considered to be the central focal point for all questions regarding quality control in welding processes. Their technological qualifications, therefore, determine the quality of welded structures and products. This is why the qualification of expert welding engineers, within the context of welding-supervisor training, carries the highest priority.



**Figure 7.** Mobile training station

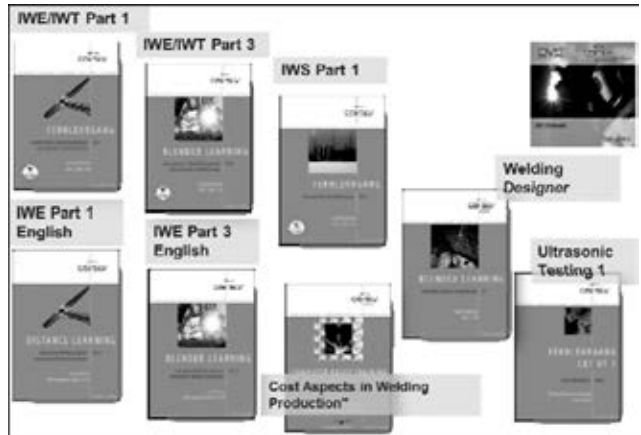


**Figure 8.** Distance learning courses of GSI at enterprise of German Welding Society

In Germany in recent years approximately 1,000 IIW welding engineers per year have been trained. The qualification of welding design engineers has also developed quite positively, since they represent the multipliers for new designs and applications for modern welding processes in the creation of products.

The successful increase in qualifications can be attributed to, in particular, the deployment of new learning methods, since approximately 350 participants are trained by GSI per year via computer-based learning or so-called blended learning. An overview of learning content, which is offered today through distance learning, is illustrated in Figure 8.

Distance learning courses require from the participants a high level of self-motivation. Independent mastering of the learning material is facilitated with visual support (Figure 9).

The course variation «Blended learning», which has been specially implemented for the training of welding engineers, is based on 50 % self-study and 50 % attendance in the classroom. The latter offers participants the opportunity of posing up-to-date issues and questions directly

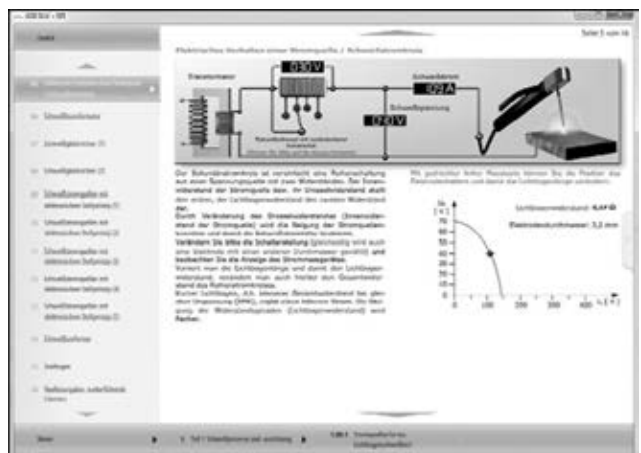


**Figure 9.** Screen with animations (example taken from distance learning course)

to the instructors and mentors, while providing the teachers an environment for immediately integrating latest information (e.g. technical standards) into the course.

The reason that distance learning courses are increasing in significance can be attributed to the opportunity to achieve a qualification through an extra-occupational program, thus corresponding to the trend of life-long learning. In this context, the impact of Internet must be respected, since questions from course participants are directly forwarded to the mentors and instructors. Modern terminal equipment and broad-band data connections support this trend as well (Figure 10).

Based on examples, taken from practical training of welders and continuing education for welding engineers, it has been illustrated here how the methodologies for transfer of knowledge have been enhanced for welding technology as well through the influence of new technologies and with aid from computers and Internet. This was necessary in this respect in order to develop, with the aid of new technologies, supplemental effects such as:

- more flexible training;
- individualisation of the training;



**Figure 10.** Modern tablet-PC as a terminal device for continuing education in welding technology

- structured learning.

On the other hand, it is also important to enable the preservation of resources, e.g. in the form of travel time, energy, less paper, etc.

This has a long-term impact on the overall training process and must be taken into consideration today in planning and investment for new educational facilities. Moreover, computer-based training methodologies form the basis for more-robust internationalisation of welding technology.

Received 15.01.2014

# PATON PUBLISHING HOUSE

www.patonpublishinghouse.com

## SUBSCRIPTION

**The Paton**  
WELDING JOURNAL

**АВТОМАТИЧЕСКАЯ  
СВАРКА**

«The Paton Welding Journal» is Published Monthly Since 2000 in English, ISSN 0957-798X.

«Avtomaticheskaya Svarka» Journal (Automatic Welding) is Published Monthly Since 1948 in Russian, ISSN 005-111X.

«The Paton Welding Journal» is Cover-to-Cover Translation of Avtomaticheskaya Svarka» Journal into English.

If You are interested in making subscription directly via Editorial Board, fill, please, the coupon and send application by Fax or E-mail.

The cost of annual subscription via Editorial Board is \$348 for «The Paton Welding Journal» and \$180 for «Avtomaticheskaya Svarka» Journal.

«The Paton Welding Journal» can be also subscribed worldwide from catalogues subscription agency EBSO.

### SUBSCRIPTION COUPON

Address for journal delivery \_\_\_\_\_

Term of subscription since \_\_\_\_\_

20

till \_\_\_\_\_

20

Name, initials \_\_\_\_\_

Affiliation \_\_\_\_\_

Position \_\_\_\_\_

Tel., Fax, E-mail \_\_\_\_\_

We offer the subscription all issues of the Journal in pdf format, starting from 2009.

The archives for 2009–2012 are free of charge on [www.patonpublishinghouse.com](http://www.patonpublishinghouse.com) site.



## ADVERTISEMENT

in «Avtomaticheskaya Svarka» and «The Paton Welding Journal»

### External cover, fully-colored:

First page of cover  
(190×190 mm) – \$700  
Second page of cover  
(200×290 mm) – \$550  
Third page of cover  
(200×290 mm) – \$500  
Fourth page of cover  
(200×290 mm) – \$600

### Internal cover, fully-colored:

First/second/third/fourth page  
of cover (200×290 mm) – \$400

### Internal insert:

Fully-colored (200×290 mm) –  
\$340  
Fully-colored (double page A3)  
(400×290 mm) – \$500

• Article in the form of advertising  
is 50 % of the cost of advertising  
area

• When the sum of advertising contracts  
exceeds \$1001, a flexible system  
of discounts is envisaged

Size of journal after cutting is  
200×290 mm

### Editorial Board of Journal «Avtomaticheskaya Svarka» and «The Paton Welding Journal»

E.O. Paton Electric Welding Institute of the NAS of Ukraine

International Association «Welding»

11, Bozhenko Str., 03680, Kyiv, Ukraine

Tel.: (38044) 200 60 16, 200 82 77; Fax: (38044) 200 82 77, 200 81 45

E-mail: [journal@paton.kiev.ua](mailto:journal@paton.kiev.ua); [www.patonpublishinghouse.com](http://www.patonpublishinghouse.com)